ABSTRACT

Title of dissertation: DYNAMICS AND SYNCHRONIZATION OF NONLINEAR OSCILLATORS WITH TIME DELAYS: A STUDY WITH FIBER LASERS

Anthony Lawrence Franz
Doctor of Philosophy, 2007

Dissertation directed by: Professor Rajarshi Roy
Department of Physics

The effect of time delay on nonlinear oscillators is an important problem in the study of dynamical systems. Erbium-doped fiber ring lasers have an internal time scale set by the length of the laser's electromagnetic cavity. Long cavities allow thousands of modes to experience gain making it very difficult to model the lasers. We examine the effect of adding external time delays through feedback and coupling.

In the first experiment an external time delay is added to a laser by adding a feedback loop to the cavity. These delay times are varied over four orders of magnitude by changing the length of fiber in the feedback loop. The laser intensity dynamics are examined using time series, power spectra, time delay embeddings, and spatiotemporal representations. We apply Karhunen-Loève (KL) decomposition on the spatiotemporal representations and use the Shannon entropy as calculated from the KL eigenvalue spectra as a measure of the complexity of the dynamics. For long delays we find that the complexity increases as expected, but also that the fluctuation size increases.

THIS PAGE INTENTIONALLY BLANK

Report Documentation Page

Form Approved
OMB No. 0704-0188

Public reporting burden for the collection of information is estimated to average 1 hour per response, including the time for reviewing instructions, searching existing data sources, gathering and maintaining the data needed, and completing and reviewing the collection of information. Send comments regarding this burden estimate or any other aspect of this collection of information, including suggestions for reducing this burden, to Washington Headquarters Services, Directorate for Information Operations and Reports, 1215 Jefferson Davis Highway, Suite 1204, Arlington VA 22202-4302. Respondents should be aware that notwithstanding any other provision of law, no person shall be subject to a penalty for failing to comply with a collection of information if it does not display a currently valid OMB control number.

1. REPORT DATE	2. REPORT TYPE	3. DATES COVERED
19 JUL 2007		**00-00-2007 to 00-00-2007**

4. TITLE AND SUBTITLE	5a. CONTRACT NUMBER
Dynamics and Synchronization of Nonlinear Oscillators with Time Delays: A Study with Fiber Lasers	5b. GRANT NUMBER
	5c. PROGRAM ELEMENT NUMBER
6. AUTHOR(S)	5d. PROJECT NUMBER
	5e. TASK NUMBER
	5f. WORK UNIT NUMBER
7. PERFORMING ORGANIZATION NAME(S) AND ADDRESS(ES) **University of Maryland at College Park,College park,MD,20742**	8. PERFORMING ORGANIZATION REPORT NUMBER
9. SPONSORING/MONITORING AGENCY NAME(S) AND ADDRESS(ES) **The Department of the Air Force, AFIT/ENEL, Bldg 16, 2275 D Street, Wright Patterson AFB, OH, 45433**	10. SPONSOR/MONITOR'S ACRONYM(S)
	11. SPONSOR/MONITOR'S REPORT NUMBER(S)

12. DISTRIBUTION/AVAILABILITY STATEMENT
Approved for public release; distribution unlimited

13. SUPPLEMENTARY NOTES

14. ABSTRACT

The effect of time delay on nonlinear oscillators is an important problem in the study of dynamical systems. Erbium-doped fiber ring lasers have an internal time scale set by the length of the laser's electromagnetic cavity. Long cavities allow thousands of modes to experience gain making it very di?cult to model the lasers. We examine the effect of adding external time delays through feedback and coupling. In the first experiment an external time delay is added to a laser by adding a feedback loop to the cavity. These delay times are varied over four orders of magnitude by changing the length of fiber in the feedback loop. The laser intensity dynamics are examined using time series, power spectra, time delay embeddings, and spatiotemporal representations. We apply Karhunen-Lo?eve (KL) decomposition on the spatiotemporal representations and use the Shannon entropy as calculated from the KL eigenvalue spectra as a measure of the complexity of the dynamics. For long delays we find that the complexity increases as expected, but also that the fluctuation size increases. In the second experiment two lasers are mutually coupled together with a coupling time delay that is varied over four orders of magnitude. The analysis is repeated and we find the surprising result that the dynamical complexity decreases for short coupling delays as compared to the uncoupled lasers. Measurements of the optical spectra indicate a narrowing of the spectra indicating that the simplification in dynamics could be due to the reduction in the number of electromagnetic modes experiencing gain. The fluctuation size increases for all delay times and is largest when the internal and external time delays match. Lag-synchrony is also observed for the mutually coupled lasers. Recent modeling using Ikeda ring oscillators showed that stable isochronal synchrony could be achieved if a third drive laser was unidirectionally coupled with enough strength. We experimentally find that increasing the coupling strength of a third drive laser added to the mutually coupled lasers above quenches the lag-synchrony. The two response lasers become more synchronized to the drive than to each other, however the levels of isochronal synchrony are low.

15. SUBJECT TERMS

16. SECURITY CLASSIFICATION OF:			17. LIMITATION OF ABSTRACT	18. NUMBER OF PAGES	19a. NAME OF RESPONSIBLE PERSON
a. REPORT **unclassified**	b. ABSTRACT **unclassified**	c. THIS PAGE **unclassified**	**Same as Report (SAR)**	**125**	

Standard Form 298 (Rev. 8-98)
Prescribed by ANSI Std Z39-18

In the second experiment two lasers are mutually coupled together with a coupling time delay that is varied over four orders of magnitude. The analysis is repeated and we find the surprising result that the dynamical complexity decreases for short coupling delays as compared to the uncoupled lasers. Measurements of the optical spectra indicate a narrowing of the spectra indicating that the simplification in dynamics could be due to the reduction in the number of electromagnetic modes experiencing gain. The fluctuation size increases for all delay times and is largest when the internal and external time delays match.

Lag-synchrony is also observed for the mutually coupled lasers. Recent modeling using Ikeda ring oscillators showed that stable isochronal synchrony could be achieved if a third drive laser was unidirectionally coupled with enough strength. We experimentally find that increasing the coupling strength of a third drive laser added to the mutually coupled lasers above quenches the lag-synchrony. The two response lasers become more synchronized to the drive than to each other, however the levels of isochronal synchrony are low.

DYNAMICS AND SYNCHRONIZATION OF NONLINEAR OSCILLATORS WITH TIME DELAYS: A STUDY WITH FIBER LASERS

by

Anthony Lawrence Franz

Dissertation submitted to the Faculty of the Graduate School of the
University of Maryland, College Park in partial fulfillment
of the requirements for the degree of
Doctor of Philosophy
2007

Advisory Committee:
Professor Rajarshi Roy, Chair/Advisor
Professor Brian Hunt
Professor Wolfgang Losert
Professor Edward Ott
Dr. Ira B. Schwartz

The views expressed in this dissertation are those of the author and do not reflect the official policy or position of the United States Air Force, Department of Defense, or the U.S. Government.

Dedication

To my family.

Acknowledgements

I would like to thank my wife for her patience and assistance. Without her this dissertation would not have been completed. I also want to thank my children for reminding me that there is more to life than work.

I want to thank my advisor, Rajarshi Roy, for being patient, pushing, or encouraging as the situation required. He is a model of how to deal with students, both current and prospective, and colleagues as well. His insight was always inspiring.

Many other people helped in substantial ways. Ira Schwartz carefully and patiently answered any questions I had and consistently produced the perfect paper when I was stuck. Leah Shaw explained the models she used and thoroughly critiqued the work presented here.

I also want to thank former graduate students and summer students who provided assistance to me. Beth Dakin introduced fiber lasers to me and got me started on the lab's systems. Nathan Karst showed me a technique to efficiently process large collections of data files in Matlab. Min-Young Kim taught me how to splice fiber and Will Ray helped me wrap kilometers of it to make delay lines. Brian Zhou explained the Ikeda model used in his paper and helped with some delay time measurements. These simple contributions all greatly contributed to the quality of the work and the efficiency of its completion.

Table of Contents

List of Figures vi

List of Symbols ix

List of Abbreviations x

1 Introduction 1
- 1.1 Background . . . 1
- 1.2 Data visualization . . . 5
- 1.3 Measures of complexity . . . 7
- 1.4 Outline of thesis . . . 11

2 Erbium-doped fiber ring lasers 14
- 2.1 Overview . . . 14
- 2.2 Description of the laser system . . . 14
- 2.3 EDFRL dynamics . . . 19
- 2.4 EDFRL characterization . . . 19
- 2.5 EDFRL time series . . . 20
- 2.6 Spatiotemporal representation . . . 22
- 2.7 Optical spectrum . . . 25
- 2.8 Summary of Chapter 2 . . . 25

3 Fiber ring laser with a second feedback loop 28
- 3.1 Overview . . . 28
- 3.2 Experimental set-up . . . 28
- 3.3 Fluctuation size and dynamical complexity of round trip patterns . . . 29
- 3.4 Spatiotemporal representation . . . 35
- 3.5 Karhunen-Loève decomposition and spatiotemporal complexity . . . 38
- 3.6 Optical spectra . . . 52
- 3.7 Summary of Chapter 3 . . . 54

4 Two mutually coupled ring lasers 55
- 4.1 Overview . . . 55
- 4.2 Experimental set-up . . . 55
- 4.3 Fluctuation size and dynamical complexity of round trip patterns . . . 56
- 4.4 Synchronization . . . 61
- 4.5 Spatiotemporal representation . . . 64
- 4.6 Karhunen-Loève decomposition and spatiotemporal complexity . . . 67
- 4.7 Optical spectra . . . 75
- 4.8 Discussion and comparison with the single laser with feedback . . . 77
- 4.9 Summary of Chapter 4 . . . 82

5 Driven mutually coupled lasers 83
5.1 Overview 83
5.2 Experimental set-up 84
5.3 Driven uncoupled lasers 87
5.4 Driven mutually coupled lasers 94
5.5 Discussion and summary of Chapter 5 95

6 Conclusions and future work 102
6.1 Conclusions 102
6.2 Future work 104

Bibliography 107

List of Figures

2.1 Erbium ion energy levels used by the laser. 15

2.2 Configuration of the fiber amplifier. 16

2.3 Erbium-doped fiber ring laser setup. 17

2.4 Laser power as a function of pump strength. 21

2.5 Erbium-doped fiber ring laser intensity time series. 22

2.6 Spatiotemporal representation of Erbium-doped fiber ring laser intensity. 26

2.7 Optical spectrum of the Erbium-doped fiber ring laser. 27

3.1 Experimental setup for the laser with a second feedback loop added. . 30

3.2 Time series for the laser with different feedback delay times. 32

3.3 Ratio of the standard deviation to the mean for different feedback delays. 33

3.4 Time delay embeddings for different feedback delays. 36

3.5 Spatiotemporal representations for different feedback delays. 39

3.6 Envelope of the full 1 ms time series for select feedback delays. 40

3.7 KL decomposition for the laser without feedback. 43

3.8 KL decomposition for the laser with a 0.068 μs feedback delay. 45

3.9 KL decomposition for the laser with a 10.3 μs feedback delay. 46

3.10 KL decomposition for the laser with a 120 μs feedback delay. 47

3.11 KL decomposition for uniformly distributed random data. 48

3.12 Complexity measures for the laser with a second feedback loop added. 51

3.13 Optical spectra for the laser with a second feedback loop added. . . . 53

4.1 Experimental setup for two mutually coupled fiber ring lasers. 57

4.2 Time series for the mutually coupled lasers with different coupling delay times. 59

4.3 Ratio of the standard deviation to the mean for different coupling delays. 60

4.4 Time delay embeddings for different coupling delays. 62

4.5 Cross correlations between two mutually coupled lasers' time series. . 65

4.6 Spatiotemporal representations for different coupling delays. 66

4.7 Full 1 ms time series for select mutual coupling delays. 68

4.8 KL decomposition for laser 1 uncoupled. 70

4.9 KL decomposition for laser 1 with a 0.050 μs coupling delay. 71

4.10 KL decomposition for laser 1 with a 0.218 μs coupling delay. 72

4.11 KL decomposition for laser 1 with a 120 μs coupling delay. 73

4.12 Complexity measures for the mutually coupled lasers. 74

4.13 Normalized eigenvalue spectra for laser 1 and laser 2 when uncoupled. 76

4.14 Optical spectra for the mutually coupled lasers. 78

5.1 Experimental setup for two mutually coupled fiber ring lasers driven by a third laser. 85

5.2 Cross correlations for unidirectional driving of uncoupled response lasers pumped at $1.4I_{th}$. 88

5.3 Cross correlations at specific shifts for unidirectional driving of uncoupled response lasers pumped at $4I_{th}$. 90

5.4 Cross correlations at specific shifts for unidirectional driving of uncoupled response lasers pumped at $2I_{th}$. 91

5.5 Cross correlations at specific shifts for unidirectional driving of uncoupled response lasers pumped at $1.4I_{th}$. 92

5.6 Cross correlations at specific shifts for unidirectional driving of uncoupled response lasers pumped at $1.2I_{th}$. 93

5.7 Cross correlations for unidirectional driving of mutually coupled response lasers pumped at $1.4I_{th}$. 96

5.8 Cross correlations at specific shifts for unidirectional driving of mutually coupled response lasers pumped at $2I_{th}$. 97

5.9 Cross correlations at specific shifts for unidirectional driving of mutually coupled response lasers pumped at $1.4I_{th}$. 98

5.10 Cross correlations at specific shifts for unidirectional driving of mutually coupled response lasers pumped at $1.2I_{th}$. 99

List of Symbols

$C_{n-1,n}$	Cross correlation between round trips n and n-1
$CC_{x,y}$	Cross correlation between time series x and y
D_{KL}	Number of KL modes needed for S to exceed an arbitrary cut-off
H	Shannon entropy
$I(t)$	Intensity time series
$I_n(t)$	Intensity of round trip n at time t
I_p	Pump current
I_{th}	Threshold pump current
J	Number of data points overlapping in $CC_{x,y}$ with shift s
$\mathbf{K}$	Covariance matrix
$M(Y;X)$	Mutual information between time series X and Y
N	Number of KL eigenvalues in the cumulative sum S
n_t	Round trip number
$p(x)$	Probability of x occurring
$p(x,y)$	Joint probability of x and y occurring
$S(N)$	Cumulative sum of the N largest eigenvalues
s	Cross correlation time shift
T_1	First embedding delay
T_2	Second embedding delay
t	Time
$u(x_j, n_t)$	Spatiotemporal data at position x_j and round trip number n_t
x_j	Position around ring cavity
α_i	Expansion coefficient for KL mode i
Δ_f	Bandwidth
δ_{ik}	Kronecker delta function
κ	Coupling strength of feedback or mutual coupling
κ_D	Coupling strength of drive to response transmission
κ_{MC}	Coupling strength of mutual coupling
λ	Wavelength
$\tilde{\lambda}_i$	Eigenvalue for KL mode i
λ_i	Normalized eigenvalue for KL mode i
ψ_i	KL mode i
σ_x	Standard deviation of x
τ	Feedback or mutual coupling time delay
τ_c	Coherence time
τ_r	Laser cavity round trip time

List of Abbreviations

DC	Direct current
DL	Delay Line
EDFA	Erbium-Doped Fiber Amplifier
EDFRL	Erbium-Doped Fiber Ring Laser
FA	Fiber Amplifier
FWHM	Full Width at Half Maximum
IR	Infrared
KL	Karhunen-Loève
OSA	Optical Spectrum Analyzer
OSC A	Oscilloscope used to measure laser dynamics
OSC B	Oscilloscope used to monitor feedback or coupling lines
PC	Polarization Controller
PD	Photodetector
VA	Variable Attenuator
WDM	Wavelength Division Multiplexer

Chapter 1

Introduction

1.1 Background

The dynamics of delay-coupled systems are rich and varied, and very important for the consideration of biological, chemical, and physical systems, including blood production [1], chemical reactions involving transport processes [2, 3], laser systems [4, 5], and electronic circuits [6]. Delays are often neglected for simplicity, and this may be a good approximation when they are very short compared to other system time scales. On the other hand, studies of time-delayed systems show that increasing delays lead to more complex, high dimensional dynamics [7]. Time-delays can play a very important role in the dynamics and function of networks of coupled elements, and often influence their collective dynamics. The adaptive nature of systems with delays, such as the variability of the number of degrees of freedom involved at a given point in their time evolution, is of interest and significance for specific applications [8].

As an illustration of these general ideas we will examine the dynamics of fiber lasers with either time-delayed feedback or time-delayed coupling with time-delays, τ, that extend over four orders of magnitude. Lasers have an important internal time scale, the round trip time, τ_r, needed for light to traverse the laser cavity. Thus, we consider a system with an internal, fixed time delay (τ_r) and apply time-delayed

feedback or time-delayed mutual coupling with a second time delay (τ) that varies from less than to well above the internal delay. The lasers each have thousands of lasing modes that are nonlinear oscillators globally coupled through sharing population inversion. It is a daunting task to model the laser systems with hundreds or thousands of coupled-mode equations, since many unknown parameters relating to the mode-coupling would be involved [9]. A time domain model that involves delay-differential equations has sometimes been employed as an alternative [5, 10] but even this approach presents serious difficulties when long lengths of fiber with random birefringence fluctuations are involved. Because of these difficulties typical of time delay systems we chose to employ the KL decomposition of spatiotemporal representations.

A very important application for fiber lasers is optical communication. Erbium-doped fiber lasers emit light with a wavelength of around 1.55 μm which matches an absorption minimum in silica fibers commonly used to transmit optical signals [11]. Optical communication using chaotic waveforms offers potential advantages in terms of privacy [12] and robustness due to broadband transmission [13]. Recently, chaos based communication was demonstrated over 120 km of commercial fiber optic line in Athens, Greece [13]. As chaotic communication systems and ideas are developed it will be important to understand how the components of the system interact over transmission lines that are kilometers long. More importantly, the dynamics of the coupled components in the presence of long delays needs to be understood. Previously optical communication using chaotic waveforms has been demonstrated in the laboratory with erbium-doped fiber ring lasers (EDFRL) [14, 15]. Fiber lasers

are attractive because of their high dimensional dynamics, which adds to privacy and large bandwidth [12], as well as the potential of an all optical communication system [16].

In communication systems, a single laser becomes useful when it interacts with other lasers and detectors. Injection locking of lasers is a common practice that can be used to lock the frequency and phase of a laser to an injected signal if the injected signal is strong enough [17, 18]. Previous modelling indicated that this can affect the intracavity dynamics of the laser [19, 20]. Researchers have experimentally studied the synchronization of chaotic EDFRLs with unidirectional coupling where light is injected from one laser into a second laser [3, 21, 22]. These papers presented time series 1 ms long or greater and did not examine the intracavity dynamics. They also did not examine variations due to multiple coupling line lengths, and the coupling line lengths were short, except for the work of Kim, et. al., [3] which used a 1.5 km length coupling line.

Mutual coupling of two EDFRLs can be achieved by injecting light from laser 1 into laser 2 and simultaneously injecting light from laser 2 into laser 1. Synchronization of coupled oscillators is a common occurrence [23]. Even nonlinear chaotic oscillators will synchronize [24, 25]. These lasers are no exception and the synchronization of mutually coupled chaotic lasers was recently studied experimentally and theoretically [26, 27]. These papers examined the intracavity dynamics of the matched lasers with 46 m cavity lengths and used matched coupling lines 9 m long. The effect of coupling strength was analyzed in detail. When coupled with strong enough coupling, the two lasers became chaotic and delay synchronized with a de-

lay equal to the length of the coupling lines. The intracavity intensity patterns repeated over several round trips. Another paper specifically analyzed the effect of the transmission line on the ability of a system to communicate using chaotic lasers [28]. This numerical work considered transmission lines hundreds of kilometers long, but only evaluated the quality of data transmission, not the effect of varying the transmission, or coupling, delay on the lasers' dynamics. There have also been many studies on leader/follower dynamics and switching in coupled semiconductor lasers [29, 30, 31, 32, 33].

Recently, theoretical work was done that developed a method for setting up stable isochronal synchrony between two coupled nonlinear oscillators [34]. A third oscillator is used to drive the two mutually coupled oscillators. The oscillators considered were Ikeda ring oscillators [5, 35] and the technique is based on generalized synchronization. Generalized synchronization occurs when the state of a response system is determined by the state of the driving system [23, 25, 36]. In this case the drive forces a spatially extended system (the two mutually coupled lasers) into generalized synchronization and the two separated (but mutually coupled) lasers synchronize to each other isochronally. The isochronal synchrony developed as the drive oscillator's coupling strength was increased, replacing the initially observed lag-synchrony.

1.2 Data visualization

We display the dynamics of the laser intensity using time series plots, power spectra, time delay embeddings, and a spatiotemporal representation of the time series. We use several methods to visualize different aspects of the dynamics. The time series plots of the laser intensity show patterns in the dynamics such as regular oscillations and round trip repetition, or the apparent lack of regular structure. We will look at time series on the scale of both the round trip time, τ_r, and the feedback or coupling delay time, τ. Power spectra show which frequencies dominate the dynamics. Time delay embeddings are used to reconstruct the phase space of a dynamical system from a time series of experimental data [37, 38]. Plots of the time series in these embeddings are a way to view the complexity of the time series and can illustrate the nature of the dynamical behavior. Finally, spatiotemporal representations are a way to visualize a time series that has dynamics with two very different time scales [39]. The one-dimensional time series is recast into a two-dimensional representation by breaking the time series up into sections with a size determined by an important time scale. In previous work both the ring laser round trip time [26, 27] and the feedback delay time [39] have both been used. To build the spatiotemporal representation the time series is broken up into strips of data that are one time scale in length. These strips are then stacked on top of each other. The resulting data set is plotted with different colors representing different values of intensity, where each point is indexed by time within the time scale and the number of time scales. We used the round trip time as our basis in

order to compare the results for different delay times. The "spatial" part of the representation comes from mapping the times within a round trip to positions along the ring cavity [40]. This idea uses Taylor's hypothesis from fluid mechanics [41], which states that if a fluid flow is fast enough a spatial pattern of turbulence can be measured by a single detector at a fixed location as the fluid moves past it. In our case the light propagating around the ring is the flow and the relatively stable round trip patterns are measured at a single point at the output of the ring cavity. These plots can display large amounts of data compactly and show features with different time scales so the round trip pattern stability can be observed and comparisons made between data sets. These four methods provide different ways of visualizing data that give us a qualitative understanding of the dynamics. We use them as a starting point to derive quantitative measures of the dynamical characteristics.

One of our results is that the fluctuation size of the laser intensity varies with delay and configuration. The size of the fluctuations in a time series is quantified by the ratio of the standard deviation of the time series to its mean. We also find that the mean of the laser intensity is not affected by varying the delay. Thus, normalizing each time series by its mean allows us to compare the relative fluctuation size between time series easily.

Another important set of data are the optical spectra of the lasers. The variation of the widths and heights of peaks in the optical spectra are considered to determine if the lasing wavelength is affected by the second feedback loop or coupling to a second laser. Spectral measurements provide us with a means to assess the influence of the feedback or coupling on the coherence properties of the lasers.

1.3 Measures of complexity

One of our results is that the feedback or coupling time-delay changes the complexity of the dynamics, and we want to describe this effect with a quantitative measure. There are many measures of complexity [42] and we examine two that use the eigenvalue spectrum calculated from the Karhunen-Loève (KL) decomposition technique [43]. Defining the complexity of data is a tricky business because different measures of complexity have been used by different people to answer different questions. Also, people tend to consider something to be simple when they understand it and complex when they do not, giving "complexity" a subjective character that must be removed for careful scientific investigation [42]. One approach is to consider the level of chaos in the dynamics. Chaotic dynamics are regarded as complex compared to steady state or periodic dynamics. Systems with complicated attractors produce more complex dynamics. Given the attractor of a dynamical system in an appropriate phase space, generalized dimensions, D_q, of the attractor can be calculated. These consider the number of boxes needed to cover the attractor and weight each box by a probability measure of how often a typical trajectory visits the box [36]. Another method, used by Farmer [7] with the Mackey-Glass equation [1], is to calculate the Lyapunov exponents and get the information dimension, D_1, using the Kaplan-Yorke conjecture [44]. The Kolmogorov-Sinai entropy, or metric entropy, is a third measure of the level of chaos in a system. It measures the rate of creation of information as the trajectory evolves. It is calculated from an entropy function of partitions of phase space. The entropy function uses the probability

measure defined over the partitions [36].

To calculate these quantities from our data we must first embed the data in a proper phase space [37]. This is difficult for our measurements. First, we have noise in our data and dealing with it complicates the phase space reconstruction process [45]. Second, our data is taken with an 8-bit oscilloscope which provides limited voltage resolution and temporal sampling.

Another approach used in algorithmic information theory neglects the idea of probabilities and considers a computer processing data. The Kolmogorov complexity of an object is defined as the length of the shortest computer program that can describe the object [42, 46, 47, 48, 49, 50]. A string of periodic data could be represented by a program that says "print the data making up a period and repeat n times." A random set of data of the same length could only be described by repeating the data. For a random sequence the expectation value of the Kolmogorov complexity is close to the Shannon entropy of the process [46]. The difficulty here is coming up with the smallest algorithm to describe the data. A related idea is how compressible a set of data is. A complexity measure from coding theory by Lempel and Ziv [42, 46, 51, 52] looks at patterns in a string of binary data. The algorithm goes through the data and adds one to the complexity measure each time it finds a pattern in the data that it hasn't seen before. This method has the drawback that almost all sequences that are sufficiently large have a high complexity, regardless of the data in the sequence [51]. This method, like all algorithmic methods, rates randomness with the most complexity. For some applications the linking of high levels of complexity with randomness is not of interest. Random

is just seen as disordered, while complex structures such as a chaotic attractor are more interesting [53, 54].

The number of elements that make up a system contribute to the complexity. The number of elements in the system also depends on the scale we chose to consider. For example we can consider properties of a gas by thinking of macroscopic quantities such as pressure or by thinking of microscopic quantities of the molecules that compose the gas [8]. Structural complexity can form in a system of elements that cannot be explained by the simple application of elementary laws applied to the elements and the interconnection of elements [42, 54]. In the lasers studied in this dissertation, there are thousands of longitudinal electromagnetic modes that are oscillating and interacting. Describing these modes and their interactions individually is very difficult, particularly since we cannot measure the intensities of the individual modes. We need to remember that the electromagnetic modes are present because thinking about their behavior can help explain the dynamics of the total intensity that we measure. The round trip time is a time scale of fundamental importance to the dynamics. We can use this to set up the spatiotemporal representations described above. These representations show structures that result from the interaction of thousands of modes in the active gain medium. To analyze the structures we chose to use the KL decomposition technique.

KL decomposition has many broad applications including analyzing turbulence [55, 56, 57], performing face recognition [58], and examining transverse profiles of laser beams [59, 60, 61]. Different fields have come up with different names for the technique, including principal component analysis, principal value decomposition,

singular value decomposition, singular system analysis, singular spectrum analysis, bi-orthogonal decomposition, proper orthogonal decomposition, and empirical orthogonal functions [62]. KL decomposition expands the data in an optimal orthogonal basis. The basis is optimal in that it minimizes the mean squared truncation error of the expansion. This is achieved by finding a basis vector that maximizes the mean squared projection of the data. Succeeding basis vectors are found that maximize the projection with the additional constraint that they be orthogonal to the preceding basis vectors [43]. The expansion can be truncated at a certain number of terms depending on the accuracy requirements of the application.

Here we apply the technique to the data in our spatiotemporal representation. The spatial dimension is formed from our map of temporal measurements of intensity for one round trip of the laser cavity to ring position in the spatiotemporal representation. We consider two methods to quantify the complexity using the results of the KL decomposition. First, we note that the number of KL modes needed to reconstruct the system dynamics to a given accuracy will be small for round trip patterns that are consistently present in the dynamics and larger when the dynamics are composed of many different patterns over the time scale considered. The magnitude of the eigenvalue corresponding to a KL mode gives a measure of the mode's importance in reconstructing the dynamics. The number of eigenvalues that need to be added to reach some selected cut-off gives us a measure of the overall complexity of the time series [43, 55, 63, 64]. Second, we interpret the eigenvalues of the KL modes to be the probabilities that the mode will contribute to the dynamics [43, 65] and calculate the Shannon entropy, or information, of the modes [46, 66, 67]. The

Shannon entropy plays a role in many of the complexity measures described above. In this case it quantifies how many KL modes will be important to the dynamics of the data. These two measures of complexity were chosen for our data because they are easy to calculate from the KL decomposition which isolates coherent structures in the data in an optimal way.

1.4 Outline of thesis

In the following chapter the reader is introduced to the EDFRL and the dynamics typically seen in these systems. Following chapters describe more complex configurations of EDFRLs and present the results from each configuration.

Chapter 2 describes the components of the EDFRLs used in these experiments. The measurement of important characteristics of the lasers are discussed. Time series are presented and a spatiotemporal representation is used to display the dynamics of the EDFRL. The process used to construct the spatiotemporal representation described. This chapter provides a baseline for comparison with results from succeeding chapters with more complex configurations.

Chapter 3 describes the next experiment where a second time-delayed feedback loop is added to the laser. This case is important to analyze for two reasons. First, EDFRL experiments use extra loops in the cavity to achieve an effect, such as to make communication more secure [3, 14] or to generate multiple wavelengths [68]. Second, we want to have results from the simpler case of a single laser with feedback to compare to the results from a mutually coupled laser experiment. The feedback

delay time, τ, is varied over four orders of magnitude from less than to much greater than the internal round trip time of the laser. The coupling strength is monitored to make sure it is constant for all delays. The data are presented in several ways, including time series plots, power spectra, time delay embeddings, and spatiotemporal representations. These different visualizations help us gain an understanding of how the dynamics change with changing feedback delay times. The process used to create the time delay embeddings is described. We see an increase in fluctuation size for long feedback delays and a variety of dynamics ranging from simple oscillations to complex patterns. Finally, the calculation of the KL decomposition and the complexity are presented in detail.

In Chapter 4 two mutually coupled EDFRLs are considered. The coupling delay, also referred to as τ, is varied over four orders of magnitude again. The same visualization techniques are used and show a variety of dynamics. The KL decomposition is performed on the spatiotemporal representations to calculate the complexity of the dynamics. A surprising result is that mutually coupling the lasers with a short delay simplifies their dynamics compared to the lasers without coupling. We also see lag-synchronization of the lasers and examine the lag time using cross correlations.

In Chapter 5 we experimentally investigate the isochronal synchrony scheme described in Section 1.1 by adding a third drive laser to the two mutually coupled lasers described in Chapter 4. We quantify the level of synchrony with a cross correlation that uses an appropriate time shift between the two time series. With no mutual coupling between the two response lasers we find an increase in the

isochronal synchrony as the drive coupling increases, but the level of synchrony remains low. When mutual coupling between the response lasers is added we find that increasing the drive coupling strength will quench the lag synchrony of the mutually coupled lasers. The isochronal cross correlation becomes larger than the lag cross correlation, but the level of synchrony remains low. More work can be done to match parameters more closely to try to increase the level of isochronal synchrony.

Chapter 6 will summarize the important results and suggest future work to explore these systems.

Chapter 2

Erbium-doped fiber ring lasers

2.1 Overview

This chapter will introduce the erbium-doped fiber ring laser (EDFRL) we are using as our nonlinear oscillator. It will describe the laser system and discuss the dynamics produced by a solitary laser without feedback or coupling. This will establish a baseline to which we will compare the dynamics observed in other configurations of the laser.

2.2 Description of the laser system

The laser system used in these experiments is an EDFRL. The Er $^{3+}$ ion is the active atom that is excited to produce the laser light. An energy level diagram with the transitions used is shown in Fig. 2.1. The atoms act like a three level laser system and are optically pumped from the $^4I_{15/2}$ ground state to the $^4I_{11/2}$ state. The atoms quickly relax to the metastable $^4I_{13/2}$ state which has a 10 ms spontaneous emission decay time. Laser light at 1550 nm is produced when stimulated emission causes the atoms to relax back to the ground state. The energy levels are broadened and split due to transition lifetime broadening, inhomogeneities in the glass host, and the Stark effect [69]. The energy levels are thus represented by manifolds of

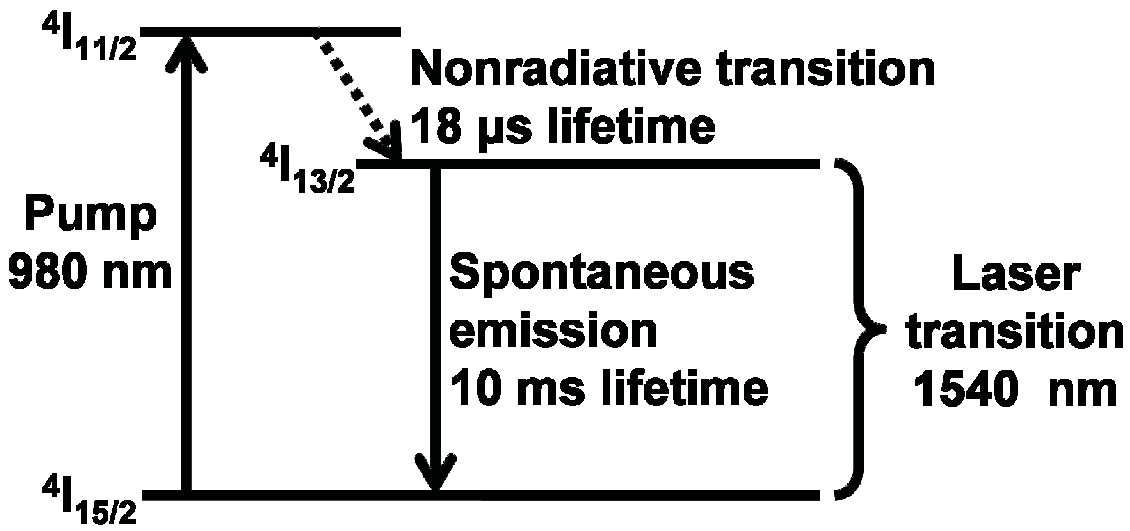

Figure 2.1: Erbium ion energy levels used by the laser. Erbium ions are pumped to the $^4I_{11/2}$ level where they quickly decay nonradiatively to the metastable $^4I_{13/2}$ level. Laser light comes from stimulated emission from the metastable level to the ground level transition. Data in the figure is from [69].

several broadened, split levels and the bandwidth of the gain of the amplifier can range from 25 nm to 60 nm depending on the glass host [70].

Silica glass fiber is doped with the Er $^{3+}$ ions to make an erbium-doped fiber amplifier (EDFA). We used an Oprel OFA-1203-17 EDFA that is configured as shown in Fig. 2.2. The amplifier is optically pumped with a laser diode operating at a wavelength of 980 nm. The pump light is injected into the erbium-doped fiber with a wavelength division multiplexer (WDM). The optical isolators force the light to propagate in one direction through the amplifier [71].

To make a laser out of the EDFA connect the input and output ports to each other with a loop of optical fiber. This completes a ring cavity that allows for light generated by stimulated emission to be fed back through the active fiber containing

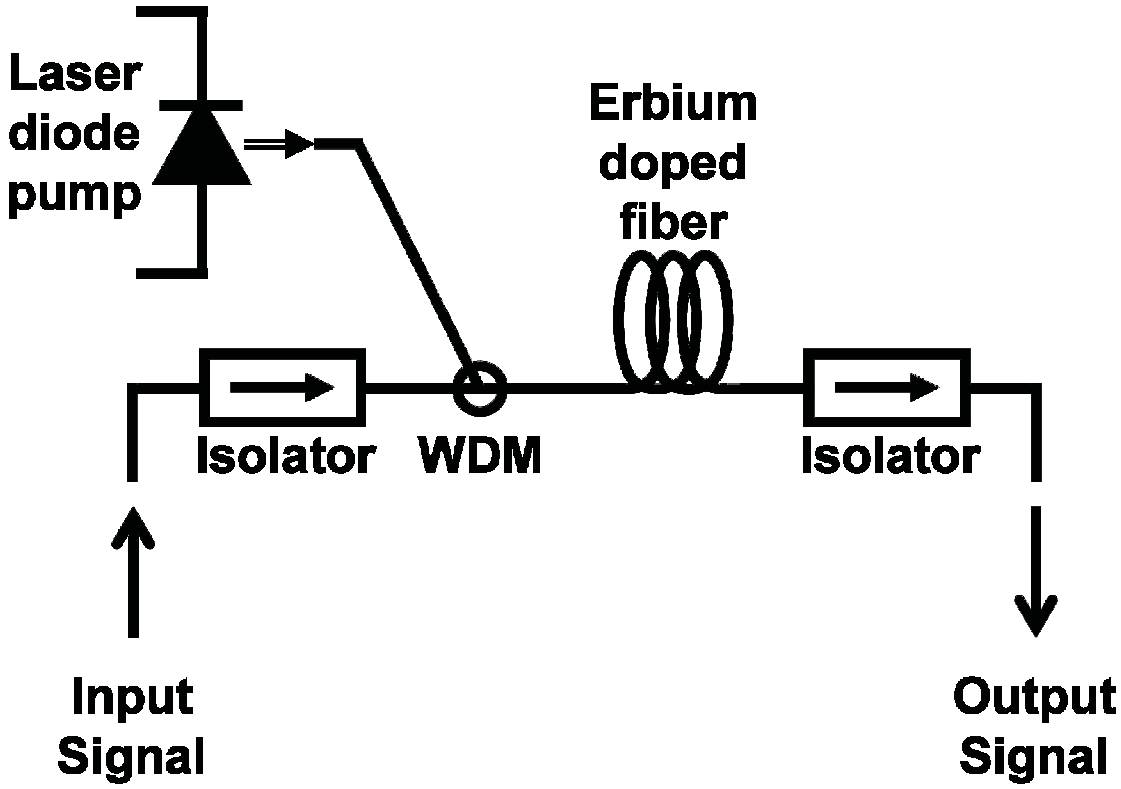

Figure 2.2: Configuration of the EDFA. Pump light from the laser diode is coupled into the fiber with a wavelength-division multiplexer (WDM). The pump light enters the Erbium-doped fiber and excites the Erbium ions. The input signal causes stimulated emission which amplifies the signal. Faraday isolators are used to maintain the direction of light flow in the amplifier. Based on Fig. 5.1 in [71].

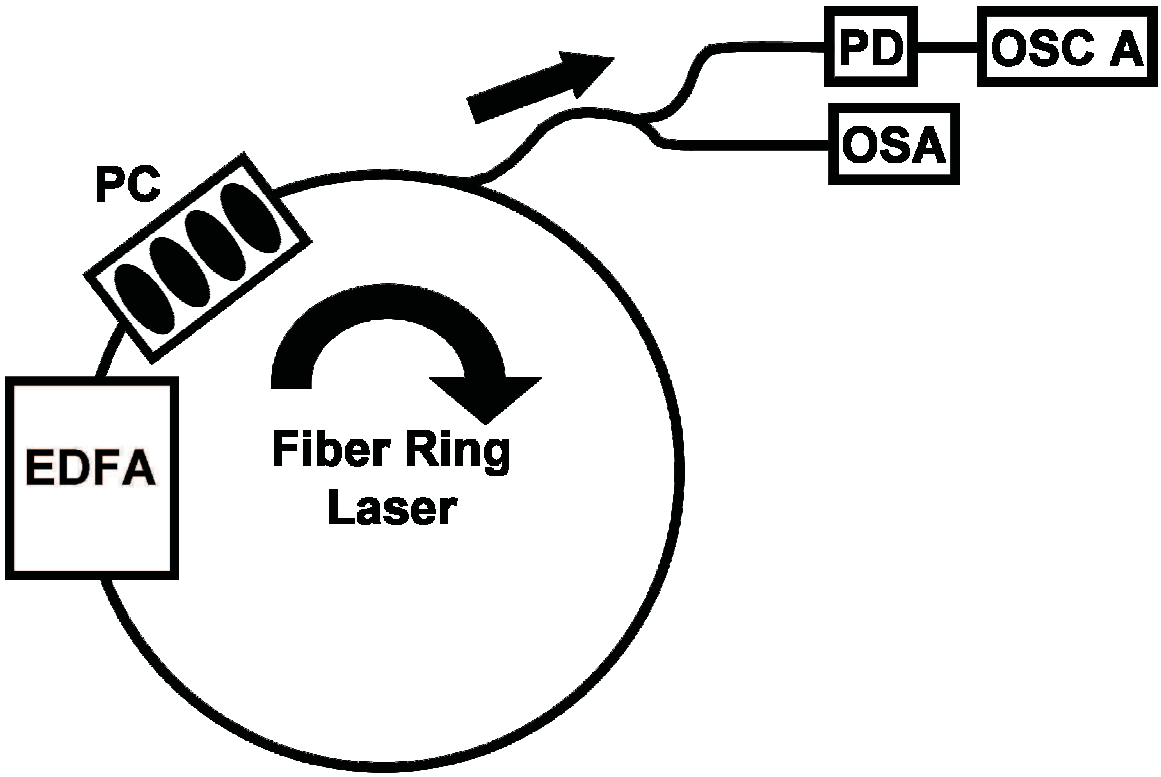

Figure 2.3: Experimental setup for the EDFRL. The arrows show the direction of light propagation through the ring. EDFA, erbium-doped fiber amplifier; PC, polarization controller consisting of a sequence of linear polarizer, quarter wave plate, half wave plate, and quarter wave plate; PD, photodetector; OSC A, oscilloscope used to measure the laser intensity dynamics; OSA, optical spectrum analyzer.

the Er^{3+} ions and generate still more light. This feedback allows the intensity of the light to grow until the amplifier saturates. Figure 2.3 shows an EDFRL with typical components.

The EDFA was discussed above. The optical fiber used in the cavity is single mode silica glass fiber. The fiber has a minimum in its absorption profile around 1550 nm, making erbium ions an attractive source of laser light for transmission in optical fibers [11]. The fiber has a 9 μm diameter core and supports only one

transverse electromagnetic mode. The wavelength of the laser light is set with the polarization controller (PC). The PC contains a linear polarizer, a quarter wave plate, a half wave plate, and another quarter wave plate. These are used to adjust the polarization of the light in the cavity. The fiber is birefringent [11] so different polarization states will experience a different index of refraction and hence a different optical path length through the cavity. Thus, the PC selects different wavelengths from within the gain bandwidth and allows us to tune the laser's wavelength. Finally, the laser is much more useful if we can get some of the light out of the cavity. We use evanescent couplers from Gould Fiber Optics to couple light into or out of the cavity. These are rated by the fraction of the input light passed to each of the output paths. For example, a 95/5 coupler was used pull some light out of the laser cavity and send it to the oscilloscope (OSC A) and optical spectrum analyzer (OSA). This coupler will keep 95% of the light in the ring and divert 5% to the measuring instruments.

The laser light intensity is measured by a New Focus model 1811 IR DC photodetector (PD) with a 125 MHz bandwidth. The photodetector's signal is passed to a LeCroy LC534AM digital oscilloscope (OSC A) with 8-bit resolution. The sampling rate is 1 GHz with 10^6 points saved per channel for two channels or less. If three or four channels are used the sampling rate drops to 500 MHz and only 5×10^5 points per channel are saved. Optical spectra are measured with an Agilent 86141B optical spectrum analyzer (OSA).

2.3 EDFRL dynamics

An advantage of fiber lasers is that the optical cavity can be long enough that the round trip time, τ_r, is hundreds of nanoseconds long and easily resolvable with modern detectors and oscilloscopes. This allows us to investigate the dynamics on time scales smaller than a round trip. Previous work [72] has taken advantage of the measurable resolution time and found that the light output has a steady state intensity with small fluctuations about the mean. These fluctuations produce a pattern over one round trip that changes slowly over many subsequent round trips as noise modifies it [10]. The evolution of the patterns is very slow compared to τ_r. The patterns are not regular or periodic within the round trip, but are stable for hundreds of round trips.

These long cavity lasers are high dimensional systems. Long cavity length and broad gain profile allow thousands of longitudinal modes to exist simultaneously in the cavity [10]. Additionally, the modes are coupled to each other through the gain medium. This prevents a reduction to a simple low dimensional system, such as those in models used for semiconductor lasers [73].

2.4 EDFRL characterization

A laser was setup as shown in Fig. 2.3 and designated "laser 1." An important parameter of the laser is the pump threshold at which the Er^3+ ions are driven into the upper laser level fast enough to allow stimulated emission to occur. The pump rate is related to the pump current, I_p, of the laser diode in Fig. 2.2. The pump

current threshold, I_{th}, is found by measuring the power out of the laser for increasing values of I_p. For $I_p < I_{th}$ the light comes from spontaneous emission and the power level is small. For $I_p > I_{th}$ stimulated emission begins to dominate and the laser power increases linearly with increasing I_p. A linear fit of the steep part of the data gives an estimate of I_{th}. Power measurements were made using the photodetector and oscilloscope. One hundred sweeps were averaged and the mean of the average was recorded. The data and a linear fit are shown in Fig. 2.4. Extrapolating the fit to a power of zero gives $I_{th} = 15.7$ mA.

The round trip time of the ring cavity was measured by making use of the repetition of the round trip patterns. This repetition occurs because the upper laser level lifetime is very long ($\approx$ 10 ms [9]) so the population inversion responds very slowly compared to the laser field. We calculate the power spectra of five 1 ms time series of intensity data. Because of the round trip repetition there is a spectral peak at the round trip time along with higher harmonics. We average the frequency of the first peak for all five spectra and invert it to find $\tau_r = 213.89 \pm 0.03$ ns, which corresponds to a cavity length of about 44.4 m.

2.5 EDFRL time series

Figure 2.5 shows a time series of intensity data taken from the laser. The intensity is normalized by the mean intensity. Figure 2.5(a) shows the entire 1 ms time series. The variation is typically less than 6% showing that the laser is stable. Figure 2.5(b) is a 10 μs section from the middle of plot(a) and shows some repetition.

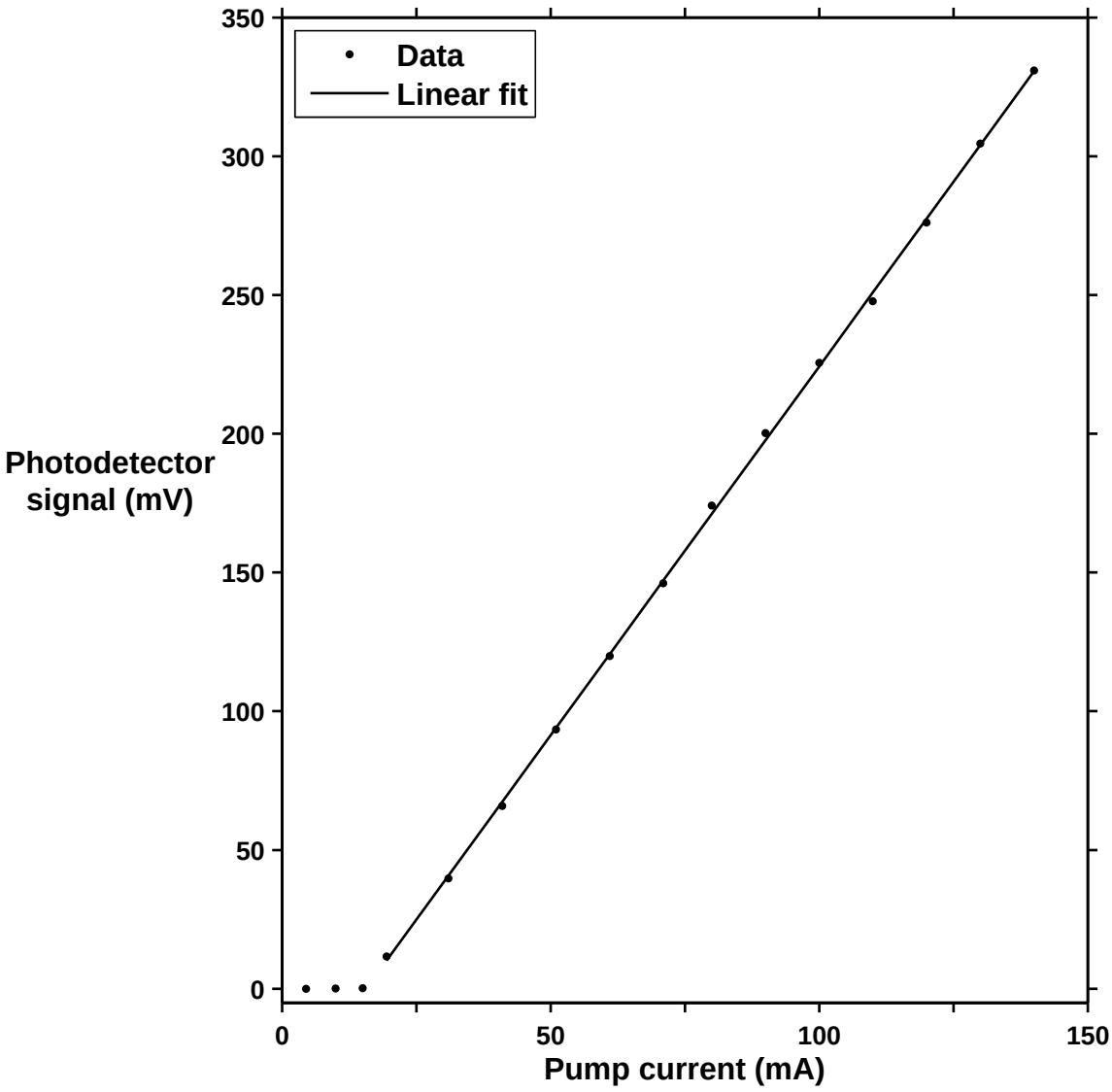

Figure 2.4: Laser power as a function of pump strength for the EDFRL. The power out is represented by the average photodetector signal as described in the text. The pump strength is represented by the pump current through the semiconductor laser used to pump the erbium ions.

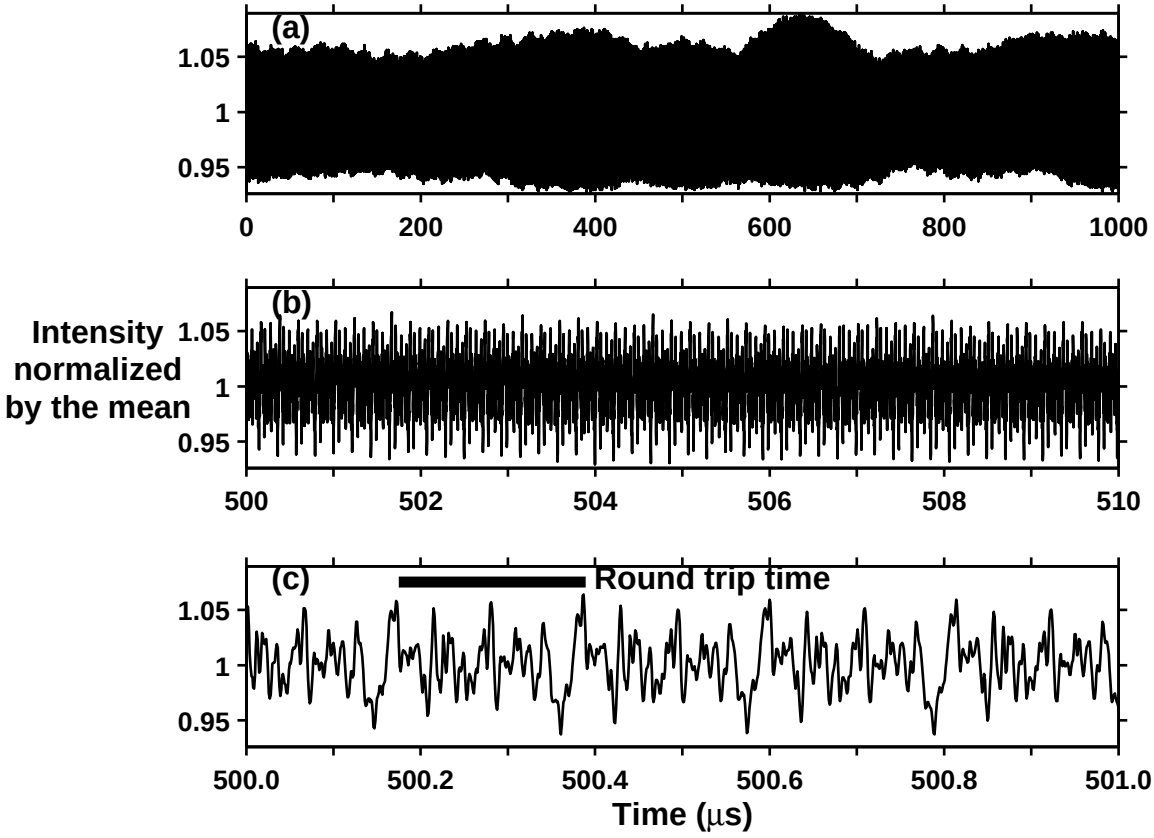

Figure 2.5: Intensity time series for the EDFRL. (a) Entire 1 ms time series normalized by the mean. (b) Ten μs portion of the time series in (a). (c) One μs portion of the time series in (b). The round trip pattern repetition is visible in this plot.

Figure 2.5(c) expands the first μs of plot (b) and shows the round trip repetition every 214 ns as expected.

2.6 Spatiotemporal representation

Because of the visibility into the intracavity dynamics and the ability of the oscilloscope to save long data sets we have a dilemma about how to look at the time series. We can examine the overall data set as in Fig. 2.5(a), but then we cannot

see the details of the round trip behavior as shown in Fig. 2.5(c). If we want to examine the round trip pattern variability we must tediously work our way through the thousands of round trips we collected in the 1 ms time series. To examine the complexity and variability of the round trip patterns, the time series need to be represented in a new way that shows us information on the time scales of both τ_r and τ. A spatiotemporal representation of the data is used to examine the dynamics of a system over many intervals of τ_r. We use τ_r as the baseline time scale since we will vary τ from run to run later and τ_r is consistent for all of the time series. It also is meaningful to the dynamics as the round trip repetition shows. This repetition is what allows the spatiotemporal representation to be meaningful visually.

To reduce the amount of data to more manageable sizes, we plot only every tenth round trip of 4500 total round trips. Since the round trip patterns do not change over the scale of ten round trips, we still obtain an accurate representation of the dynamics (Fig. 2.5 shows this stability over four round trips). Each time series is re-scaled from 0 to 1 to better see the features in the fluctuations. Now two problems must be addressed to create the spatiotemporal representations. First, the time series is composed of discrete data, and the end of the round trip will most likely lie in the gap between measurements. We improve our precision in this respect by linearly interpolating nine data points between our existing data to give a resolution of 0.1 ns. The second issue is that there is uncertainty in the round trip time measurement, so we do not know exactly which data point to use to start the next round trip. This error grows as we skip round trips. We can sidestep this problem by using the fact that the intensity pattern repeats every round trip. To

determine the starting element of the next round trip to stack on our plot, we use a correlation measure

$$C_{n-1,n}(s) = \sum_t (I_{n-1}(t) - \langle I_{n-1} \rangle)(I_n(t+s) - \langle I_{n,s} \rangle), \tag{2.1}$$

where $I_{n-1}(t)$ is the intensity of the previous round trip where t indexes the position in the ring, $I_n(t)$ is the intensity of the current round trip at position t, $\langle I_{n-1} \rangle$ is the time average over the previous round trip, and $\langle I_{n,s} \rangle$ is the time average of the current round trip shifted by s [74]. A range of ± 5 ns centered on the estimate of the starting point was used for s. The correlation usually selected elements within a range of ± 1 ns or less of the estimate. The correlation will favor lining up high frequency structures more than low frequency structures because the high frequency structures vary more over the correlation range. Low frequency components do not vary much over a small range, and so the correlation from a low frequency signal is more uniform, allowing noise or other features more influence on $C_{n-1,n}(s)$. In some cases a tighter range on s of ± 1 ns was needed because some time series had a significant low frequency component with either a small amplitude high frequency component overlaid on it or no high frequency component at all. The larger range of s allowed the correlation to select starting points that were far apart from each other, resulting in artificial discontinuities.

Figure 2.6 shows the spatiotemporal representation for the intensity of the EDFRL. More information can be presented in this type of plot than in a time series plot. Structures in the round trip pattern can be stable for hundreds or even a thousand round trips or may slowly vary on these time scales. There is little

periodic structure within the round trip patterns of the solitary laser, except for specific settings of the polarization controller [72].

2.7 Optical spectrum

The optical spectrum of the laser is shown in Fig. 2.7. The full width at half maximum (FWHM) is about 0.2 nm and the peak is centered at about 1550.5 nm. This gives a bandwidth of about 17 GHz which is sufficient to accommodate approximately 4000 longitudinal modes of the laser which have a spacing of 4.45 MHz (51.5 fm) [75]. The small spacing between modes is due to the 44 m cavity of the fiber laser (compare this length to the millimeter size cavity of a semiconductor laser). Many modes experience gain which makes long cavity lasers more complex.

2.8 Summary of Chapter 2

Now we have a baseline for how our EDFRL behaves. The average laser intensity is stable and the fluctuations follow patterns that repeat every round trip. These patterns slowly evolve as spontaneous emission noise modifies them. This behavior is expected and illustrated with the spatiotemporal representation. The optical spectra is a single narrow peak, but due to the small spacing between longitudinal modes we still have around 4000 modes experiencing gain and oscillating in the cavity. We will use this case as a baseline and the dynamics that follow will be compared to it. Now we will add a extra loop to the laser that will provide external time-delayed feedback to the laser cavity.

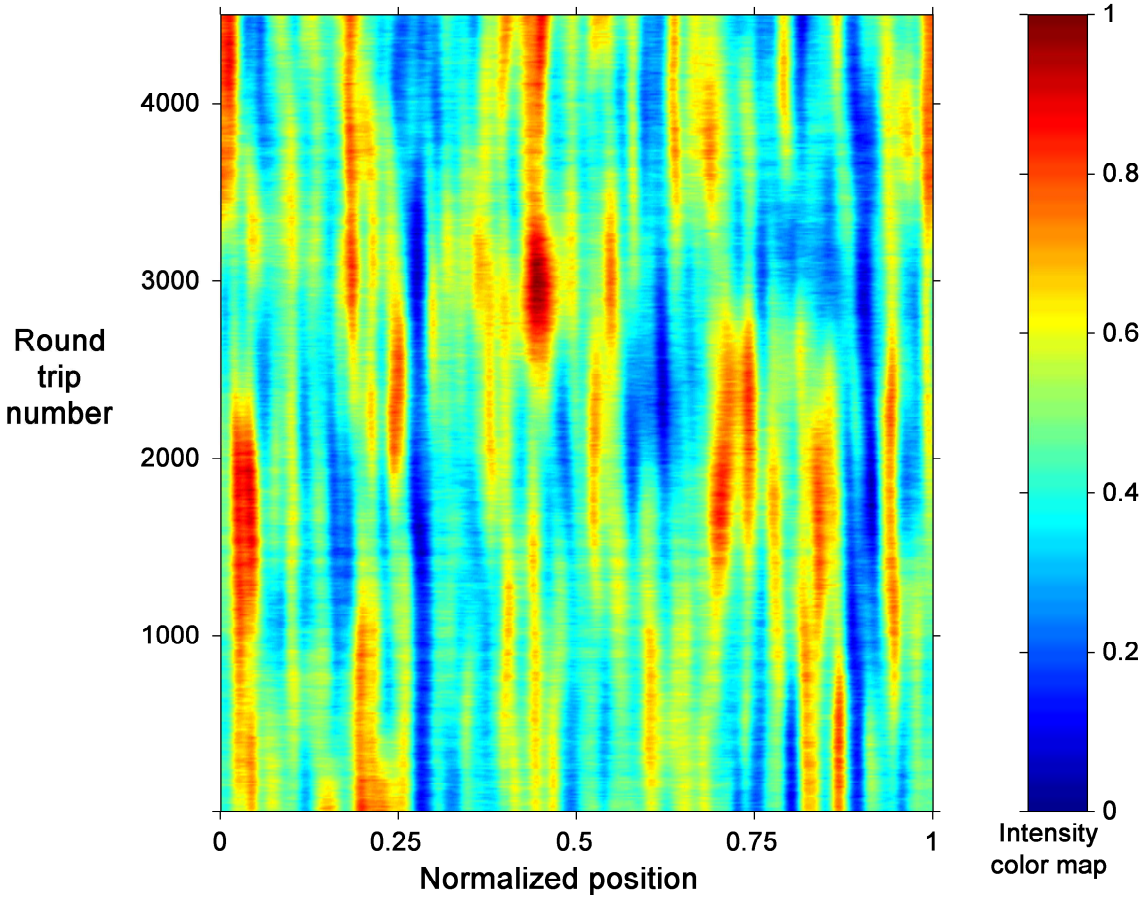

Figure 2.6: Spatiotemporal representation for the EDFRL. The data is interpolated with nine points between each position data point. Every tenth round trip is plotted.

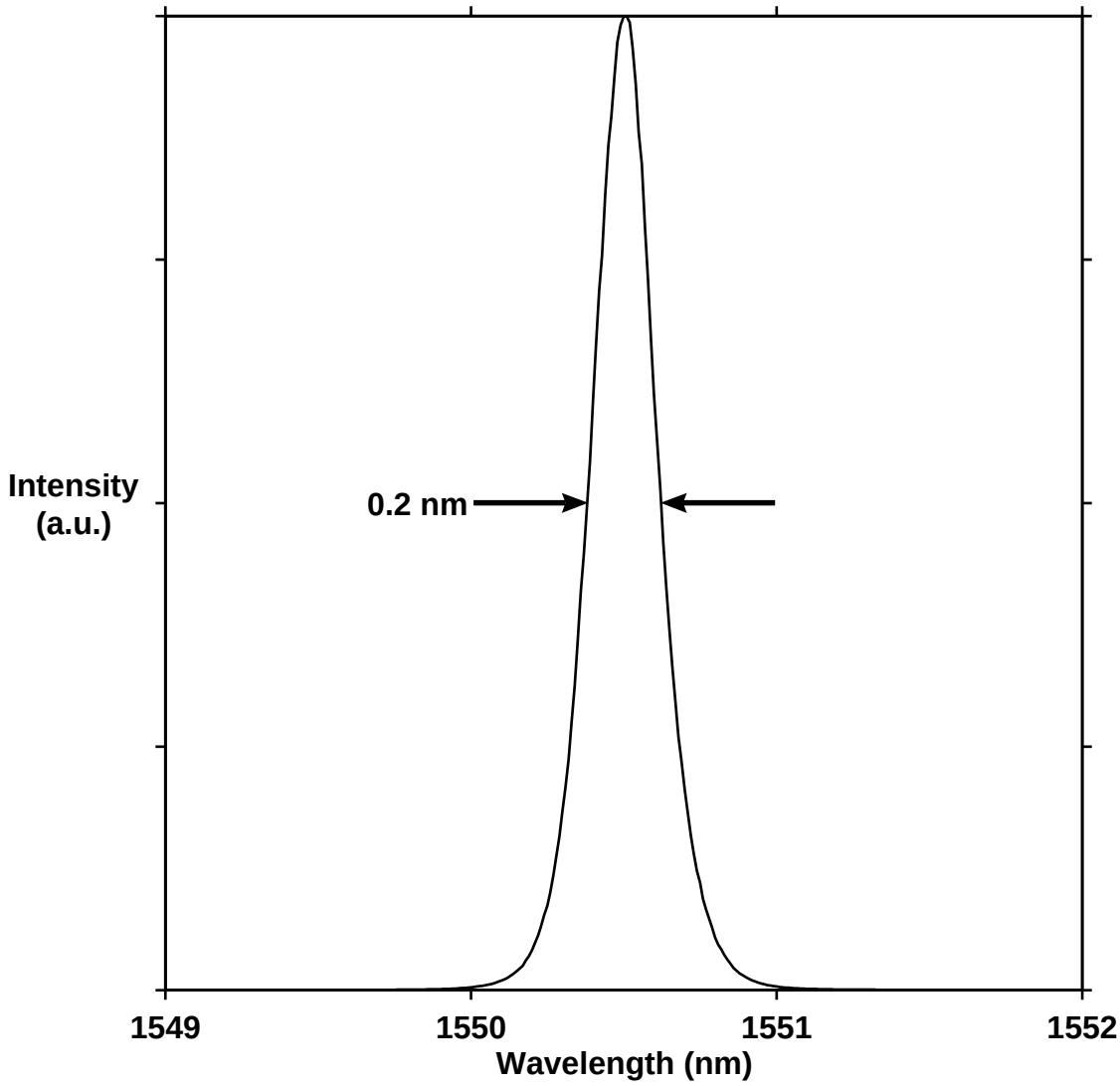

Figure 2.7: Optical spectrum of the EDFRL. The full width at half maximum (FWHM) is shown on the plot.

Chapter 3

Fiber ring laser with a second feedback loop

3.1 Overview

This chapter will describe the feedback loop experiment, present the data with different methods of visualizing the dynamics, and then present the Karhunen-Loève analysis we used to quantify the complexity of the dynamics. The chapter will end with the results of the complexity analysis.

3.2 Experimental set-up

Figure 3.1 shows the setup for the experiment with a second feedback loop. The laser is tuned to operate at a wavelength of 1550 nm using the polarization controller. The laser was pumped at 8.0 times the threshold pumping rate. A 95/5 coupler is used to send light to OSC A to measure the intensity dynamics of the laser. OSC A is the LeCroy LC534AM oscilloscope which measures the signal from a New Focus model 1811 IR 125 MHz bandwidth photodetector. The light is sampled every 1 ns. The OSA measures the optical spectrum of the laser. A 70/30 coupler pulls out 30% of the light in the ring and sends it through a feedback line into which different lengths of fiber are inserted to change the delay time of the feedback. A second 70/30 coupler is used to inject the light from the feedback line back into the

ring.

The feedback line length varied from 14 m to 38 km which corresponds to delay times of 0.068 μs to 187 μs. This wide range of times allows us to see how the dynamics are affected when τ is less than, comparable to, and larger than τ_r. A variable attenuator is used to adjust the light levels in the line. This allows us to correct for the different losses in the different lengths of the feedback line and to keep the coupling strength constant for all of the data runs. The coupling strength, κ, is defined as the ratio of the power injected into the ring from the feedback line to the power in the ring. In the experiments described here we chose $\kappa = 1\%$. This coupling strength was set by the losses in the couplers and connectors and the amount of absorption in the 38 km line. We used the variable attenuator to keep κ constant. The light intensity in the feedback line is monitored with a Tektronix model TDS 3032 oscilloscope (OSC B) which reads the DC level of a New Focus model 1611 IR photodetector. Five 1 ms long time series are recorded for each delay time.

3.3 Fluctuation size and dynamical complexity of round trip patterns

We normalize the intensity time series by dividing each one by its mean. The means of the intensities remained constant. The dynamics of the normalized laser output is plotted over five round trips in Fig 3.2(a) for the laser without feedback. Figure 3.2(b)-(i) show the results for the laser with feedback of various delays. The plots in the figure have been offset for clarity. Without the offset they would all

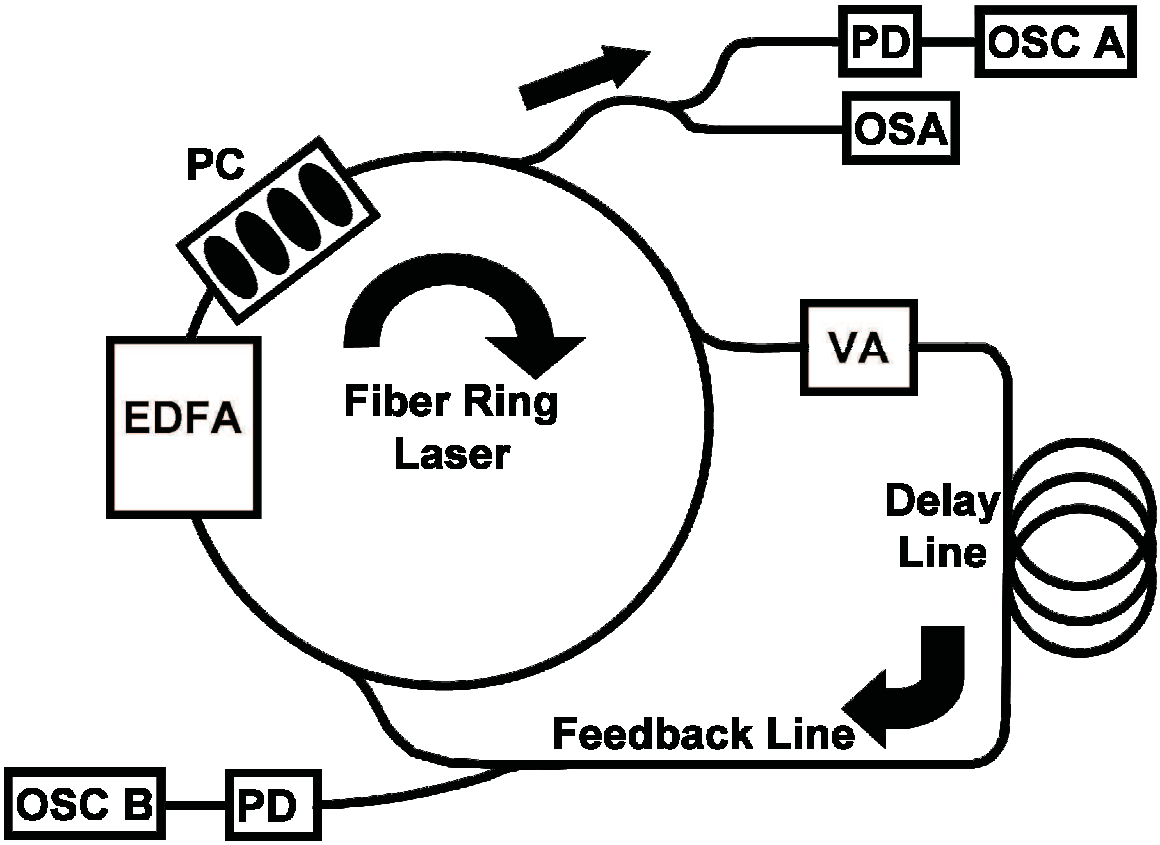

Figure 3.1: Experimental setup for the laser with feedback. The arrows show the direction of light propagation through the ring and the feedback line. EDFA, erbium-doped fiber amplifier; PC, polarization controller consisting of a sequence of linear polarizer, quarter wave plate, half wave plate, and quarter wave plate; VA, variable attenuator; PD, photodetector; OSC A, oscilloscope used to measure laser dynamics; OSC B, oscilloscope used to monitor the feedback line; OSA, optical spectrum analyzer.

be centered on an intensity of 1 due to the normalization. Periodic dynamics is usually observed at a delay time τ of 1 μs or less, with periods much smaller than τ_r. Figure 3.2(c) and (d) display patterns with a period of approximately half the round trip time and one round trip respectively. The last three plots show that the dynamics repeat over a round trip, that the magnitude of the fluctuations increases for large delays, and that the patterns within a round trip are very irregular compared at long delays to the regular oscillations at shorter delays. Note that the intensity scale is the same for all plots, so the relative increase in intensity fluctuations is conspicuous. The power spectra of the five round trip time series are shown in the right hand column of Fig. 3.2. The DC component at 0 MHz was omitted for clarity. The spectrum for the case without feedback (Plot 3.2(a)) has harmonics of the round trip time. Plots (b)-(f) have spectra with specific peaks that are indicative of periodic dynamics. Plots (g)-(i) again show harmonics of the round trip time as the dynamics become more complicated.

To quantify the increase in fluctuation size seen in the time series plots, we examine the variation of the means and standard deviations of the time series with varying feedback delay time. The means remain approximately constant over the changing delay, but the standard deviations increase. To compare the increase we calculate the ratio of the standard deviation of the time series to its mean. Figure 3.3 shows the mean and standard error of these ratios for the five time series taken at each delay. The standard deviation increases from 3% of the mean for the laser without feedback and shorter delay times to around 35% of the mean at long delays. To interpret these results, we should note that the feedback level has been carefully

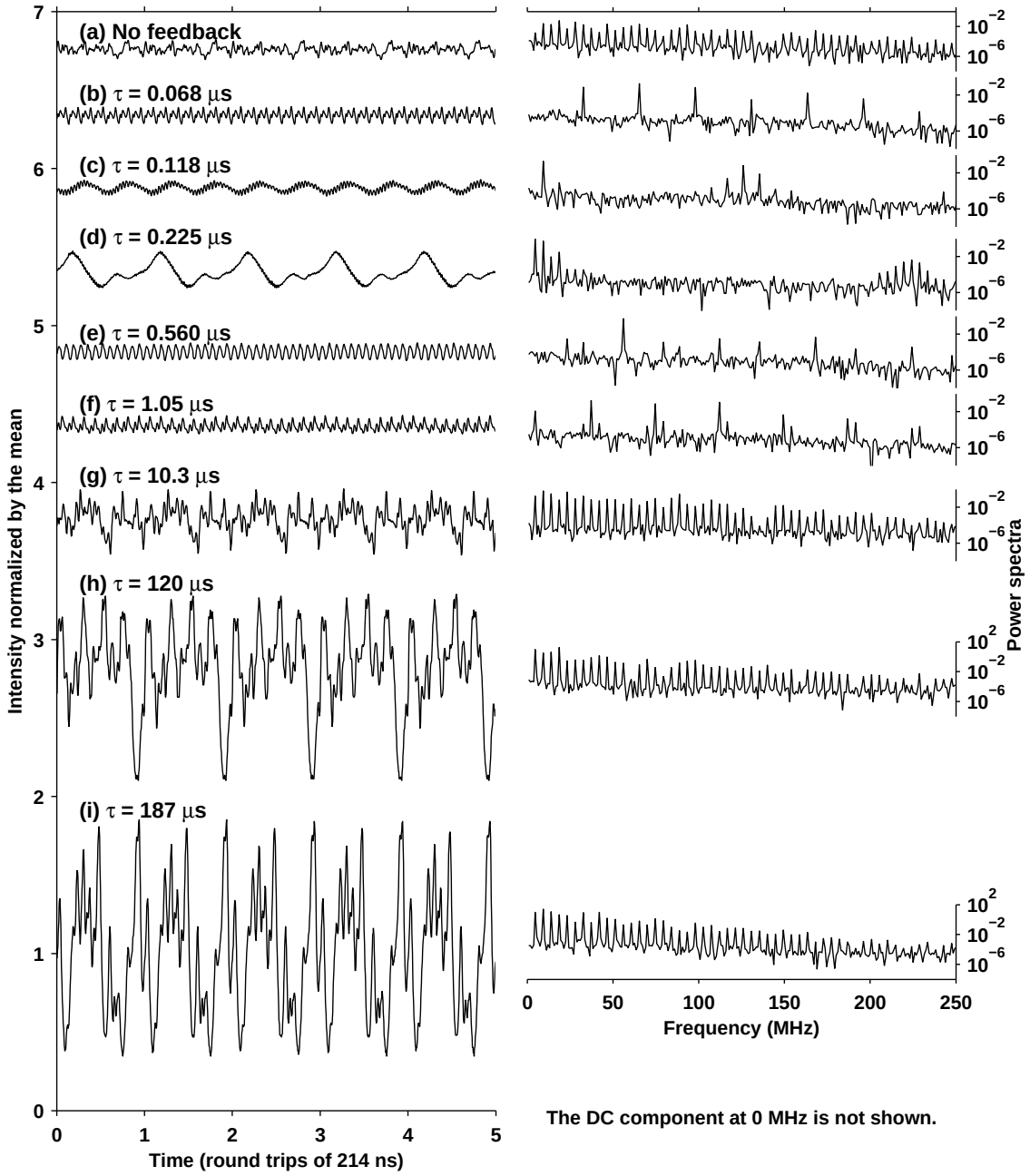

Figure 3.2: The left column shows laser output intensities over five round trips where the round trip time is 214 ns. Each time series is normalized by its mean, and the plots are offset for clarity. (a) is for the laser without feedback. (b)-(i) are for the laser with feedback with the time delay, τ, given. The right hand column has power spectra of the five round trips shown for each time series. The DC component at 0 Hz has been omitted to better show the detail of the spectra.

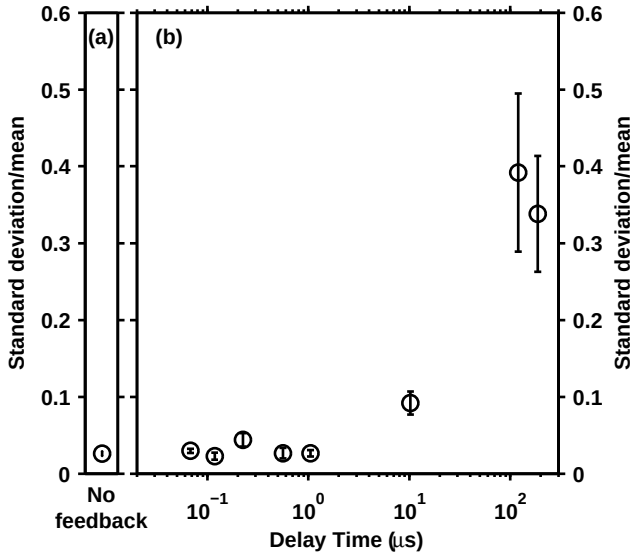

Figure 3.3: (a) Ratio of standard deviation to the mean for the laser without feedback. (b) Ratio of standard deviation to the mean for the laser with feedback of different delays. The error bars in both plots are the statistical standard error based on a sample set of five 1 ms long time series.

maintained constant at $\kappa = 1\%$. The dramatic rise in the standard deviation is seen to occur at the 10 μs delay. The large error bars on the last two data points are caused by the changing temporal patterns for the intensity time series that were sampled to compute the standard deviation. These statistics describe the size of the fluctuations but do not tell us about the complexity or variability of the round trip patterns.

Another way to visualize the data to help us see the complexity of a round trip pattern is with a time delay embedding. These are usually used to reconstruct the phase space of a dynamical system and require careful calculation of the number of dimensions needed to unfold the attractor and the proper delays to use to sample the

data [37, 38]. Because the goal of our embeddings is merely to obtain a qualitative sense of the complexity of a round trip pattern, we use only three dimensions and do not calculate the number of dimensions needed to represent the phase space dynamics. The resulting trajectories are projections into three dimensions of the true phase space trajectories. Each point of the trajectory has three coordinates: $I(t-T_1-T_2)$, $I(t-T_1)$, and $I(t)$ where $I(t)$ is the intensity at time t and T_1 and T_2 are the embedding delays. Following the procedure recommended in Ref. [76] the first minimum of the mutual information of the time series is used to determine the embedding delay. The average mutual information (in bits) between time series X and time series Y, $M(Y;X)$ is

$$M(Y;X) = \sum_{x,y} p(x,y) \log_2 \left[\frac{p(x,y)}{p(x)p(y)} \right], \tag{3.1}$$

where $p(x,y)$ is the joint probability that $X = x$ and $Y = y$ and $p(x)$ and $p(y)$ are the probabilities that $X = x$ and $Y = y$ respectively. In our case, $X \rightarrow I(t)$ and $Y \rightarrow I(t-T_1)$. The mutual information gives the reduction in the uncertainty of Y for a given measurement of X [46]. The longer the delay, the more the coordinates will become uncorrelated. Using the first minimum gives us the most independent pair of coordinates that are not completely uncorrelated. To find the second embedding delay, T_2, we use the minimum of the mutual information of Z given X and Y [77]. We calculate the second delay using the minimum of the mutual information

$$M(Z;X,Y) = \sum_{x,y,z} p(x,y,z) \log_2 \left[\frac{p(x,y,z)}{p(x,y)p(z)} \right], \tag{3.2}$$

where $p(x,y,z)$ is the joint probability that $X = x$, $Y = y$, and $Z = z$. For both Eqs. 3.1 and 3.2 the probabilities are calculated using histograms of the entire 1 ms

time series with 25 bins for each dimension. The intensities of each time series are re-scaled from 0 to 1 and the histogram applied over this range. The embedding delays calculated are used to qualitatively examine the complexity of a typical round trip pattern for each feedback delay case.

Figure 3.4 shows the time delay embedding of the first round trip shown in each of the plots in Fig 3.2. Comparing plot (a) for the laser without feedback to plots (b)-(f) shows that feedback with a short delay simplifies the round trip patterns. The cloud in plot (a) is transformed into more organized structures of loops. The high frequency features in Fig 3.2(c) and (d) appear in Fig 3.4(c) and (d) as small oscillations overlaid on the low frequency structures. In plot (g) where the time delay is increased to 10.3 μs, the round trip patterns become complex again and are qualitatively similar to plot (a), but with larger fluctuations. At long delays the fluctuation size increases dramatically, and so plots (h) and (i) require a larger scale to display the data. These two plots also show that the round trip structure is more complex at long delays than at short delays. The time delay embeddings provide a qualitative view of the complexity of a round trip. Now we proceed to examine the long term evolution of the round trip patterns over the entire time series.

3.4 Spatiotemporal representation

The time series show that the round trip time is still an important parameter in the dynamics and time delay embeddings show a variety of round trip patterns. Now we want to consider the evolution of the round trip patterns. Figure 3.5

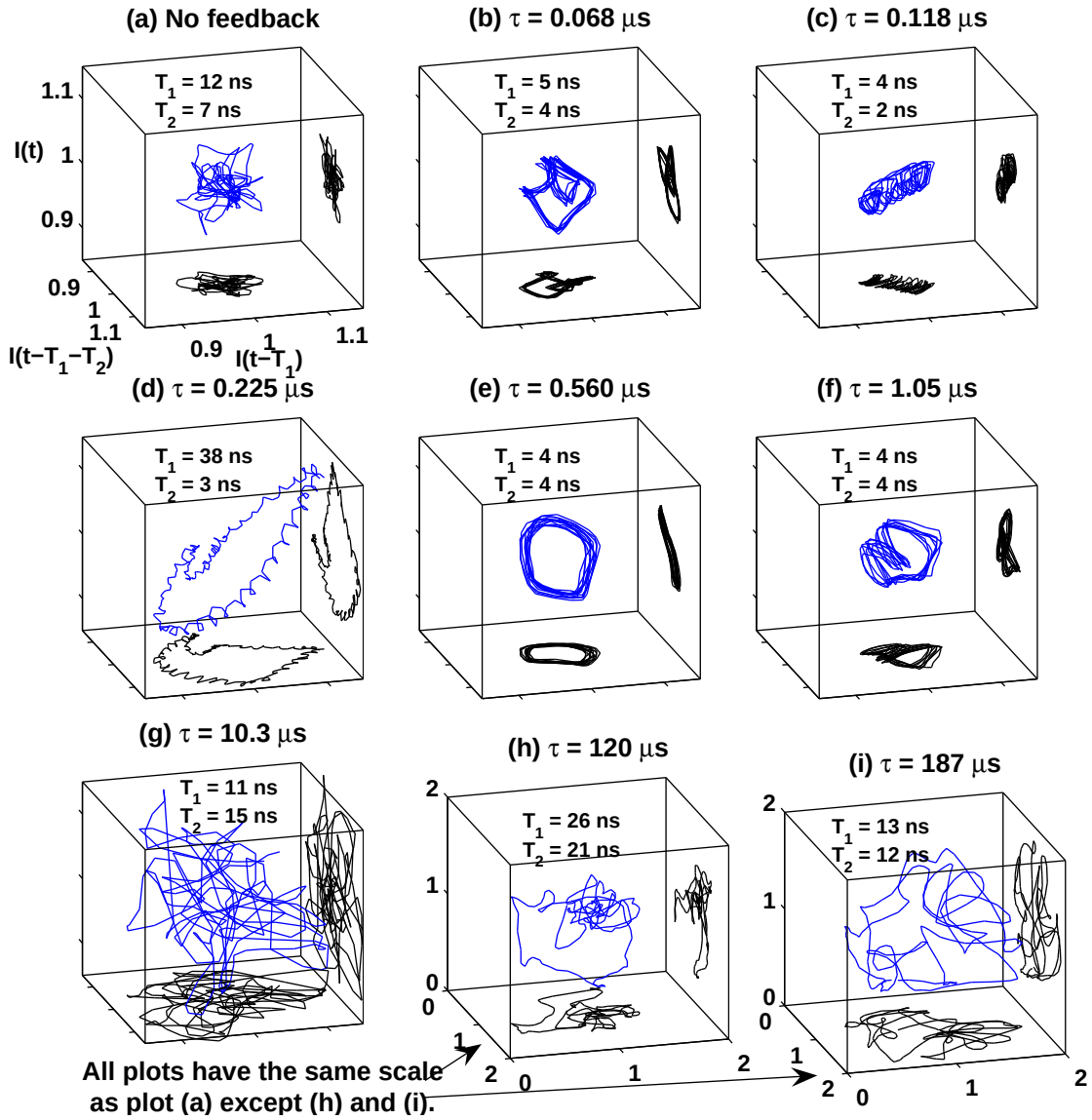

Figure 3.4: Time delay embeddings of the first round trip shown in Fig. 3.2. Plot (a) is for the laser without feedback. The rest of the plots are for the laser with feedback with the time delay, τ, given. The embedding delays, T_1 and T_2, are also given. The blue curve is the 3-D trajectory, and the black curves are 2-D projections onto the bottom and right sides of the plots. The data points are 1 ns apart. Plots (a) through (g) have the same scale. Plots (h) and (i) have a larger scale due to the larger fluctuations in these time series. The plots are centered about 1 because each time series was normalized to its mean.

shows spatiotemporal representations for the first 4500 round trips (using every tenth round trip) of the time series plotted in Fig. 3.2 and Fig. 3.4. The data shown in the previous figures occurs around round trip 2340 in the plots of Fig. 3.5. The variety of dynamics produced when changing the feedback delay time is illustrated clearly. Figure 3.5(a) is a reprinting of Fig. 2.6 and shows the dynamics of the laser without feedback for comparison. Figures 3.5(b), (e), and (f) show patterns of vertical stripes. These stripes correspond to the regular oscillations seen in Fig. 3.2 for these cases. The round trip patterns can be stable for hundreds of round trips, and certain oscillation frequencies are maintained even as the patterns evolve into new periodic patterns. Figure 3.2(c) shows a high frequency oscillation overlaid on a low frequency oscillation. The corresponding power spectrum shows a peak at twice the round trip frequency and group of three peaks near 125 MHz. Figure 3.5(c) shows us that the low frequency oscillation is not a harmonic of the round trip frequency. The low frequency peaks travel along the ring while the high frequency peaks stay in place. The same phenomenon occurs in Fig. 3.5(d), but it is hard to see the high frequency oscillation because it has a small amplitude. It is visible in the power spectrum as a collection of peaks near 225 MHz and can also be seen in the time delay embedding in Fig. 3.4(d). Analysis of the power spectra for these two cases shows that the high frequency oscillations are harmonics of the frequency corresponding to a period of 213.95 ns, and the low frequency oscillations are harmonics of the frequency corresponding to 214.22 ns. This could be caused by two polarization states that oscillate in the cavity simultaneously at different wavelengths due to the birefringence in the fiber. Figure 3.5(g) shows that the

regularity of the round trip pattern is lost for longer delays. Figures 3.5(h) and (i) show how the character of the plot changes for the longest time delays. Closer examination reveals that two-dimensional features repeat themselves with a period equal to the feedback delay. While looking at the data on the scale of a round trip shows a complex pattern, the spatiotemporal representation shows that these patterns quickly vanish but reappear hundreds or even a thousand round trips later. The spatial position of the patterns shifts because τ is not commensurate with τ_r. The time scale of the delayed feedback is being imprinted on the dynamics.

The long τ time series show repetition of a pattern with a period of τ. Figure 3.6 shows the full 1 ms time series from which the data in Fig. 3.5(h) and (i) was extracted. The case for the laser without feedback is shown for comparison, and bars of length τ are shown on the plots for the cases with feedback. The spatiotemporal representations in Fig. 3.5 (h) and (i) show that these long time scale patterns have complex round trip patterns. These round trip patterns evolve and reappear over 100 μs later as the overall pattern repeats every τ. The long pattern is essentially stored in the long transmission lines in the characteristics of the light moving through the lines. As the signal is fed into the second laser cavity, it is "processed" to reproduce the intensity pattern.

3.5 Karhunen-Loève decomposition and spatiotemporal complexity

The complexity of the dynamics can be quantified by taking KL decompositions of the spatiotemporal representations. The procedure [43, 55, 74, 78] is

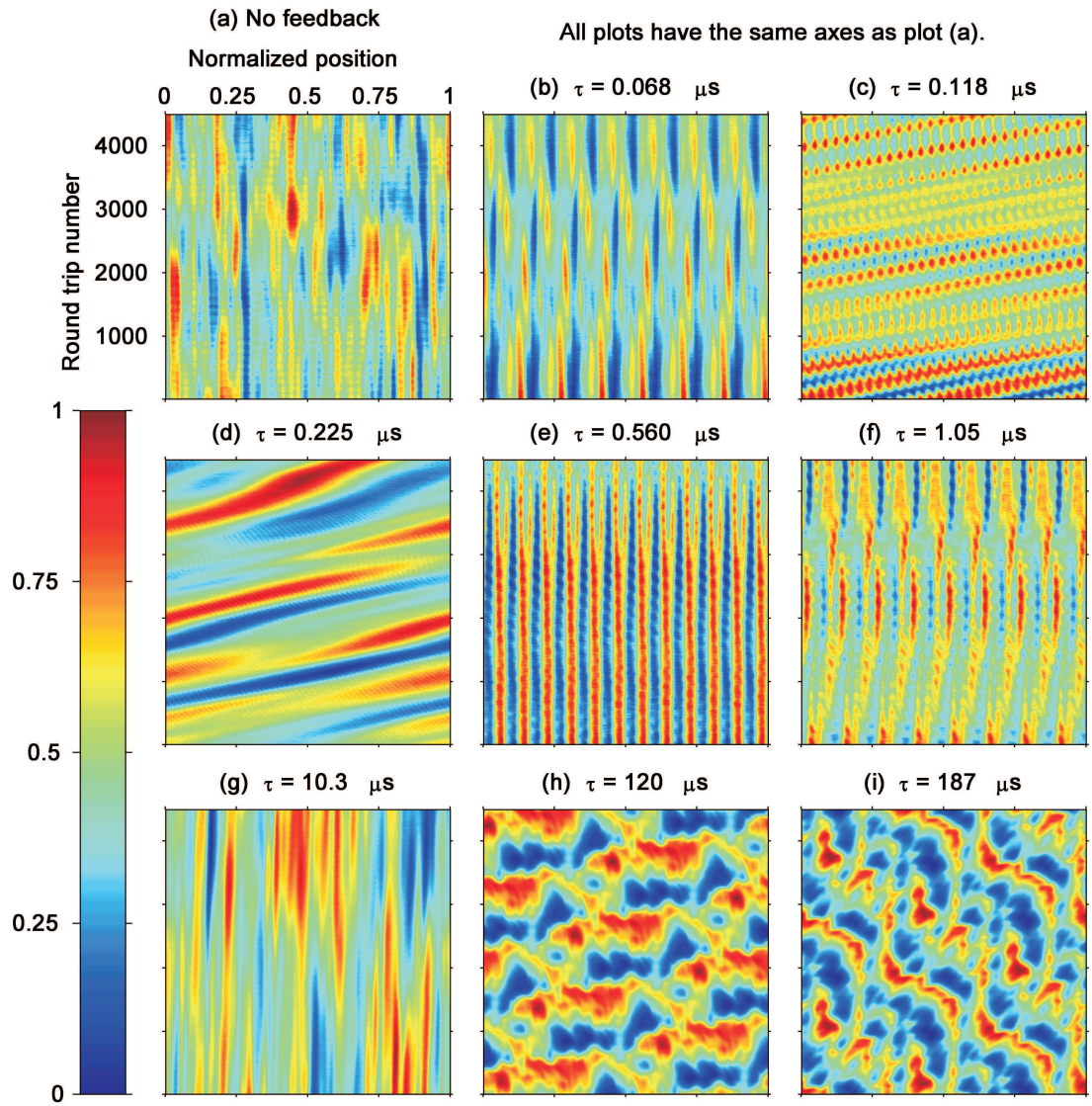

Figure 3.5: Spatiotemporal representations of the intensity dynamics for a laser with (a) no feedback and (b)-(i) feedback with the time delay, τ, listed. The laser intensities are rescaled from 0 to 1 for each time series, with the color bar indicating the value of the normalized intensity on the plots. All plots have the same axes as plot (a). Every tenth round trip is plotted.

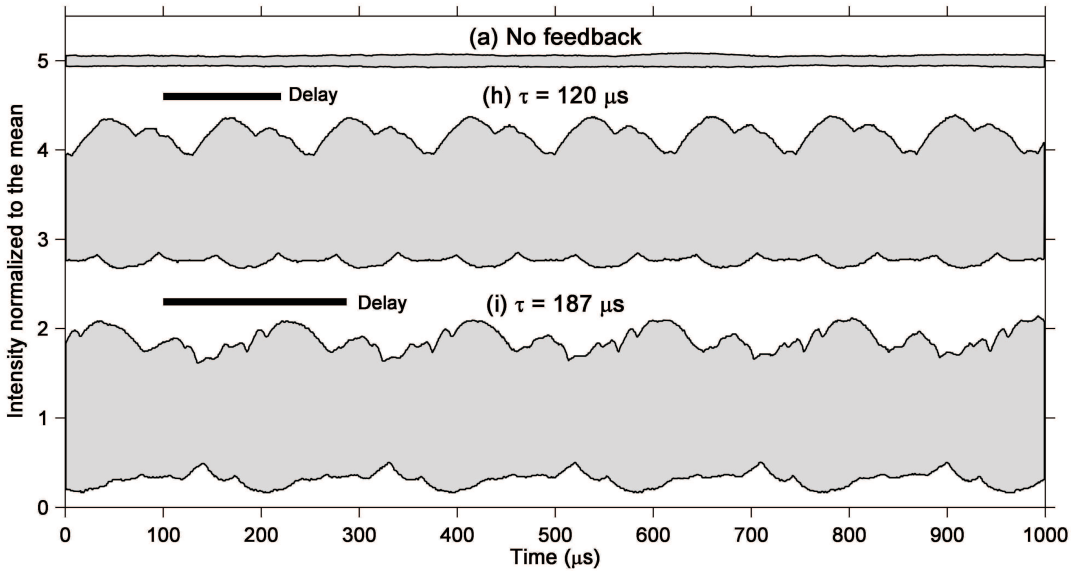

Figure 3.6: Envelope of the full 1 ms time series of the intensity dynamics for a laser with (a) no feedback and (h)-(i) feedback with the time delay, τ, listed. The labeling corresponds to the plots in previous figures. (a) and (h) are offset for clarity. The bars on plots (h) and (i) visually show the length of τ for each plot.

performed on a set of spatiotemporal data $u(x_j, n_t)$ which is a discrete array of data with each point indexed by a position around the ring, x_j, and a round trip number, n_t. First, for each value of x_j we subtract the mean for that position j averaged over all n_t. Next, we compute the covariance matrix, $\mathbf{K}$, with elements

$$K(x_j, x_{j'}) = \langle u(x_j, n_t) u(x_{j'}, n_t) \rangle \tag{3.3}$$

where the angle brackets refer to time averaging. Then we calculate the eigenvalues $\tilde{\lambda}_i$ and eigenvectors ψ_i of $\mathbf{K}$. The eigenvectors are orthogonal KL modes that describe a spatial pattern of the intensity over a round trip. The original data can be written in terms of an expansion

$$u(x_j, n_t) = \sum_i \alpha_i(n_t) \psi_i(x_j) \tag{3.4}$$

that uses the KL modes, $\psi_i(x_j)$, as its basis. Each mode has a coefficient, $\alpha_i(n_t)$, that weights the impact of that mode on the round trip pattern at round trip n_t. The coefficients as a function of time are calculated with $\alpha_i(n_t) = \sum_j u(x_j, n_t)\psi_i(x_j)$ where

$$\langle \alpha_i(n_t) \alpha_k(n_t) \rangle = \tilde{\lambda}_i \delta_{ik}. \tag{3.5}$$

$\tilde{\lambda}_i$ is the eigenvalue corresponding to KL mode i and δ_{ik} is the Kronecker delta function. The coefficients come from projections of the data onto the KL modes, so the larger the eigenvalue the more the KL mode represents the structure of the round trip pattern. The modes with the largest eigenvalues will be the most important in the expansion of Eq. 3.4 so we order the eigenvalues from largest, $\tilde{\lambda}_1$, to smallest, $\tilde{\lambda}_n$, and normalize them by the sum of all the eigenvalues. These normalized eigenvalues, λ_i, will be used to determine the complexity of the data.

The KL decomposition is considered optimal in the sense that the KL modes form the orthogonal basis that minimizes the error that arises when the expansion in Eq. 3.4 is truncated. The direction of the first basis vector is selected such that the variance of the data is maximized along it. The second basis vector is selected to maximize the variance subject to the constraint that it is orthogonal to the first vector. Subsequent basis vectors are chosen similarly and the result is that the variance is "condensed" within as few basis vectors as possible [43]. Another way to express the optimality is that the KL basis minimizes the Shannon entropy, as calculated below, compared to all other bases [65]. The KL modes with large eigenvalues are important to the reconstruction of the data and we expect to see their influence often. In this sense the KL basis reduces the uncertainty of the data because it sharpens the eigenvalue distribution. This idea will be described more completely below.

Figure 3.7 shows the results of a KL decomposition on the spatiotemporal representation in Fig. 3.5(a) for the laser without feedback. Figure 3.7(a) is the spatiotemporal representation. Figure 3.7(b) shows three KL modes where KL mode 1 has the largest eigenvalue, KL mode 2 has the second largest eigenvalue, and KL mode 10 has the tenth largest eigenvalue. The KL modes for this case are complicated. The expansion coefficients are plotted in Fig. 3.7(c). The vertical axis is time as represented by the round trip number. KL modes 1 and 2 are large for long periods of time and KL mode 10 makes small contributions to the Eq. 3.4 expansion.

Figures 3.8, 3.9, and 3.10 show the KL decomposition for the laser with $\tau = 0.068$ μs, $\tau = 10.3$ μs, and $\tau = 120$ μs respectively. The first two KL modes

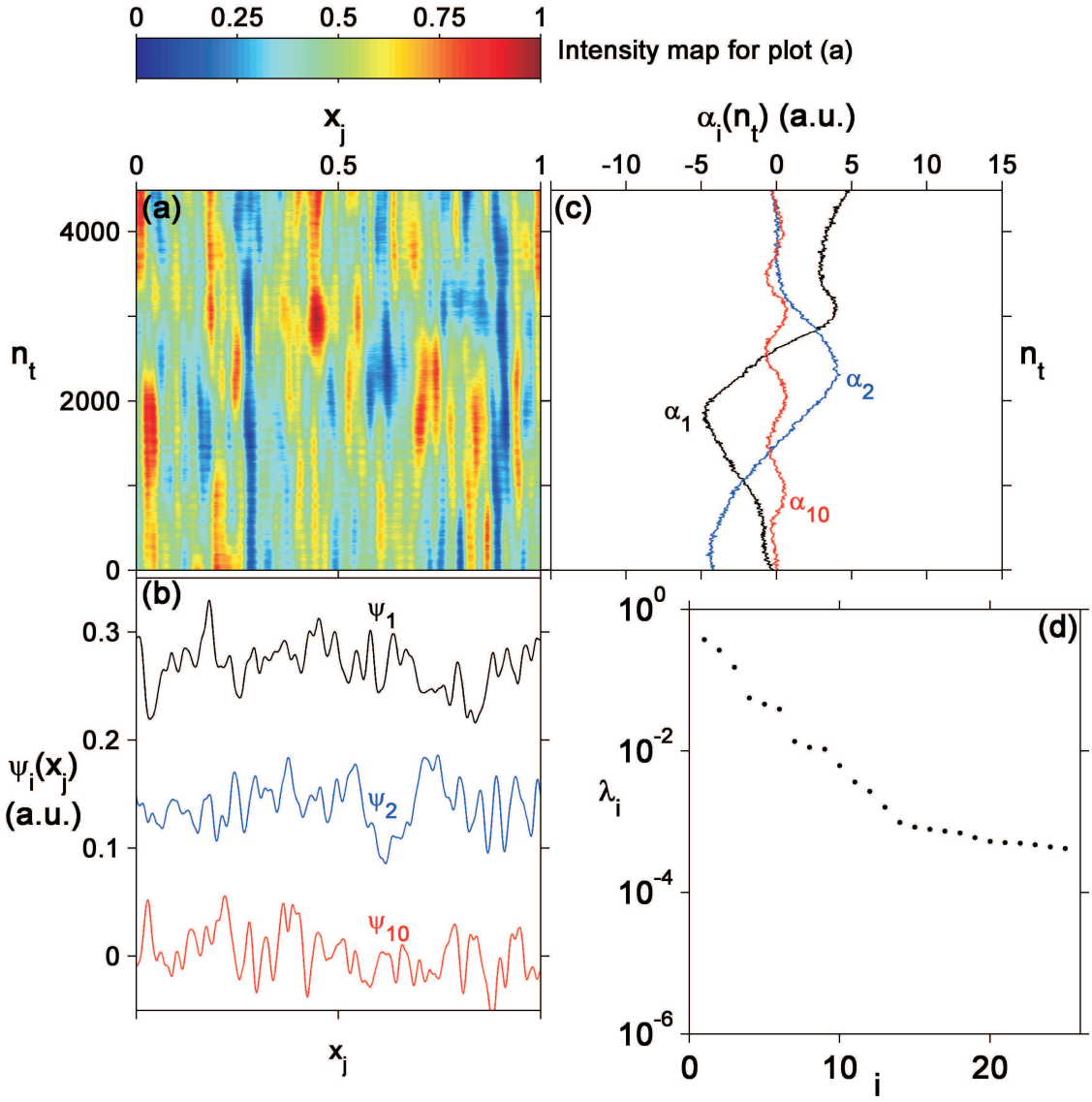

Figure 3.7: KL decomposition for the laser without feedback. (a) Spatiotemporal representation of the intensity dynamics from Fig. 3.5(a). (b) KL modes associated with the largest two eigenvalues and the tenth largest eigenvalue. Modes 1 and 2 are offset for clarity. (c) Expansion coefficients for the KL modes in (b). The vertical axis is time as represented by n_t. (d) Logarithmic plot of the 25 largest eigenvalues normalized by the sum of all the eigenvalues.

in Fig. 3.8(b) have structures that repeat seven times per round trip to match the spatiotemporal representation. Since α_{10} is very small, KL mode 10 makes very little contribution to the expansion in Eq. 3.4. Figure 3.9 has very complex looking KL modes and KL mode 10 is also unimportant to the expansion. In Fig. 3.10 the expansion coefficient oscillate as different modes are used at different times to build the 120 μs pattern and then recreate it over and over. The KL decomposition calculates round trip length patterns that are the most efficient at recreating the spatiotemporal data.

For comparison, Fig. 3.11 shows a KL decomposition of a spatiotemporal representation made up of uniformly distributed random numbers. The KL modes and expansion coefficients are very noisy as expected. The complex KL modes, $\psi(x)$, reflect the randomness along the spatial direction, and the noisy expansion coefficients, $\alpha(n_t)$, reflect the randomness along the time direction.

The first two orthogonal KL modes in Fig. 3.10(b) are approximately sinusoidal and shifted in phase by a quarter of a round trip. The eigenvalues for these two modes are also similar in size as shown in Fig. 3.10(d). The KL decomposition will produce Fourier modes for translationally invariant data [43, 56] so these modes may reflect the degree of translational symmetry in the data. Figure 3.10(c) shows that the expansion coefficients of the two KL modes oscillate and are generally antiphase to each other. Physically this behavior may be explained by previous work that shows the orthogonal polarization states of EDFRLs oscillate in an antiphase manner to each other [72, 79].

The first method of quantifying the complexity considers how many terms are

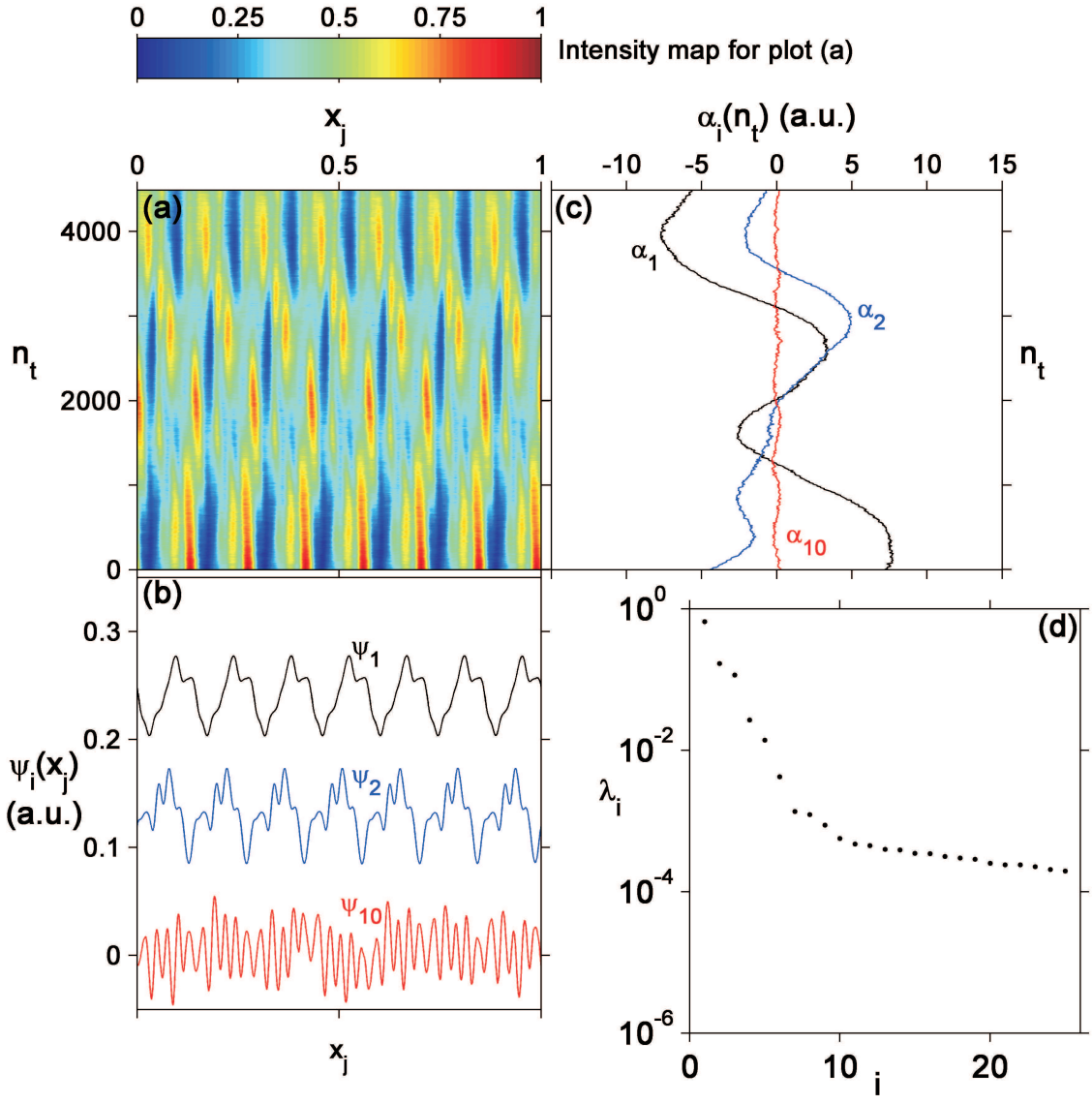

Figure 3.8: KL decomposition for $\tau = 0.068$ μs. (a) Spatiotemporal representation of the intensity dynamics from Fig. 3.5(b). (b) KL modes associated with the largest two eigenvalues and the tenth largest eigenvalue. Modes 1 and 2 are offset for clarity. (c) Expansion coefficients for the KL modes in (b). (d) Logarithmic plot of the 25 largest eigenvalues normalized by the sum of all the eigenvalues.

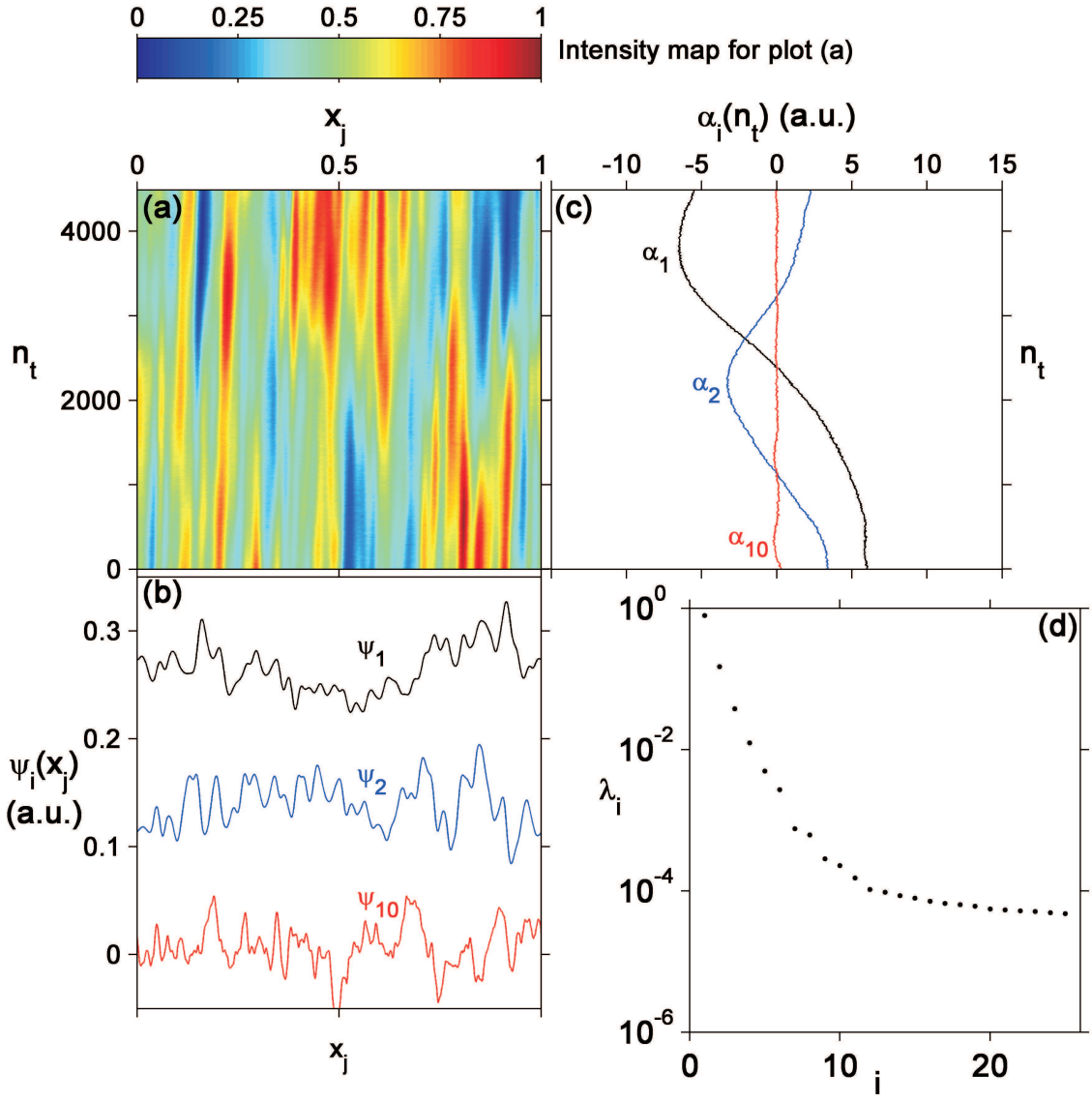

Figure 3.9: KL decomposition for $\tau = 10.3$ μs. (a) Spatiotemporal representation of the intensity dynamics from Fig. 3.5(g). (b) KL modes associated with the largest two eigenvalues and the tenth largest eigenvalue. Modes 1 and 2 are offset for clarity. (c) Expansion coefficients for the KL modes in (b). (d) Logarithmic plot of the 25 largest eigenvalues normalized by the sum of all the eigenvalues.

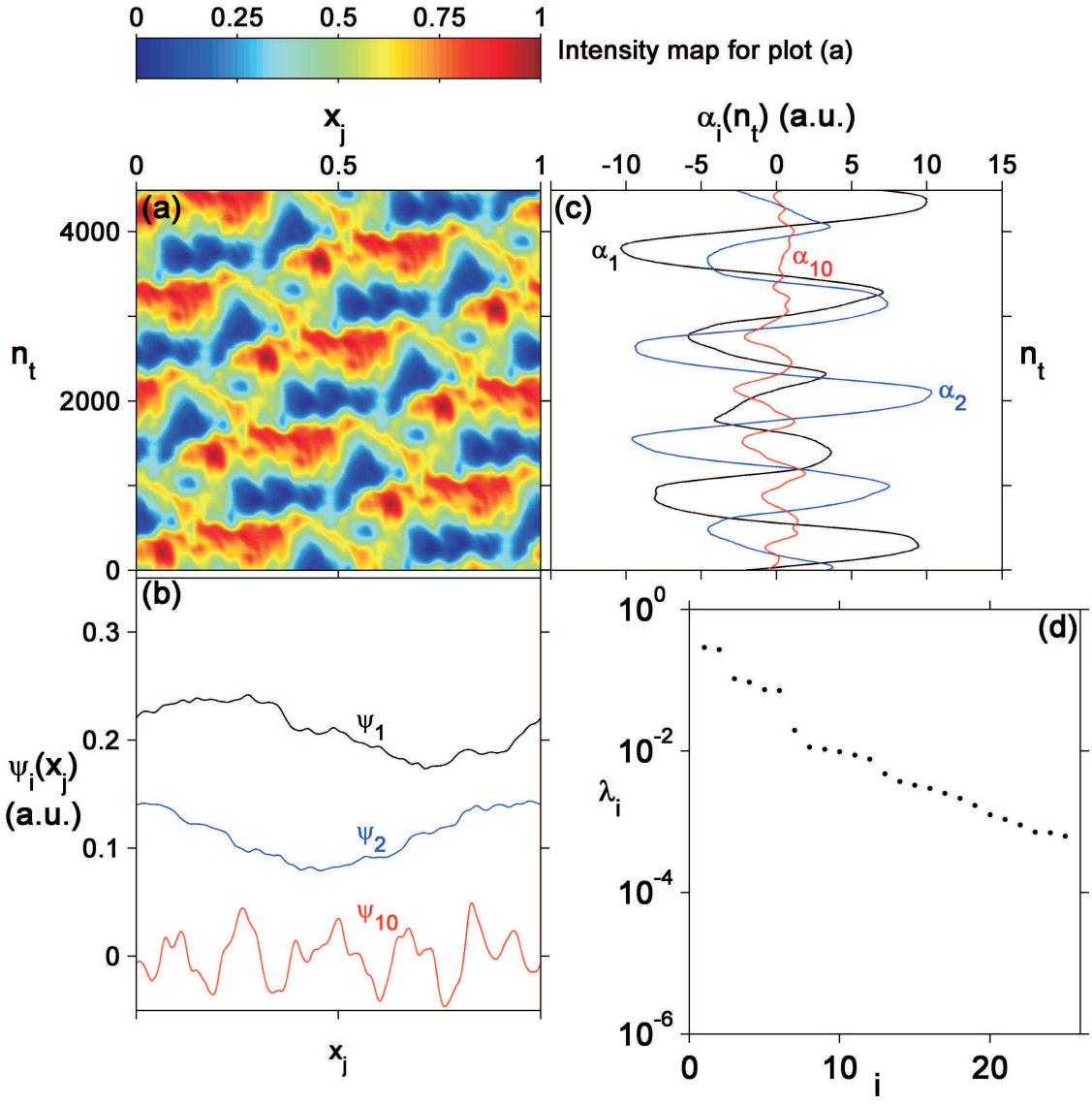

Figure 3.10: KL decomposition for $\tau = 120$ μs. (a) Spatiotemporal representation of the intensity dynamics from Fig. 3.5(h). (b) KL modes associated with the largest two eigenvalues and the tenth largest eigenvalue. Modes 1 and 2 are offset for clarity. (c) Expansion coefficients for the KL modes in (b). (d) Logarithmic plot of the 25 largest eigenvalues normalized by the sum of all the eigenvalues.

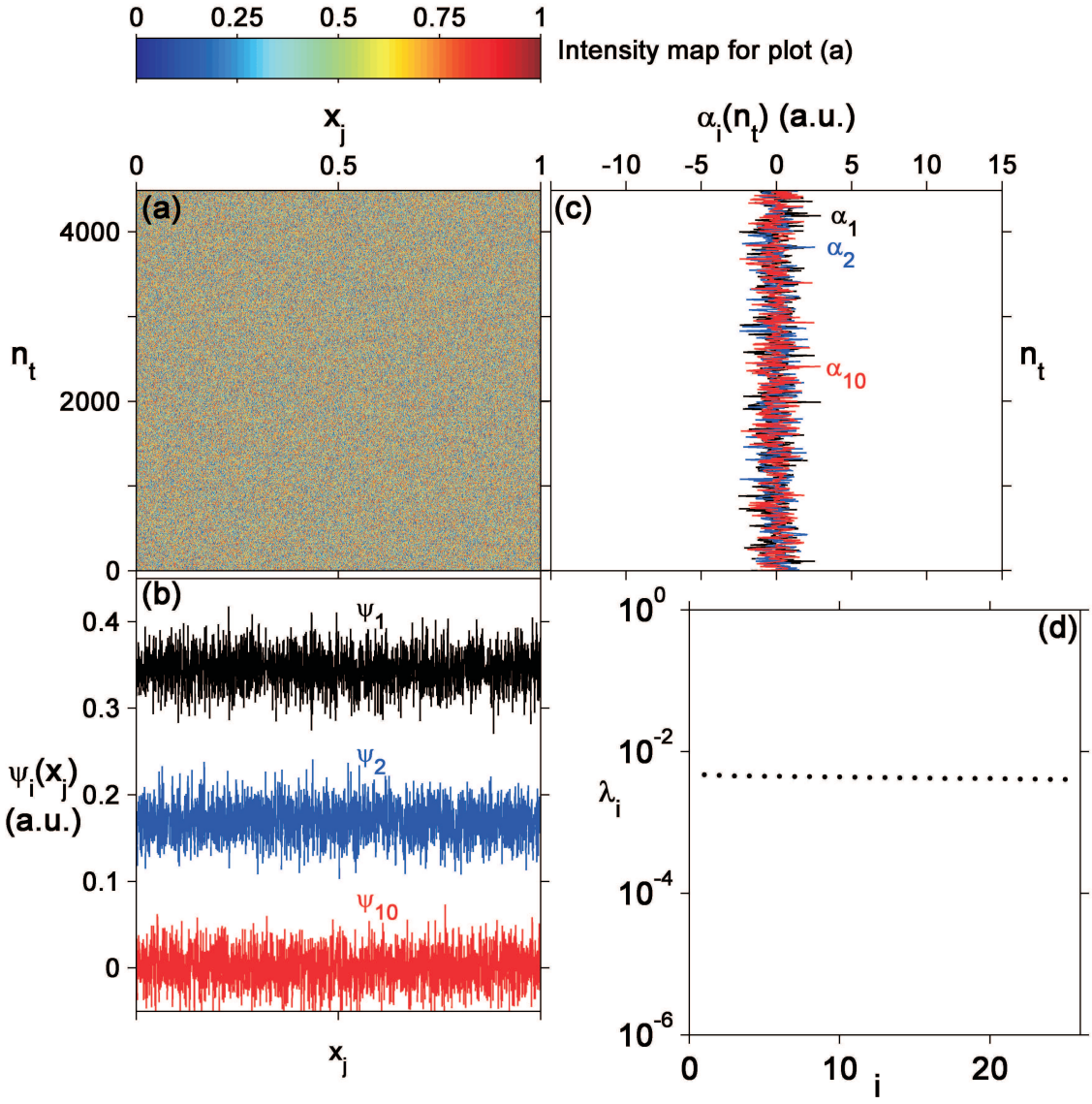

Figure 3.11: KL decomposition for uniformly distributed random data. (a) Spatiotemporal representation of uniformly distributed random data. The data has the same number of elements as the data in Fig. 3.5. (b) KL modes associated with the largest two eigenvalues and the tenth largest eigenvalue. Modes 1 and 2 are offset for clarity. (c) Expansion coefficients for the KL modes in (b). (d) Logarithmic plot of the 25 largest eigenvalues normalized by the sum of all the eigenvalues.

needed in the expansion in Eq. 3.4 to accurately reconstruct the original spatiotemporal data set [43, 55, 63, 64]. This number has been called the KL dimension, D_{KL}, in previous work [64]. The importance of each mode to the reconstruction is given by the eigenvalues, λ, through the relation in Eq. 3.5. Figure 3.7(d) shows a logarithmic plot of the eigenvalue spectrum for the 25 largest eigenvalues. The rate of decay is large for smaller i and then levels off at a smaller decay rate after about $i = 14$. Figures 3.8(d), 3.9(d), and 3.10(d) show the eigenvalue spectrum for the $\tau = 0.068$ μs, $\tau = 10.3$ μs, and $\tau = 120$ μs cases respectively. For Figs. 3.8(d) and 3.9(d) λ_1 is large and the eigenvalues decay more quickly than exponentially at first. This means that the expansion in Eq. 3.4 can represent the spatiotemporal data accurately with only a few terms. In comparison, Fig. 3.10(d) has a flatter slope and requires more terms in the expansion to accurately represent the spatiotemporal data. The eigenvalue spectrum for the random data in Fig. 3.11(d) is very flat showing that no single KL mode dominates the dynamics. Data with stable structures can be represented by a few KL modes, but changing round trip patterns will require more KL modes to describe the evolving structures.

To determine how many modes, D_{KL}, are needed, we sort the normalized eigenvalues in decreasing order and compute

$$S(N) = \sum_{i=1}^{N} \lambda_i \tag{3.6}$$

until $S(N) \geq 0.95$, where $i = 1$ corresponds to the largest eigenvalue, $i = 2$ corresponds to the second largest eigenvalue, and so on. The smallest value of N that meets the criteria is the value assigned to D_{KL}. The 95% level was chosen arbitrarily.

Figure 3.12(a) shows the average number of KL modes for the laser without feedback needed to represent the intensity waveforms with 95% accuracy. Figure 3.12(b) is the same but for the laser with different feedback delays. The number of modes needed for accurate representation increases for larger delays as the delay time scale impresses itself on the dynamics, the round trip patterns vary more from round trip to round trip, and the overall dynamics becomes more complex. For comparison we generated 10 sets of uniformly distributed random data with the same number of pixels as our spatiotemporal representations such as that shown in Fig. 3.11(a). We found $D_{KL} = 392.7 \pm 0.2$, which is significantly larger than any of our other results.

This method suffers from the arbitrary 95% accuracy requirement and the difficulty in selecting this value when the eigenvalue distributions have a knee in them such as the one around $i = 12$ in Fig. 3.7(d). The second method uses the entire eigenvalue spectra through a connection with information theory. We interpret λ_i to be probability to find the system in the state ψ_i [43, 65] and calculate the Shannon entropy [46, 66, 67], H, with

$$H \equiv -\sum_i P_i \log_2 P_i = -\sum_i \lambda_i \log_2 \lambda_i. \tag{3.7}$$

This measure of complexity considers the KL modes to be states of the system. If only one KL mode described the system ($\lambda_1 = 1, \lambda_{i\neq 1} = 0$) then $H = 0$ because our uncertainty about the state of the system would be zero. For comparison we calculated H for the 10 spatiotemporal representations of random numbers. These images had an average value of H of 8.6595 ± 0.0005 bits per pixel [80]. The maximum for H occurs when the probabilities are all equal which results in a flat

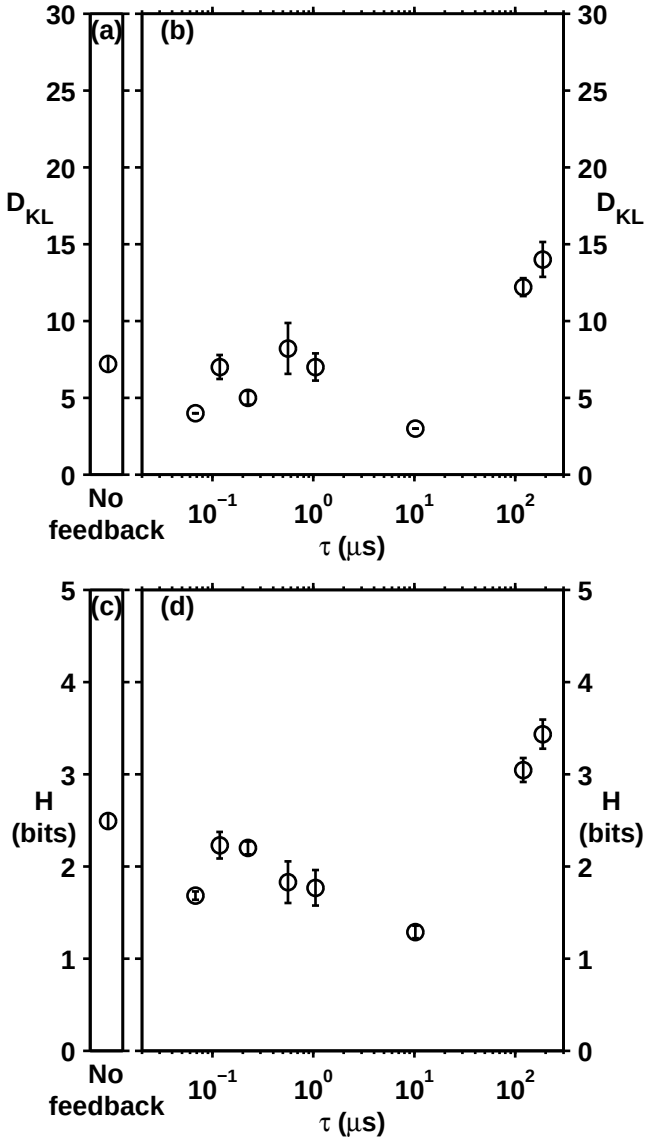

Figure 3.12: (a)Number of KL modes needed to reconstruct the spatiotemporal plot for the laser without feedback to 95% accuracy. (b) Number KL modes needed for 95% accurate reconstruction of the spatiotemporal plot for the laser with feedback of different delays. (c) Shannon entropy for the laser without feedback. (d) Shannon entropy for the laser coupled with feedback of different delays. The error bars in these plots are the statistical standard error based on a sample set of five.

eigenvalue spectrum. In this case Eq. 3.7 reduces to the logarithm of the number of KL modes which gives a theoretical maximum of $H = 11$ bits per pixel for our data. Figure 3.12(c) shows the Shannon entropy for the laser without feedback and Fig. 3.12(d) shows the entropy for the laser with delayed feedback. The Shannon entropy decreases from 2.5 for the laser without feedback to a minimum of about 1.3 for the laser with feedback delayed by 10 μs. The Shannon entropy went up for the longest two delays to around 3. These results are similar to the results from calculating D_{KL} in the first method except here we see a decrease in complexity for short delays that was not observed in Fig. 3.12(b).

The spatiotemporal representations in Fig. 3.5 show a variety of dynamics. Some of the data shows structures that do not move spatially around the ring and other data show structures that are traveling around the ring. Techniques have been developed to "center" the data before doing the KL decomposition [81]. Essentially the data is moved into the frame of the traveling wave so the analysis can focus on the structure that is moving through the ring. It would be interesting to apply this technique to our data in the future.

3.6 Optical spectra

The optical spectra of the laser are presented in Fig. 3.13. The optical spectrum analyzer data acquisition is not fast enough to capture the optical spectra on the time scale of a round trip. Each peak is a spectral envelope of the wavelengths measured over the scan time, which is around one second per sweep. Due to the

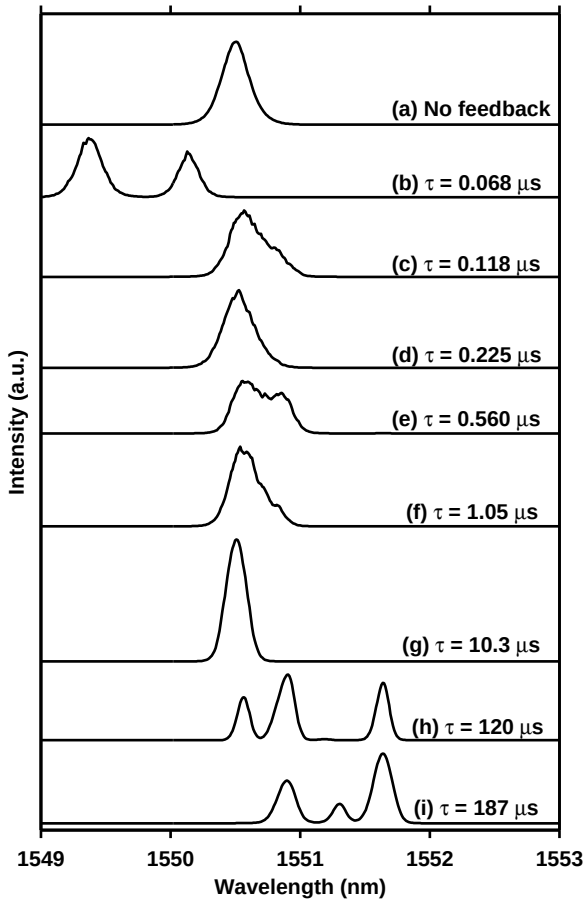

Figure 3.13: Optical spectra of the laser. (a) is for the laser without feedback. (b)-(i) are for a laser with feedback with a delay, τ, as listed.

length of the laser cavity, there are thousands of cavity modes that fit within the envelopes. The bandwidth resolution of the spectrum analyzer is 0.1 nm. When feedback is applied, we often notice the presence of additional peaks, and the lasing frequency is generally spread over a wider wavelength range than for the laser without feedback. When the spectral peaks are separated we can usually observe that the width of the peaks are comparable to case (a) without feedback.

3.7 Summary of Chapter 3

Adding an extra feedback loop to the EDFRL generates a variety of dynamics depending on the feedback delay. The size of the intensity fluctuations increases as the feedback delay increases. The time series and time delay embeddings show us that the round trip patterns are get more complex for longer feedback delays. The spatiotemporal representations provide a picture of the dynamics over both short and long time scales. Using Karhunen-Loève decomposition we can quantify the complexity of the dynamics using two different measures. The dynamics get more complex at the longest delays where $\tau \gg \tau_r$. Next, we will mutually couple two EDFRL's together and examine the dynamics.

Chapter 4

Two mutually coupled ring lasers

4.1 Overview

Now we will mutually couple two fiber ring lasers together and vary the time delay of the coupling between them. The organization of this chapter is similar to the previous chapter. First comes a description of the experiment followed by different ways to visualize the dynamics. The chapter will end with the results of the complexity analysis.

4.2 Experimental set-up

We now want to compare the measurements for a single laser with feedback with what is observed when two fiber lasers are mutually coupled together with a delay, τ. We repeat the measurements and analysis of the previous section with two coupled ring lasers whose cavity lengths are within 1 cm of each other and have $\tau_r = 213.9$ ns. The two EDFAs were built together with matching characteristics. The two active erbium-doped fibers in them are identically doped, 17 m long, and matched in length to within 1 mm. The two lasers are still physically different and so are not identical. Each fiber has its own unique inhomogeneities that cannot be prevented or really measured. Laser 1 is the laser used in the previous experiment

and has a threshold $I_{th} = 15.7$ mA. Some of the components in Laser 2 have more loss so laser 2's threshold is $I_{th} = 26.1$ mA. These values come from linear fits of intensity vs. pump current data like that shown in Fig. 2.4. The experimental setup is shown in Fig. 4.1. The power in both rings was matched by adjusting the pumps, and the variable attenuators were used to match the power in the coupling lines. Laser 1 was pumped at 4.7 times its threshold pumping level, and laser 2 was pumped at 4.6 times its threshold. The coupling strength, κ, was 1.7% for this setup and kept constant by using the variable attenuators. Extra fiber was added to the coupling lines to vary the coupling time, τ, from 0.050 μs to 120 μs. Ten time series of 1 ms were taken for each delay time and the Agilent 86141B OSA was used to measure the optical spectrum.

4.3 Fluctuation size and dynamical complexity of round trip patterns

The dynamics of the normalized laser output is plotted over five round trips in Fig 4.2(a) for the uncoupled lasers. The time series for laser 1 is offset above laser 2 for all plots in Fig. 4.2. The time series pairs are also offset for clarity since their means all lie at 1 due to the normalization. Figure 4.2(b)-(h) show the results for the mutually coupled lasers with the delays listed. The power spectra for laser 1 is shown in the left hand column. Like the single laser with feedback, the coupled laser system shows a variety of dynamics, including regular patterns in (b)-(f). A superposition of patterns with high and low frequencies is seen in (e), making a transition to complicated patterns repeating every round trip in (g) and (h). The

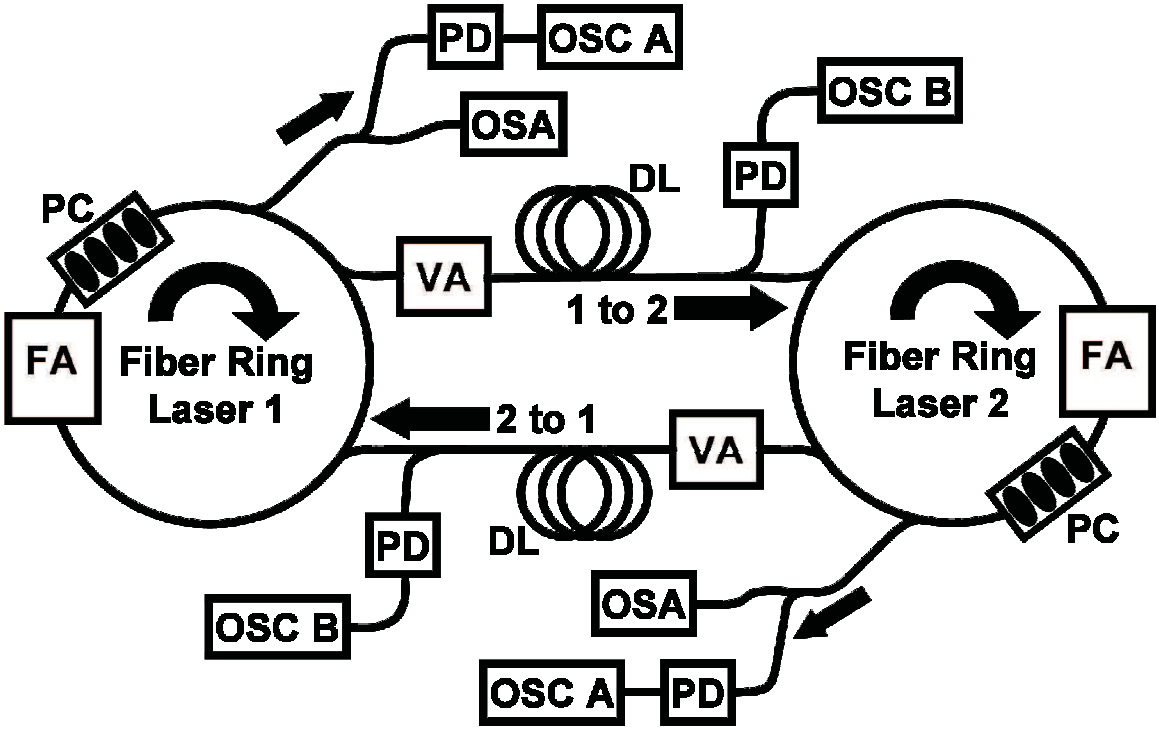

Figure 4.1: Experimental setup for two mutually coupled lasers. The arrows show the direction of light propagation through the rings and the coupling lines. FA, erbium-doped fiber amplifier; PC, polarization controller; VA, variable attenuator; DL, delay line; PD, photodetector; OSC A, oscilloscope used to measure laser dynamics; OSC B, oscilloscope used to monitor the coupling lines; OSA, optical spectrum analyzer.

size of the fluctuations increases for the coupled lasers even at the shortest delays.

To quantify the increase in fluctuation size we plot the ratio of the standard deviation to the mean as before. Figure 4.3 shows the ratios for the mutually coupled lasers and also includes the data from Fig. 3.3 for comparison. In plot (a) there are two values for laser 1 because two sets of data were taken: one set with laser 1 set up for the feedback experiment and another set for laser 1 set up for the mutually coupled experiment. This was done to compare the mutually coupled results with the uncoupled laser operating under identical conditions. Primary differences between the two cases include different pump strengths and different tuning of the optical cavity with the polarization controllers. These were changed to match the power in the rings and the lasing wavelengths of the two lasers. The coupled lasers have larger fluctuations except at long delays when all three data sets are comparable. The ratio increases with increasing delay for the coupled lasers except when the delay time is 4 ns more than the round trip time. The fluctuations are the largest for this delay. Without coupling the system is constrained to repeat every round trip. With coupling, it also has to work with the delay time. If $\tau = \tau_t$, both of these demands on the dynamics are the same.

Next we examine the complexity of the round trip fluctuations for the mutually coupled lasers. The time delay embeddings for the first round trip plotted in Fig. 4.2 are shown in Fig. 4.4. All of the plots have the same axes as the plots in (a) for the uncoupled lasers. The scale is the same as in Fig. 3.4(h) and (i), and it is easy to see how the size of the fluctuations increases even for short delays. Plots (d) and (h) are partially clipped at this scale. If the scale is reduced, Fig. 4.2(a) is similar

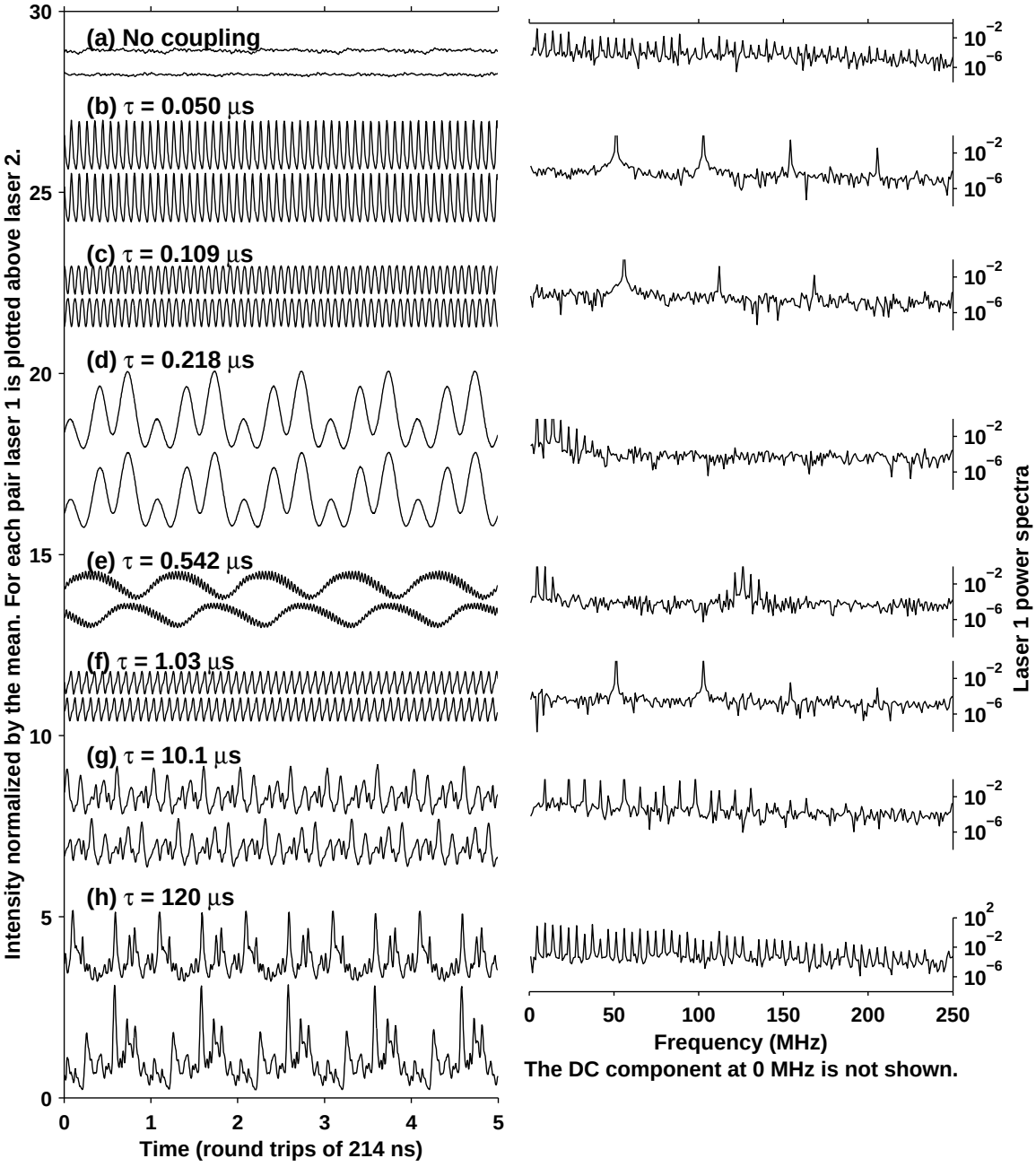

Figure 4.2: Laser output intensities over five round trips where the round trip time is 214 ns. Each time series is normalized to its mean. The plots are offset for clarity. For each pair of time series, laser 1 is offset above laser 2. (a) is for the lasers with no coupling. (b)-(i) are for the lasers mutually coupled with the time delay, τ, given. The right hand column has power spectra of the five round trips shown for each time series of laser 1. The DC component at 0 Hz has been omitted to better show the detail of the spectra.

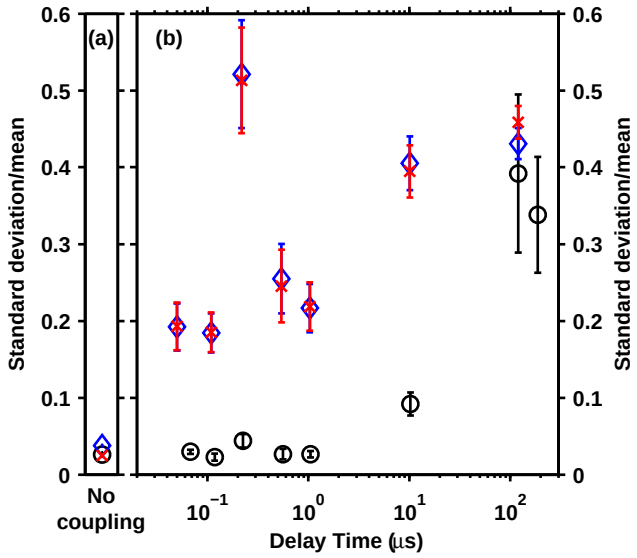

Figure 4.3: (a)Ratio of standard deviation to the mean for a single laser without feedback (∘) and laser 1 (blue ⋄) and laser 2 (red ×) when uncoupled. (b) Ratio of standard deviation to the mean for single laser with feedback (∘) and laser 1 (blue ⋄) coupled to laser 2 (red ×) with different delays. The error bars in both plots are the statistical standard error based on a sample set of ten for the coupled lasers and five for the single laser. The single laser data (∘) are reprinted from Fig. 3.3 for comparison.

to Fig. 3.4(a). For coupling time delays of 1 μs or less, the round trip patterns form regular repeating structures. For longer time delays, the round trip patterns become more complex as shown in (g) and (h).

4.4 Synchronization

Figures 4.2 (b)-(g) and 4.4 (b)-(g) show that the shape of the round trip patterns for laser 1 and 2 are similar for each pair for the short section of the time series shown. This provides evidence of synchronization over a few round trips, and we want to see if it holds over the entire 1 ms time series measured. To quantify the level of synchronization we calculate the cross correlation, $CC_{1,2}$, of the intensity time series of the two lasers using

$$CC_{1,2}(s) = \frac{1}{\sigma_1 \sigma_2} \frac{1}{J} \sum_{j=1}^{J} \left[I_1(t_j - s) - \langle I_1 \rangle \right] \left[I_2(t_j) - \langle I_2 \rangle \right] \tag{4.1}$$

where σ_i is the standard deviation of the entire time series for laser i, J is the number of data points of overlap after sliding time series 1 by the time shift s, $I_i(t)$ is the intensity of laser i at time t, and angle brackets refer to the time average of the entire time series. If $CC_{1,2} = 1$, then the time series are lag synchronized at the lag s. If $CC_{1,2} = -1$, then the signals are correlated but out of phase by half a cycle. If $CC_{1,2} = 0$ then the time series are uncorrelated and not synchronized. Since previous work [26, 27] found the lasers lag-synchronize with a shift $s = \tau$ when chaotic, we compute $CC_{1,2}(s)$ over a range of s that includes τ for each case.

Figure 4.5 shows the cross correlations of the time series plotted in Fig. 4.2 for different time shifts, τ_s. Plot (a) is for the uncoupled lasers, and the magnitude of the

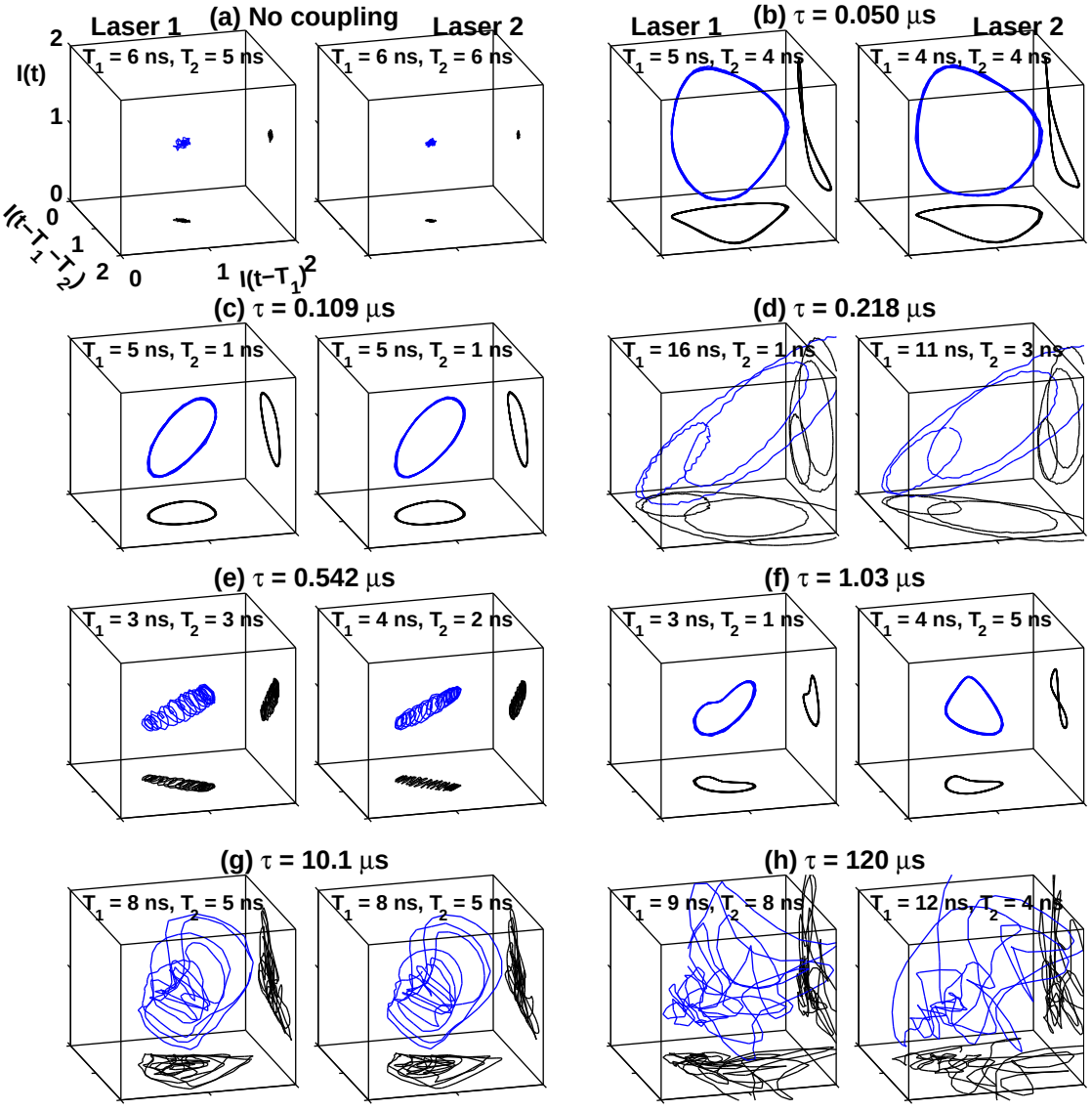

Figure 4.4: Time delay embeddings of the first round trip shown in Fig 4.2. Laser 1 is shown in the left box, and laser 2 is shown in the right box for each pair. Plot (a) is for the uncoupled lasers. The rest of the plots are for the mutually coupled lasers with the time delay, τ, given. The embedding delays, T_1 and T_2, are also given. The blue curve is the 3-D trajectory, and the black curves are 2-D projections onto the bottom and right sides of the plots. The data points are 1 ns apart. All plots have the same scale and are centered about 1 because each time series was normalized by its mean.

cross correlation is near zero. Plots (b)-(h) are for the lasers when they are mutually coupled. The delays are listed and also shown visually by a thick black bar. Note that the horizontal scale varies from plot to plot. Cross correlations (b), (c), and (e)-(g) are periodic with short periods compared to the coupling delays because the time series are periodic at those frequencies. Plots (b)-(h) show the leader/follower symmetry observed in the chaotic case, but the lasers are synchronized at τ only for plots (e) and (h). Plot (b) shows an isochronal case where the lasers are synchronized with no delay. Plot (c), (f), and (g) are not isochronal, but are not synchronized at τ either. For plots (b), (c), (f), and (g), $CC_{1,2}(s) \approx -1$ indicating the lasers are approximately half a cycle out of phase with each other at $s = \tau$. For plot (e) $CC_{1,2}(\tau)$ is at a maximum with respect to the low frequency variation of $CC_{1,2}(s)$ but is at a local minimum for the low frequency variation. For plot (d) $\tau_{rt} \approx \tau$, and synchronization occurs both with no delay and again at $s = \tau$. Because the round trip patterns change so slowly, it is impossible to tell if this case has lag synchronization or isochronal synchronization. Plot (h) shows no correlation except when $s \approx \pm\tau$. The two peaks are composed of spikes occurring every τ_r that are not visible in the resolution of the plot. The long shift required for correlation explains why the plots in Fig. 4.2(h) and 4.4(h) show no evidence of synchrony over the short section of the time series shown.

The synchronization behavior for the lasers under periodic conditions is different from the behavior observed under chaotic conditions in paper [26]. There the synchronization was always observed to occur with a shift of $s = \pm\tau$. Here the periodic nature of the dynamics causes synchronization to occur for $s < \tau$. Plot (b)

shows a case that appears to be isochronal that was not observed for the chaotic data, and plot (d) is a special case as described above. Case (h) has more complicated structures over a round trip, and its power spectrum in Fig. 4.6(h) shows no single strong periodicity dominating the time series. It follows the pattern for chaotic data that was observed in [26].

4.5 Spatiotemporal representation

As in the single laser case with feedback, we want to visualize the full time series of the mutually coupled lasers. This allows us to see the stability of the round trip patterns and the synchronization. Figure 4.6 shows spatiotemporal representations for the time series containing the data in Fig. 4.2 and Fig. 4.4 which were around round trip 2430. Again, every tenth round trip is plotted up to 4500 round trips. Figure 4.6(b)-(d) and (f) show very regular stable round trip patterns that persist for thousands of round trips. Fig. 4.6(e) shows a case of the superposition of low and high frequencies. Power spectra in Fig. 4.2 show two groups of peaks. The high frequency peaks are harmonics of the frequency corresponding to 213.95 ns and the low frequency peaks are harmonics that correspond to 213.78 ns. Fig. 4.6(h) appears random at first, but structures can be seen that repeat on the order of twice the round trip time. The peaks in the time series alternate from one laser to the other and it takes one delay time to move from one laser to the other. The result is a repeating pattern in the dynamics with a period of two delay times.

This repeating pattern is shown clearly in Fig. 4.7. These are plots of the

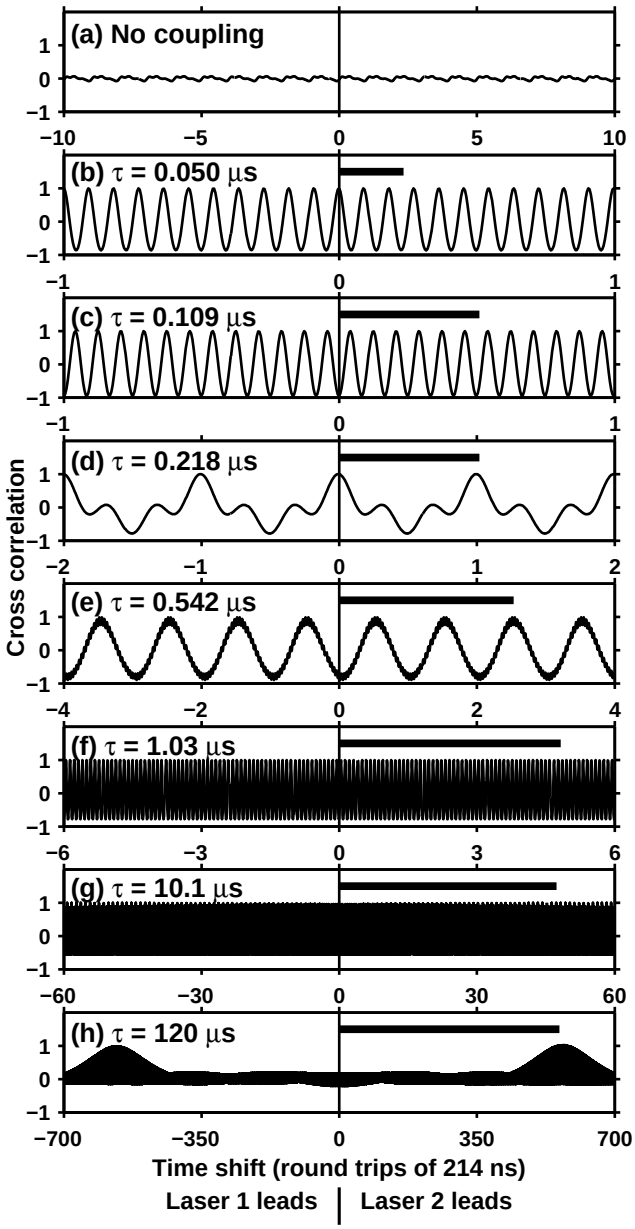

Figure 4.5: Cross correlations of the entire 1 ms intensity time series corresponding to the time series pairs shown in Fig 4.2. Plot (a) is for the uncoupled lasers. The rest of the plots are for the mutually coupled lasers with the time delay, τ, given. The thick black bars show the delay time graphically. Note that the horizontal scale of each plot changes. Negative(positive) time shifts correspond to laser 1(2) leading. Due to the symmetry a definite leader cannot be determined with these plots.

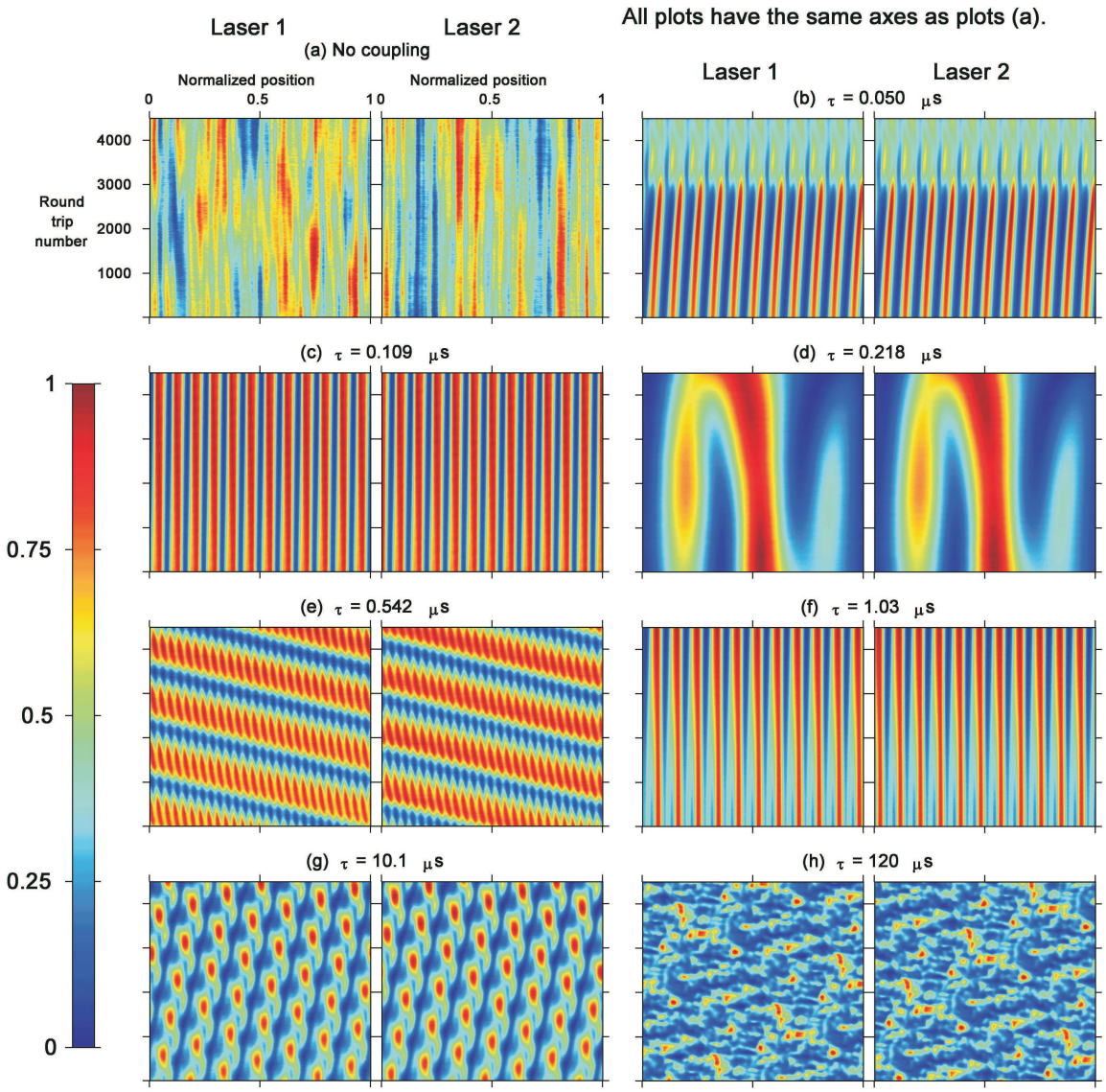

Figure 4.6: Spatiotemporal representations of the intensity dynamics of the mutually coupled lasers for (a) lasers 1 and 2 uncoupled and (b)-(h) with the coupling delays, τ, indicated. The laser intensities are re-scaled from 0 to 1 for each time series with the color bar indicating the value of the normalized intensity on the plots. All plots have the same axes as plot (a). Every tenth round trip is plotted.

envelope of the full 1 ms time series from which the data in Fig. 4.2 was extracted. The plots are labelled to match previous plots. The lasers are synchronized with a delay of τ. The repeating pattern of one laser is now 2τ. This is different than the single laser with feedback which had patterns repeating every τ as shown in Fig. 3.6(h) and (i). The bottom of Fig. 4.7 shows a five round trip time long section of the long data set for each laser. These two sections are offset by the time shift at which the cross correlation shown in Fig. 4.5 (h) is a maximum. The two data sets match and show that the lasers are delay synchronized at both long and short time scales.

Figures 4.6 and 4.7 are consistent with the cross correlation data presented in Fig. 4.5 (g) and (h). Figure 4.6(g) shows the repetitive pattern with a time scale smaller than τ that produces the multiple spikes in $CC_{1,2}$. Figures 4.6(h) and 4.7(h) show that the intensity pattern repeats with a period of τ, so $CC_{1,2}$ is near zero until $s = \tau$. There are spikes that occur every τ_r as well that are not visible in Fig. 4.5(h) due to the long time scale shown. As the time series becomes more complex the two lasers synchronize with a time shift equal to τ like the chaotic data in [26].

4.6 Karhunen-Loève decomposition and spatiotemporal complexity

As before we analyzed the spatiotemporal representations using KL decomposition to quantify the complexity of the dynamics. Figures 4.8, 4.9, 4.10, and 4.11 show the KL decomposition for the laser 1 spatiotemporal data shown in Fig. 4.6(a), (b), (d), and (h). The KL results in Fig. 4.8 for the uncoupled laser are similar to the results

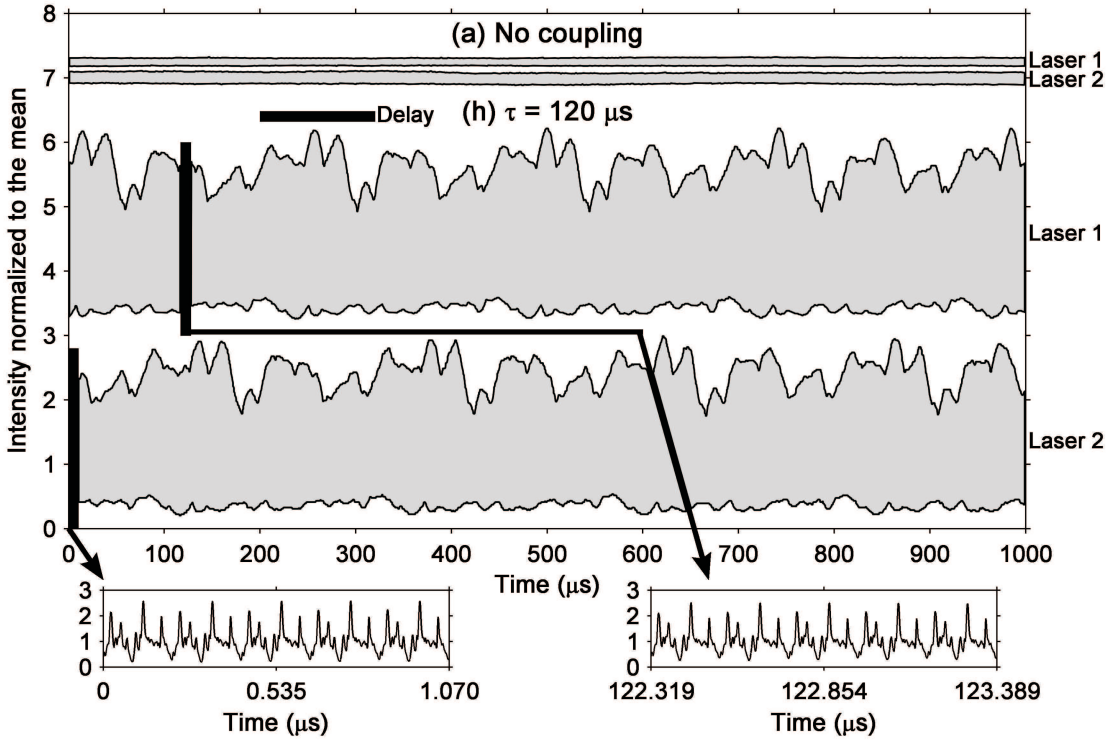

Figure 4.7: Envelope of the full 1 ms time series of the intensity dynamics for the lasers (a) when uncoupled and (h) when mutually coupled with $\tau = 120$ μs. The labeling corresponds to the plots in previous figures. For each pair laser 1 is offset from laser 2 for clarity. (a) is also offset from (h) for clarity. The bar on plot (h) visually shows the length of τ. The small plots on the bottom show a five round trip portion of the long time series from each laser. These small portions are offset by 122.319 μs which is the offset given by the maximum of the cross correlation in Fig. 4.5 (h). The data are delay synchronized over both the round trip and long coupling delay time scales.

if Fig. 3.7. In Fig. 4.9(b) we see KL modes that have structures that repeat 11 times a round trip. Plot (c) shows that KL mode 10 has a minimal impact on the expansion of Eq. 3.4. In comparison Fig. 4.10(a) has a different type of pattern that uses the modes shown in plot (b). KL mode 10 is more complex, but it also has a very small expansion coefficient. These last two cases have a large λ_1 and a rapid decay of the eigenvalue spectrum as seen in plot (d), indicating that only a few terms are needed in the expansion to reconstruct the spatiotemporal data accurately. Figure 4.11 shows the results for a more complex case. Here α_{10} is often comparable to α_1 and α_2 so KL mode 10 cannot be neglected in the expansion. Plot (d) shows that λ_1 is small and that the eigenvalue spectrum decay is slower compared to the other cases.

Figure 4.12(a) and (b) shows the average number of KL eigenvalues (KL modes) needed to reach the cut off of 95% of the sum of all the eigenvalues. Figure 4.12(c) and (d) show the Shannon entropy for the same cases [80]. The data from Fig. 3.12 is included for comparison. In plots (a) and (c) there are two values for laser 1 for the same reasons given for Fig. 4.3. For the coupled lasers the number of modes needed increases for larger delays just like the single laser case. At lower delays the mutually coupled system needs fewer KL modes to capture the simple periodic dynamics. At larger delays the mutually coupled system needs more KL modes than the single laser with feedback to represent the variety of round trip patterns produced. They show similar results with a decrease in complexity for short delays and an increase in complexity for the longest delays.

One striking difference is the complexity of laser 2 in plots (a) and (c) for the

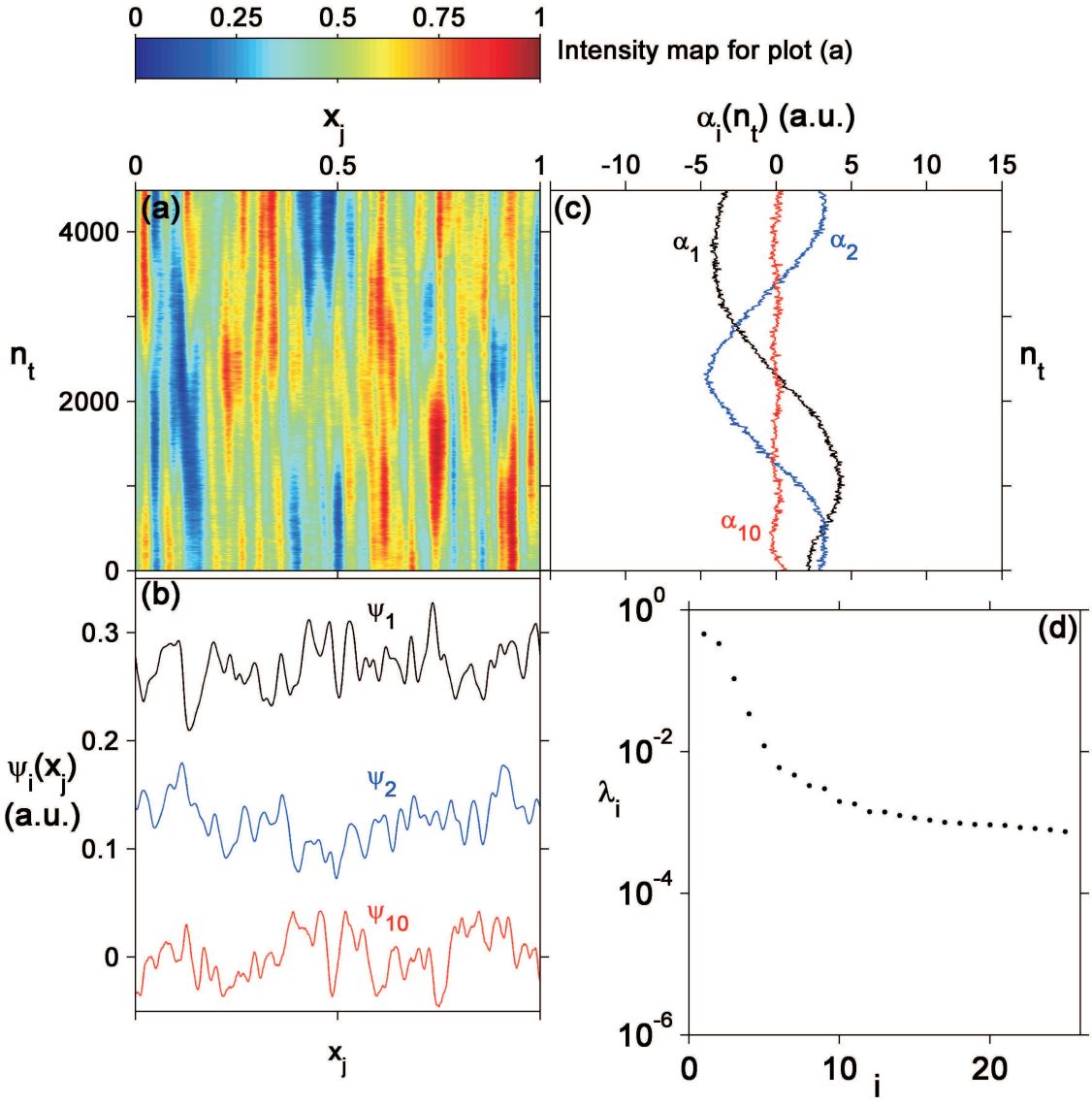

Figure 4.8: KL decomposition for laser 1 uncoupled. (a) Spatiotemporal representation of the intensity dynamics from Fig. 3.5(a). (b) KL modes associated with the largest two eigenvalues and the tenth largest eigenvalue. Modes 1 and 2 are offset for clarity. (c) Expansion coefficients for the KL modes in (b). The vertical axis is time as represented by n_t. (d) Logarithmic plot of the 25 largest eigenvalues normalized by the sum of all the eigenvalues.

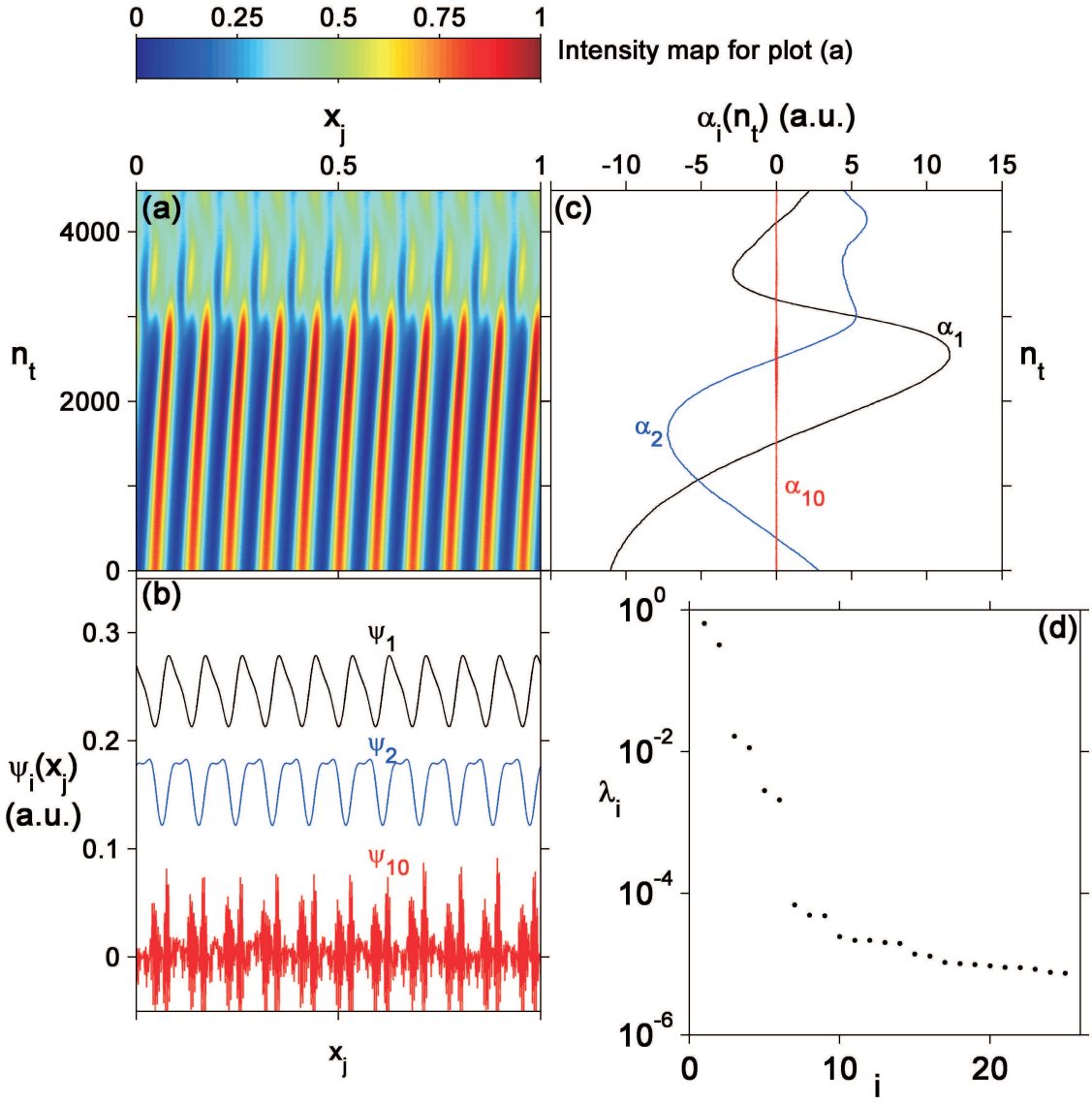

Figure 4.9: KL decomposition for laser 1 with a 0.050 μs coupling delay. (a) Spatiotemporal representation of the intensity dynamics from Fig. 3.5(b). (b) KL modes associated with the largest two eigenvalues and the tenth largest eigenvalue. Modes 1 and 2 are offset for clarity. (c) Expansion coefficients for the KL modes in (b). The vertical axis is time as represented by n_t. (d) Logarithmic plot of the 25 largest eigenvalues normalized by the sum of all the eigenvalues.

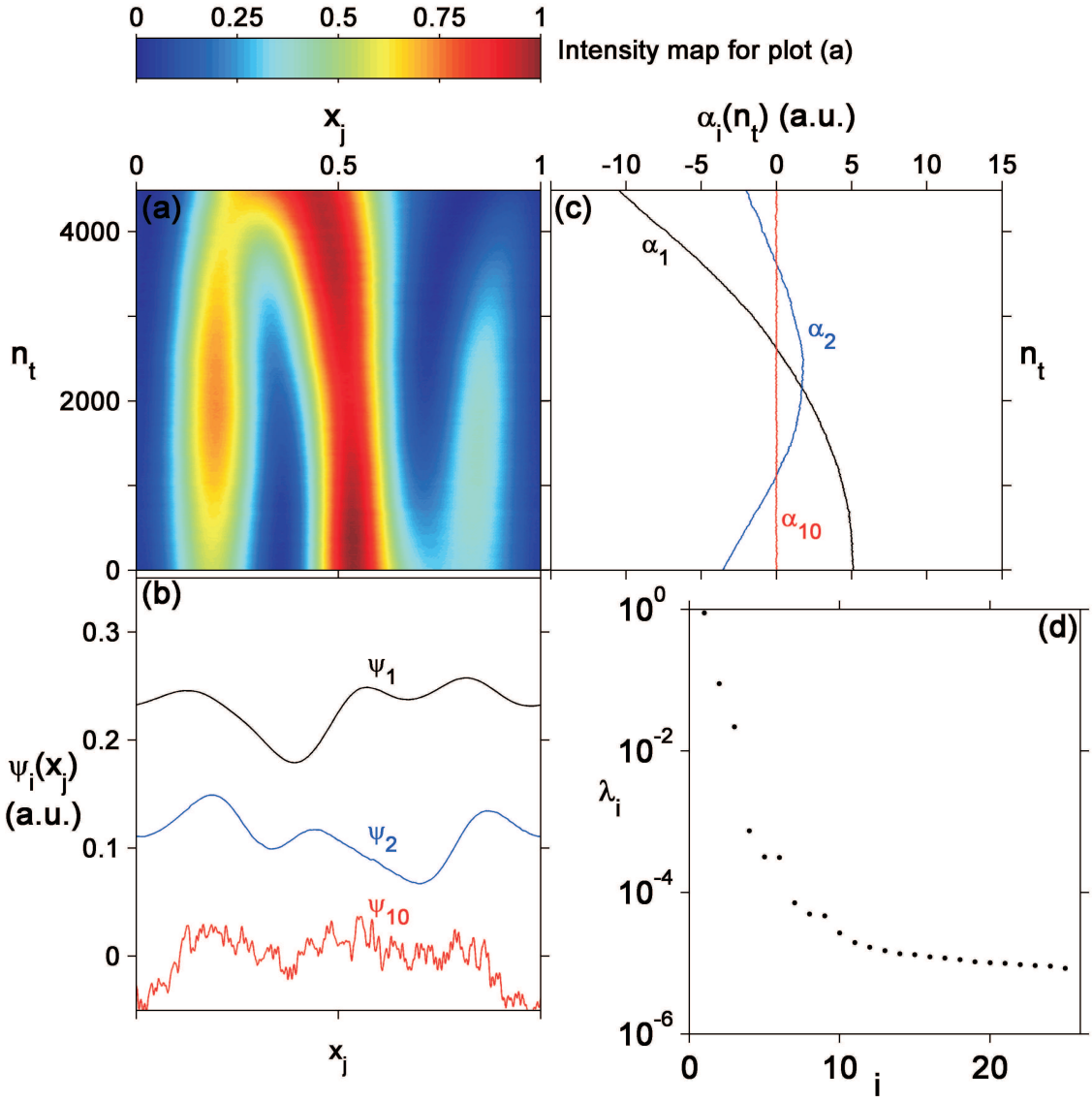

Figure 4.10: KL decomposition for laser 1 with a 0.218 μs coupling delay. (a) Spatiotemporal representation of the intensity dynamics from Fig. 3.5(d). (b) KL modes associated with the largest two eigenvalues and the tenth largest eigenvalue. Modes 1 and 2 are offset for clarity. (c) Expansion coefficients for the KL modes in (b). The vertical axis is time as represented by n_t. (d) Logarithmic plot of the 25 largest eigenvalues normalized by the sum of all the eigenvalues.

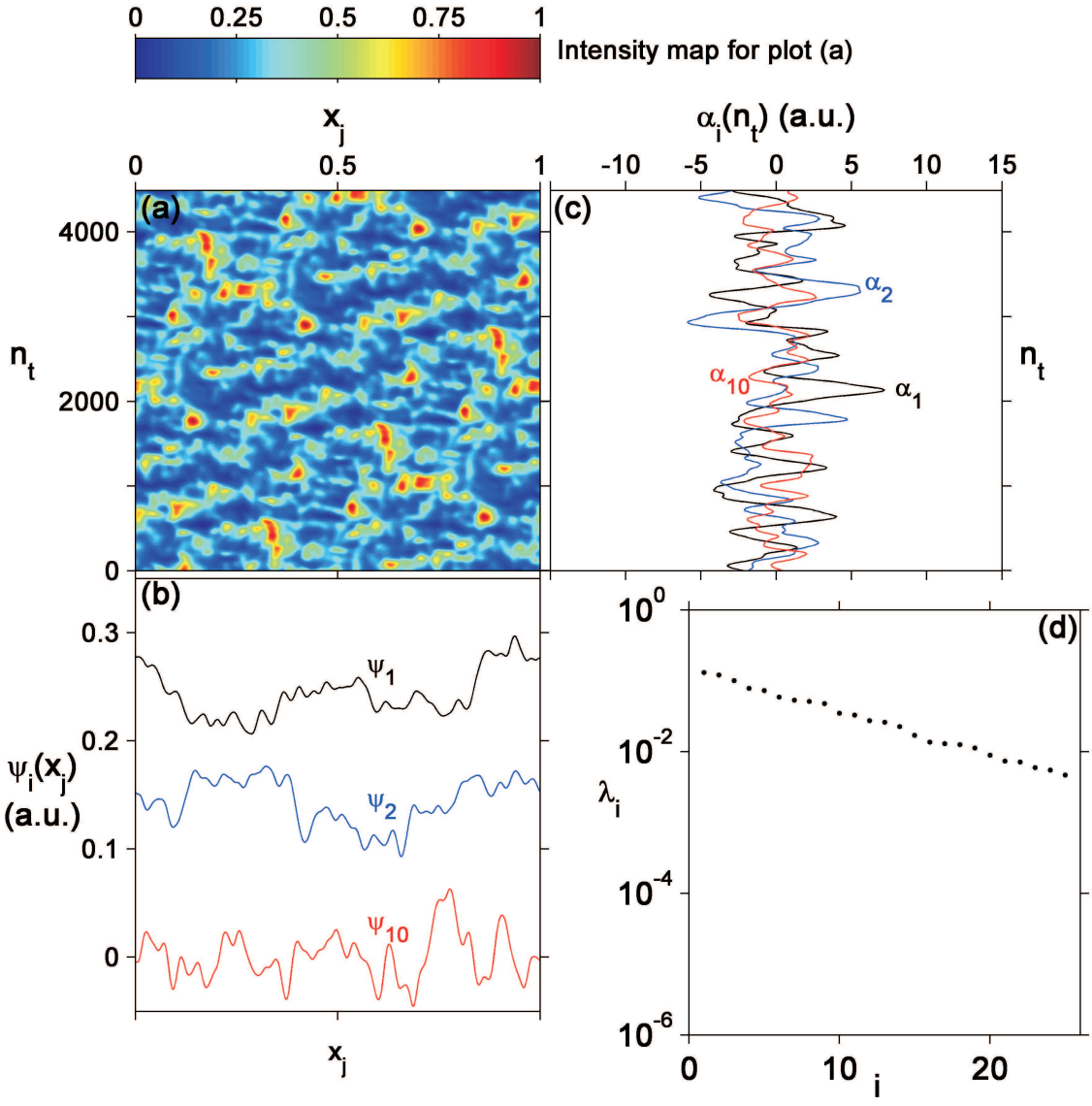

Figure 4.11: KL decomposition for laser 1 with a 120 μs coupling delay. (a) Spatiotemporal representation of the intensity dynamics from Fig. 3.5(h). (b) KL modes associated with the largest two eigenvalues and the tenth largest eigenvalue. Modes 1 and 2 are offset for clarity. (c) Expansion coefficients for the KL modes in (b). The vertical axis is time as represented by n_t. (d) Logarithmic plot of the 25 largest eigenvalues normalized by the sum of all the eigenvalues.

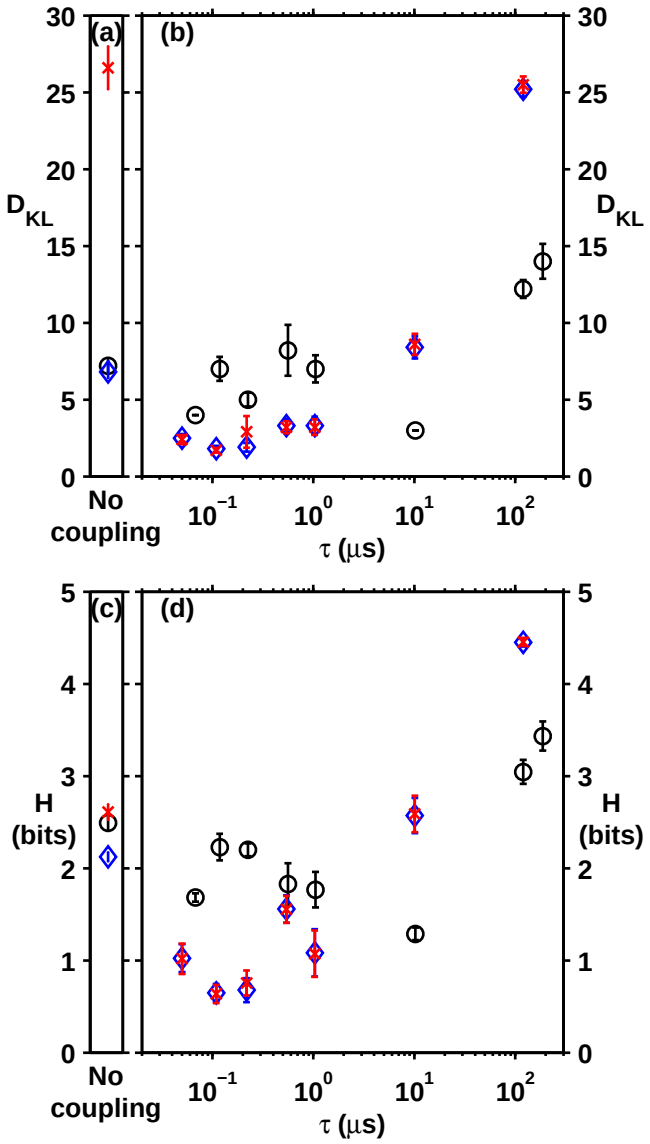

Figure 4.12: (a) Number of KL modes needed to reconstruct the spatiotemporal plot to 95% accuracy for a laser without feedback (○) and laser 1 (blue ◇) and laser 2 (red ×) when uncoupled. (b) Number of KL modes needed for 95% accurate reconstruction of the spatiotemporal plot for single laser with feedback (○) and laser 1 (blue ◇) coupled to laser 2 (red ×) with different delays. (c) Entropy for a laser without feedback (○) and laser 1 (blue ◇) and laser 2 (red ×) when uncoupled. (d) Entropy for single laser with feedback (○) and laser 1 (blue ◇) coupled to laser 2 (red ×) with different delays. The error bars in all plots are the statistical standard error based on a sample set of ten for the coupled lasers and five for the single laser. The single laser data (black circles) are reprinted from Fig. 3.12 for comparison. The coupled laser data in(c) and (d) is from Ref. [80].

uncoupled case. Counting the KL eigenvalues rates the complexity of laser 2 higher than the longest delay case and much higher than laser 1 uncoupled. The entropy of the two uncoupled lasers is similar which is expected since the spatiotemporal representations are similar. The reason for the discrepancy is revealed by examining the eigenvalue spectra of two typical cases. Figure 4.13 shows the 25 largest eigenvalues and the cumulative sum of the eigenvalues for the KL decomposition of the spatiotemporal representations shown in Fig. 4.6(a). S for laser 1 reaches the 95% cut off before the decay rate of the eigenvalues flattens. For laser 2 the knee is rounded before S crosses the cut off and it takes many more eigenvalues to reach it. Thus the arbitrary cut off has a significant impact on the final value of D_{KL}. H provides a better measure of complexity for our lasers because we do not need to set a cut-off arbitrarily and it gives similar values for similar spatiotemporal representations and eigenvalue spectra (compare Fig 4.6(a) and Fig. 4.13 with Fig. 4.11(a) and (d)).

4.7 Optical spectra

The optical spectra of the lasers is presented in Fig. 4.14. Each peak is a spectral envelope of the wavelengths measured over the scan time of the OSA. The figure shows that the lasing wavelengths can shift when the lasers are coupled. The spectra are not stable in that the peaks shift in location and shape from scan to scan of the OSA. For Fig. 4.14(c) and (g)-(i) the spectra is confined to a single peak which we can compare the uncoupled laser spectra. The height of the peaks increases

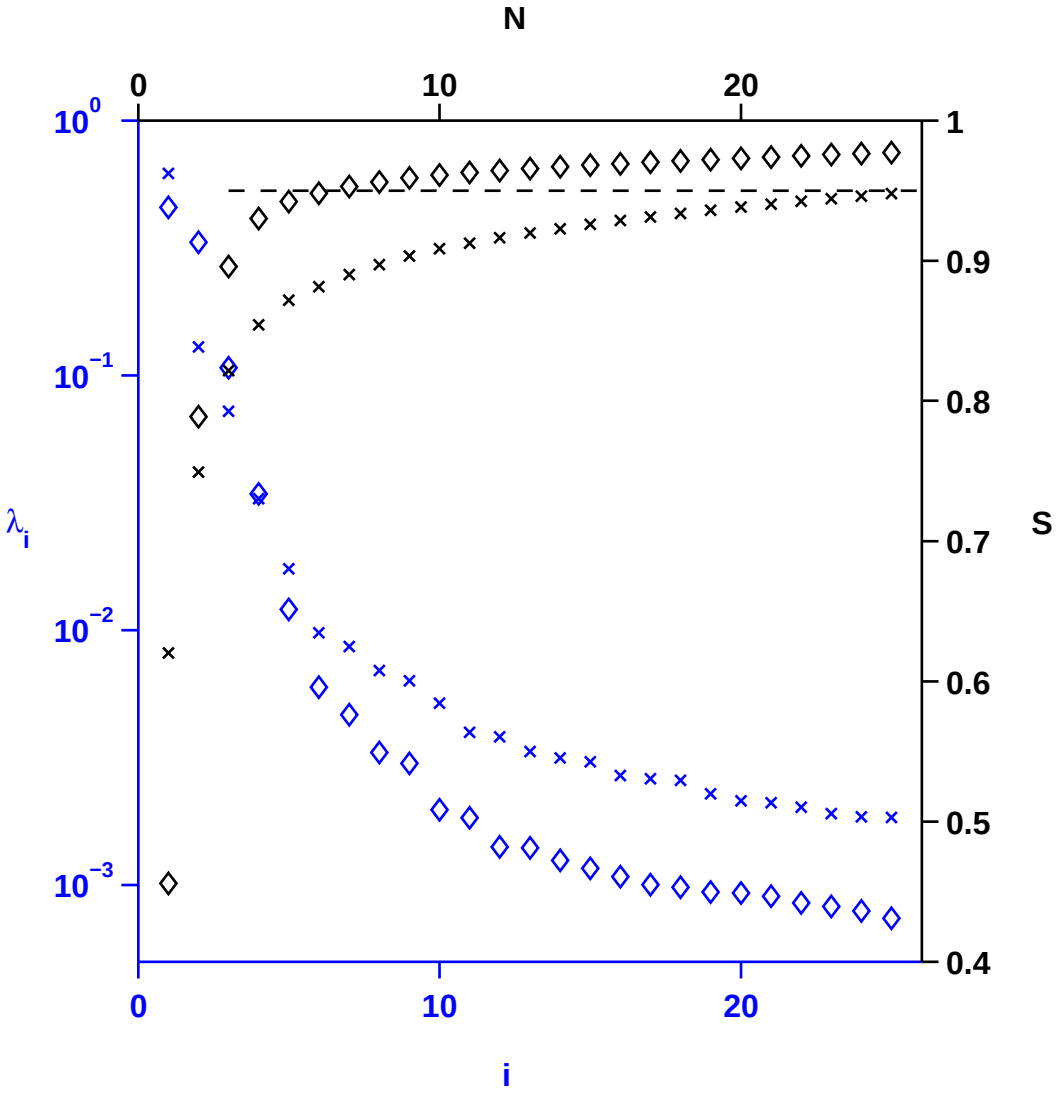

Figure 4.13: KL eigenvalue spectra and cumulative sum of the eigenvalues for laser 1 ($\diamond$) and laser 2 ($\times$) uncoupled. The first 25 normalized eigenvalues are plotted on the left axis in blue and the cumulative sum of the eigenvalues is plotted in black on the right axis. The dotted line shows the the cut off $S = 0.95$.

by four times or more. This indicates an increase in the coherence of the optical fields. The increase is partially due to the reduction in width of the spectral peak which pulls more power into the central wavelengths, thus raising the peak intensity. When the lasers are coupled the full width at half maximum decreases from 0.2 nm to 0.1 nm. This could be due to the restriction imposed on the conditions required for lasing in the two cavities. Each cavity is tuned to operate at a certain wavelength by adjusting the polarization controllers in the cavity. Since the fiber is birefringent the light must have certain polarization states to experience high gain. When coupled to the other laser, only modes with polarization states that satisfy both laser cavities will be amplified. This limits the range of wavelengths over which the light will experience gain and hence limits the range of lasing wavelengths.

4.8 Discussion and comparison with the single laser with feedback

The effect of a low level of time-delayed injected light on an EDFRL with an extra feedback loop or from mutual coupling to another EDFRL depends on the time delay. One effect observed in both experiments and shown in Fig. 4.3 was the increase in the size of the fluctuations about the mean with increasing τ. For the single laser case the fluctuation size did not increase significantly until τ exceeded 10 μs. For the mutually coupled lasers the fluctuation size was significantly larger at short τ than the single laser case. For longer delays the fluctuation size increased and became comparable to the single laser case at the longest delays considered. There was a significant spike at the resonant delay condition ($\tau = \tau_r$).

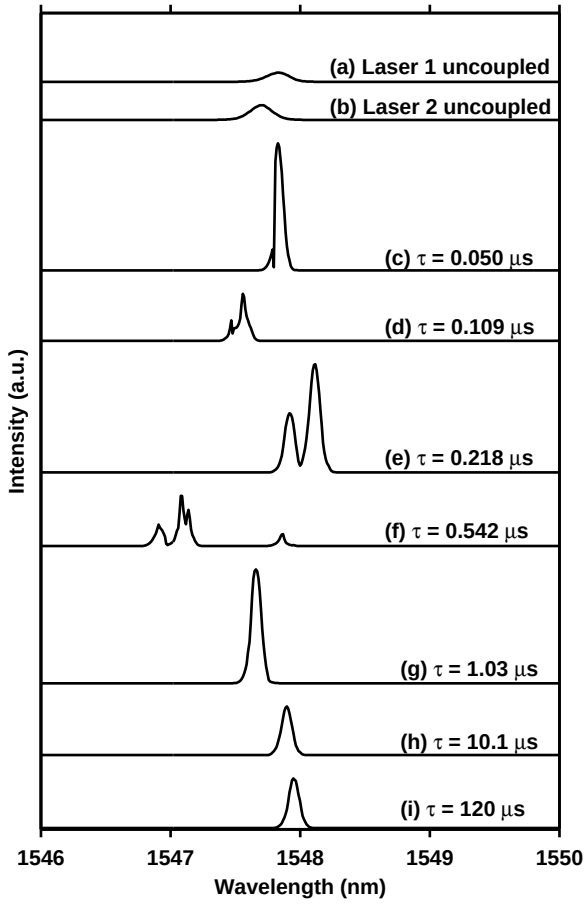

Figure 4.14: Optical spectra of the lasers. (a) and (b) are for the uncoupled lasers. (c)-(h) are the sum of the light from both lasers coupled with a delay, τ, as listed.

These observations may have to do with the coherence time of the lasers. From the measured spectra of the fiber lasers in Figs. 3.13 and 4.14 we see that a typical spectral width of the uncoupled lasers is about 0.2 nm, or $\Delta_f = 17$ GHz. This width is sufficient to accommodate approximately 4000 longitudinal modes of the laser which have a spacing of 4.45 MHz (51.5 fm). If these modes were randomly phased with respect to each other, the coherence time of the light would be estimated as $\tau_c \approx 1/\Delta_f = 58$ ps. Adding a second feedback loop with variable delay time to the single laser and measuring the standard deviation of the resulting intensity fluctuations (Fig. 3.3) shows that a marked increase occurs for a delay time of $\tau = 10$ μs. This result is corroborated when the two fiber lasers are mutually coupled as well (Fig. 4.3). The time scale of microseconds is much longer than the estimate of τ_c above. It indicates that the effective coherence time of the fiber laser output is not determined by the measured spectral width. Instead, it is comparable to the line width of a single longitudinal mode. Based on estimated cavity parameters our mode width is approximately 500 kHz which corresponds to $\tau = 2$ μs [75]. We do not see an increase in the fluctuation size for the single laser with feedback for short delays because the injected light is from the same source, but at long delays the coherence time is exceeded and the fluctuations increase. The mutually coupled lasers see an increase in fluctuation size at all delays because the injected light is from a different source. More work needs to be done to determine the physical cause of the increased fluctuation size and also to examine the apparent resonance that occurs when $\tau = \tau_r$.

The complexity of the dynamics also changed with different delays. For a single

laser with a feedback delay comparable to τ_r, the EDFRL has periodic dynamics with periods shorter than τ_r. For τ much longer than τ_r, the dynamics repeat with periods of τ and τ_r, and the intracavity dynamics become more complex. Compared to the laser without feedback, the overall complexity as described by D_{KL} in Fig. 3.12(b) does not change for small τ, decreases for $\tau = 10$ μs, and then increases for large τ. The overall complexity as described by H in Fig. 3.12(d) decreases for small τ, is minimized at $\tau = 10$ μs, and then increases for large τ.

This behavior highlights one of the characteristics of the KL decomposition method as applied to our data. Figures 3.4(g) and 3.5(g) shows that the round trip patterns for this $\tau = 10$ μs case are complex, yet both D_{KL} and H rated the overall complexity of the dynamics as very low. This is because even though only a few KL modes are needed to reproduce the data there are no constraints on how complicated an individual KL mode can be. Figure 3.9(b) shows that the KL modes are complex in this case, while Fig. 3.9(c) shows that the expansion coefficients for the first two modes are large. Thus the complexity measures we use from the KL decomposition describe the overall spatiotemporal complexity of the data and do not quantify how complex the individual KL modes might be. Since the KL modes have a "length" of τ_r these measures do not quantify the complexity within a round trip. Since the KL modes can be thought of as round-trip-long strips of time series, time delay embeddings of the KL modes could be done to examine their complexity in the future.

The complexity of the dynamics of two mutually coupled EDFRLs are similar to the single EDFRL with feedback. Compared to the single laser the dynamics are

less complex for short τ and more complex for long τ as seen in Fig. 4.12. For long τ the round trip patterns repeat, but now the long time scale repetition is 2τ instead of τ. The EDFRLs also synchronize with each other. Usually the synchronization occurs with a time shift that depends on the fast periodicity of the dynamics, but in two cases it appears to occur with no shift. As the dynamics become more complex for long delays, the lasers synchronize with a shift corresponding to $\pm\tau$ in agreement with previous results for chaotic data.

The spectrum of the coupled lasers collapses to roughly half of the width of the uncoupled lasers' spectra. This collapse of available modes does not occur in the single EDFRL with a feedback loop. As described above, in the mutually coupled case there are two laser cavities that define two independent sets of constraints on the light. Only cavity modes that satisfy the two sets of constraints will experience gain and survive. This reduction in available modes is correlated to a reduction in the complexity of the dynamics. The ability to simplify the complex dynamics of an oscillator by applying small amounts of feedback with short delays or coupling oscillators together with short delays can help organize unwanted complex behavior.

A way to interpret this much longer coherence time is to observe that the spatiotemporal patterns in Figs. 3.5 and 4.6 are stable over hundreds of round trips of the fiber laser cavities. This demonstrates that the phases of the individual longitudinal modes are stable relative to each other for long periods of time of the order of microseconds. If the lasers were completely mode locked one would notice a recurring ultrashort pulse on every round trip. Instead the temporal patterns in Figs. 3.2 and 4.2 show complex patterns of peaks and valleys which indicate

that not all the modes are locked. These metastable repeating complex patterns could be interpreted as being due to clusters of longitudinal modes that remain in a stable phase relationship over hundreds of round trips. Figure 4.6 in particular thus demonstrates stable phase locking of the mutually coupled lasers, giving rise to highly regular spatiotemporal patterns.

4.9 Summary of Chapter 4

Mutually coupling two lasers together with a delay causes an increase in the intensity fluctuation size at all delays investigated. The largest fluctuations occur at the longest delay and when $\tau = \tau_r$. We also see lag-synchronization of the two lasers with a delay that does not equal the coupling delay when the dynamics are periodic.

KL decomposition shows us that the dynamics get simpler for short delays and more complex for long delays. The Shannon entropy, H, appears to be a more robust measure of complexity then the number of eigenvalues, D_{KL}, needed to achieve an arbitrary data reconstruction accuracy. The method using D_{KL} is very sensitive to the location of the knee in the eigenvalue spectrum. The calculation of H considers all of the eigenvalues while the method that uses D_{KL} ignores the smaller ones completely once the cut-off has been reached.

Chapter 5

Driven mutually coupled lasers

5.1 Overview

The previous chapter showed lag synchronization occurred for mutually coupled systems which is consistent with previous experimental and theoretical results for fiber lasers [26, 27, 74]. Other work has shown isochronal synchrony between two semiconductor lasers when a third laser was mutually coupled between them [82]. Recent modeling with Ikeda ring oscillators shows stable isochronal synchrony can be achieved in mutually coupled oscillators by unidirectionally driving them with a third oscillator [34]. In this chapter we will experimentally investigate the transition from lag to isochronal synchrony for mutually coupled EDFRLs.

We add a third laser to the mutually coupled configuration studied in the previous chapter. This laser, referred to as the drive laser, is unidirectionally coupled to laser 1 and 2. The effect of the drive laser on the dynamics of the first two lasers is examined. Data was taken for the case when laser 1 and 2 are mutually coupled with a short delay, and also when the two lasers are uncoupled. This chapter will describe the experimental setup and then examine the cross correlations between the three lasers to determine the synchronization state between the lasers. The driven uncoupled lasers case will be examined and then the driven mutually coupled case will be described afterwards.

5.2 Experimental set-up

The previous experiment was modified as shown in Fig. 5.1. Another 70/30 coupler was added to lasers 1 and 2 to insert light from the drive laser. These couplers were inserted after the output couplers that are used to mutually couple the lasers. This adds fiber to the ring cavity so the round trip times were re-measured using the Fourier transform method described in section 4 of Ch. 2. Ten 1 ms time series were taken for each laser. The new round trip times are 224.88 ± 0.03 ns for laser 1 and 224.83 ± 0.02 ns for laser 2 which corresponds to a length of around 46.7 m. The errors are standard errors based on a sample size of ten. The pump levels of the lasers were changed from $4I_{th}$ down to $1.2I_{th}$. The lower pump values result in lower power levels in the response lasers' cavities. This effectively raises the maximum coupling strength from the drive laser which operates at a constant high power.

The drive laser is unidirectionally coupled to lasers 1 and 2. It uses a Uniphase model OAB 1552 erbium-doped fiber optical amplifier. This amplifier is not specifically matched to the Oprel EDFAs in lasers 1 and 2 because it was manufactured separately so characteristics such as the length of active erbium-doped fiber are different. We used a pump setting of $I_p = 114.8$ mA which is 4.4 times the threshold of $I_{th} = 26.1$ mA. A polarization controller is used to tune the laser's wavelength. A 95/5 coupler is used to send light to a New Focus model 1811 IR 125 MHz bandwidth photodetector and the LeCroy LC534AM oscilloscope which is used to measure the intensity dynamics of the laser. We used the method described in section 4 of Ch. 2

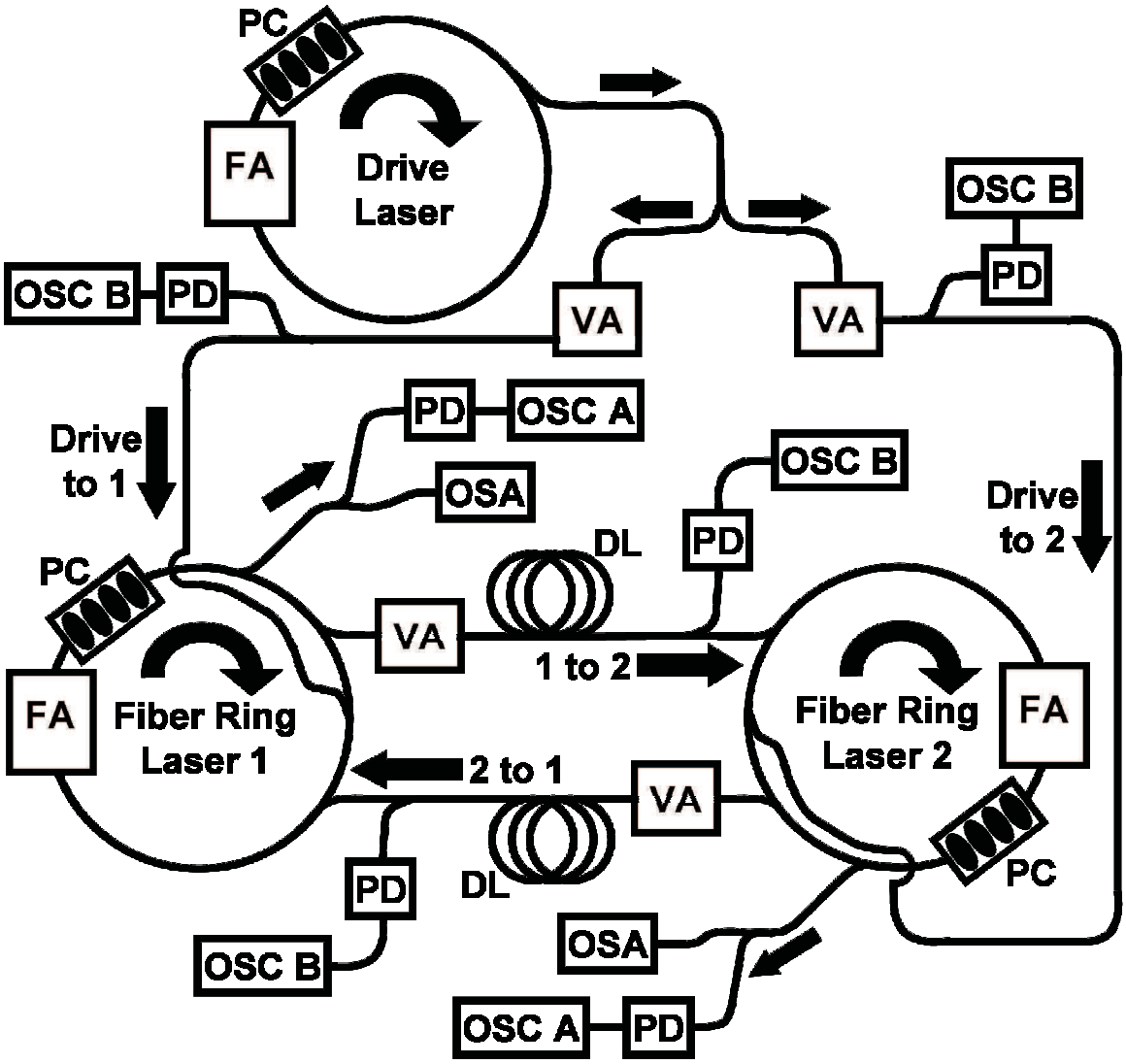

Figure 5.1: Experimental setup for two mutually coupled lasers driven by a third laser. The arrows show the direction of light propagation through the rings and the coupling lines. FA, erbium-doped fiber amplifier; PC, polarization controller; VA, variable attenuator; DL, delay line; PD, photodetector; OSC A, oscilloscope used to measure laser dynamics; OSC B, oscilloscope used to monitor the coupling lines; OSA, optical spectrum analyzer.

to measure the round trip time and found $\tau_r = 225.37 \pm 0.03$ ns. The error is a standard error based on a sample size of ten. A 70/30 coupler pulls light out of the ring and then a 50/50 coupler splits the light to send to lasers 1 and 2. For clarity, the lines carrying signals unidirectionally transmitted from the drive laser to lasers 1 and 2 will be referred to as "transmission lines." The lines that mutually couple laser 1 and laser 2 will be called "coupling lines." Variable attenuators in the transmission lines are used to change the coupling strength of the drive laser to the response lasers, κ_D. Also, the variable attenuators ensure κ_D is the same for both transmission lines. 90/10 couplers pull light out of the transmission lines to monitor it with a Tektronix model TDS 3032 oscilloscope (OSC B) which reads the DC level of a New Focus model 1611 IR photodetector. The travel time down the two unidirectional transmission lines is 43.3 ns for the drive to laser 1 and 43.1 ns for the drive to laser 2.

The sampling time for the intensity time series is increased to 2 ns per point because the sampling time of the LeCroy LC534AM oscilloscope is cut in half when three or four channels are used. The time series are still 1 ms long, but have half as many data points. The measurement lines from the output couplers of the lasers to the oscilloscope are matched to within 0.5 ns of each other. Data was taken when lasers 1 and 2 were uncoupled to provide a baseline of their behavior when driven. Data was also taken with lasers 1 and 2 mutually coupled to each other while being driven to see if isochronal synchrony could be achieved. The driven uncoupled lasers are discussed next.

5.3 Driven uncoupled lasers

For these measurements the light in the coupling lines were blocked to break the mutual coupling. The cross correlation between two time series, given by $CC_{x,y}(s)$ in Eq. 4.1, is used to determine the level of synchrony between two time series of laser x and laser y with a shift, s, between the two time series. A typical set of cross correlations is shown in Fig. 5.2 for the response lasers pumper at $1.4I_{th}$. Figure 5.2(a) shows the correlations for the lasers when uncoupled. The correlation is close to zero as expected because the lasers do not adjust to each other when uncoupled. Figures 5.2(b) and (c) show the cross correlations for a small and large amount of drive coupling respectively. The thick blue bars indicate the 258 ns lag from the time the oscilloscope reads the drive laser data to the time the oscilloscope reads the corresponding signal from the response lasers. This lag is due to the drive signal traveling down the transmission line and then most of the way around the response lasers' cavities before reaching the output couplers that send the light to the oscilloscope. If the response lasers synchronize with the drive then we expect to see a peak in $CC_{1,D}$ (the blue curves) and $CC_{2,D}$ (the red curves) at the end of the blue bars. Isochronal synchrony between the response lasers would be indicated by a peak in the black curves at $s = 0$. The plots that follow show values of $CC_{x,D}(s)$ for $s = 256$ or 258 ns. Values at both points were checked and the s that gave the largest cross correlations consistently was used. The plots also show values of $CC_{1,2}(s = 0)$ to check for isochronal synchrony. The repeating patterns in the cross correlations are due to the round trip repetition in the laser dynamics.

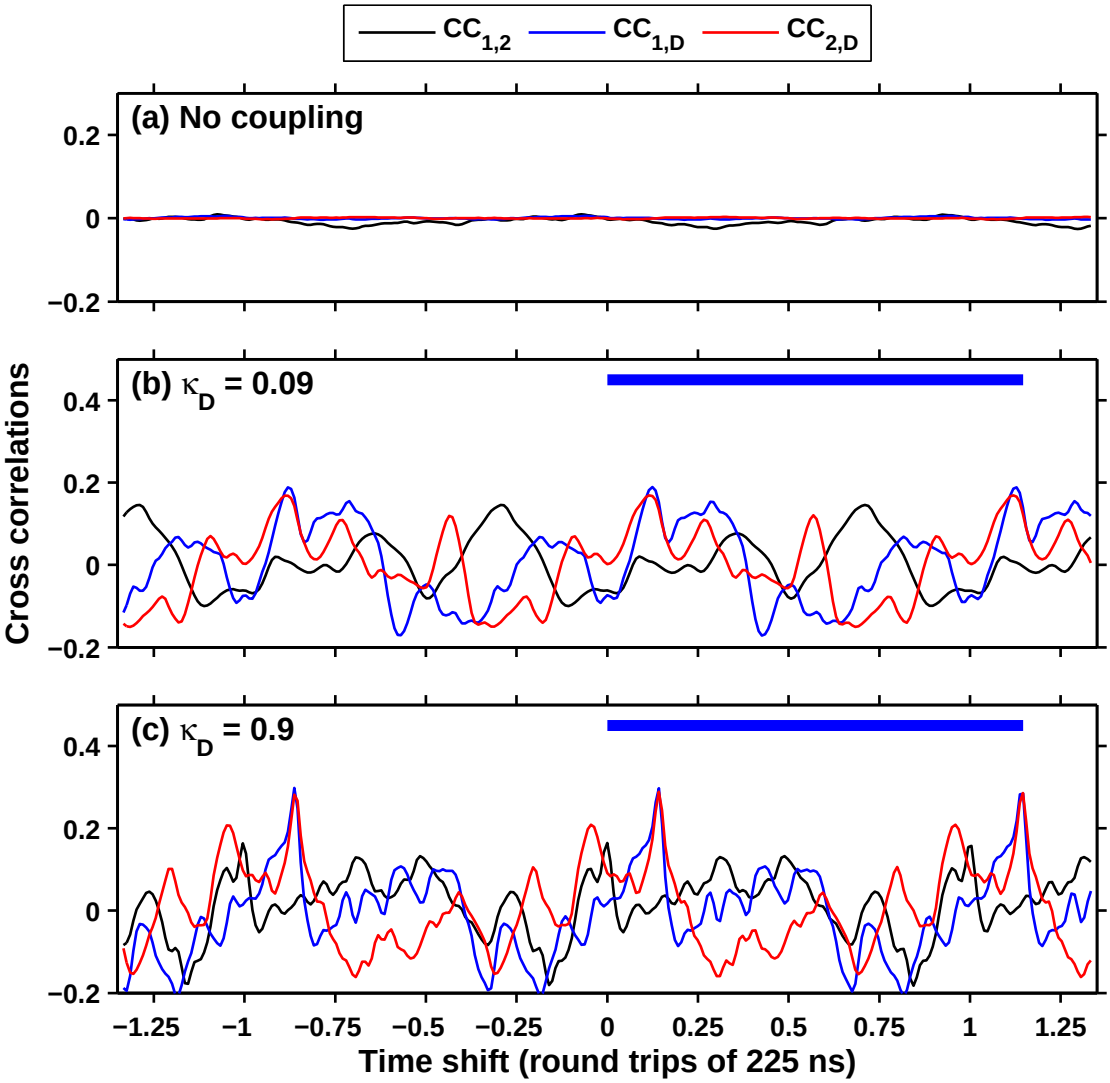

Figure 5.2: Cross correlations for unidirectional driving of uncoupled response lasers pumped at $1.4I_{th}$. (a) No coupling between any of the lasers. (b) Low level of drive coupling. (c) High level of drive coupling. For all plots of $CC_{x,y}$ the left(right) side of the plots correspond to a shift as if $x(y)$ were leading. The blue bars in plots (b) and (c) indicate the 258 ns time lag for a signal to travel from the drive through the transmission line and the response laser and be measured as compared to a signal measured directly from the drive.

The cross correlations for lasers 1 and 2 pumped at four times threshold is shown in Fig. 5.3. Plot (a) shows $CC_{x,D}\,(s = 256$ ns) with the drive laser leading the response lasers. The response lasers do not synchronize to the drive. Figure 5.3(b) shows $CC_{1,2}\,(s = 0)$. If isochronal synchrony of the response lasers occurs then $CC_{1,2}\,(s = 0) = 1$. Since the response lasers do not synchronize to the drive we don't expect them to synchronize to each other without mutual coupling.

Synchrony may occur at larger coupling strengths, but the drive laser is operating at its peak power level. We can effectively increase κ_D by decreasing the power in the response lasers' cavities by turning down the pump. Figure 5.4 shows the results for the response lasers pumped at $2I_{th}$. The cross correlations increase and saturate at low values. Reducing the pump further to $1.4I_{th}$ and $1.2I_{th}$ produces similar levels of synchronization as shown in Fig. 5.5 and Fig. 5.6 respectively.

Figures 5.4, 5.5, and 5.6 show that the cross correlations between the drive and the response lasers saturate at about 0.3 for larger κ_D. This is consistent with previous work that considered noise-induced synchronization of two uncoupled response systems [83]. That work drove two uncoupled lasers with a noise modulated signal from a single mode external cavity semiconductor laser and found a quick transition from no synchrony to synchrony that saturated at 0.4. Our experiment is similar except we use a drive laser with thousands of modes which is modulated by spontaneous emission noise and our transition is more gradual.

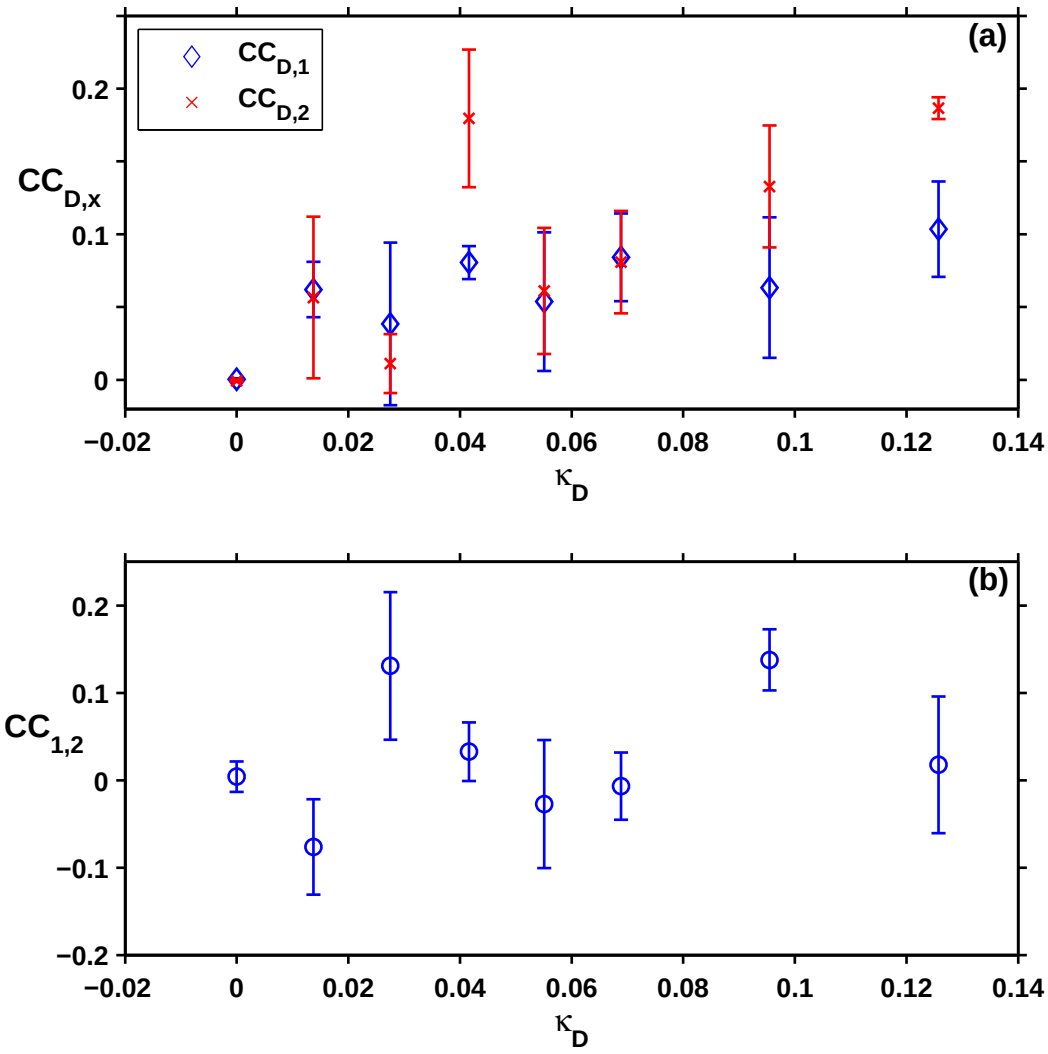

Figure 5.3: Cross correlations at specific shifts for unidirectional driving of uncoupled response lasers pumped at $4I_{th}$. (a) Cross correlations between the drive and laser 1 (blue $\diamond$) and the drive and laser 2 (red $\times$) where the drive leads by $s = 256$ ns. (b) Cross correlation of laser 1 and 2 with $s = 0$ ns. The κ_D values are averages of the values for the two transmission lines.

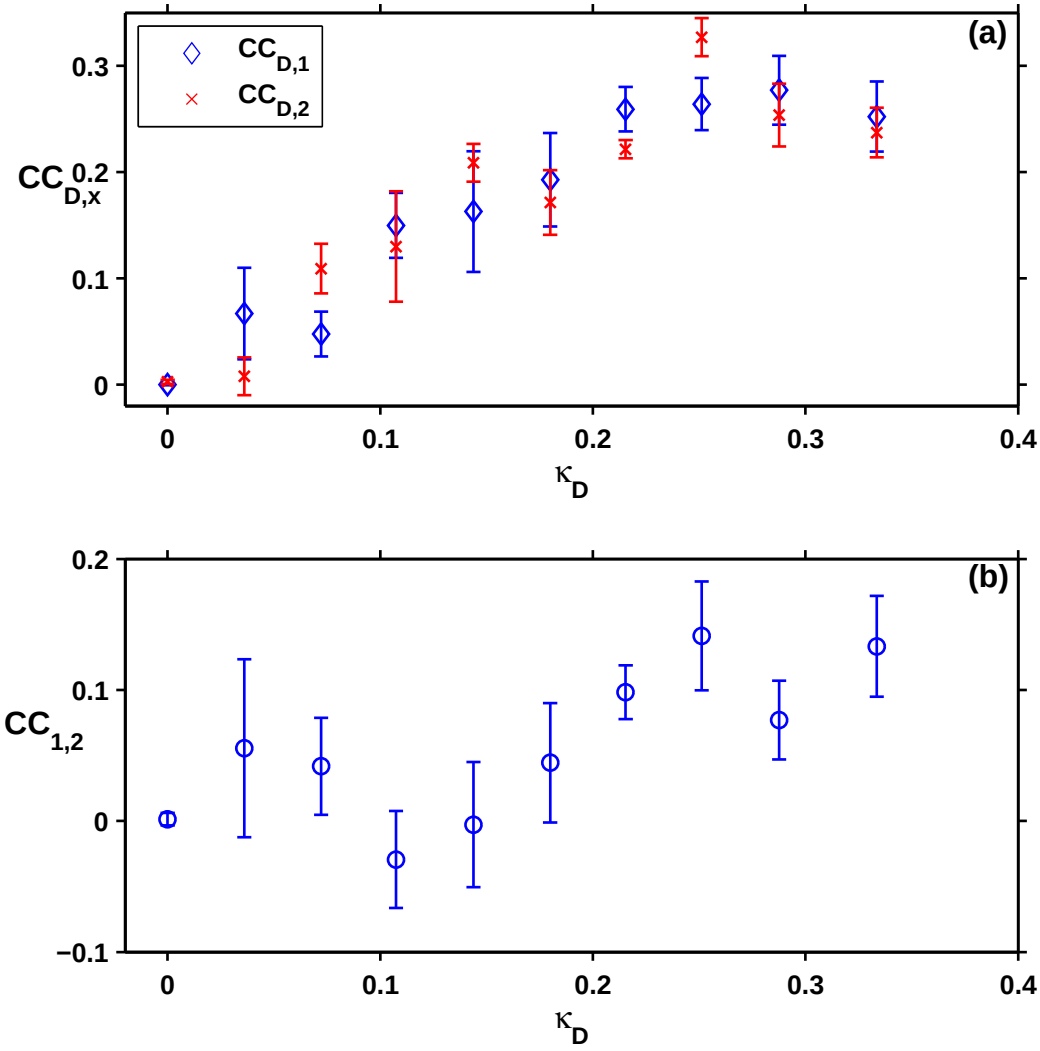

Figure 5.4: Cross correlations at specific shifts for unidirectional driving of uncoupled response lasers pumped at $2I_{th}$. (a) Cross correlations between the drive and laser 1 (blue $\diamond$) and the drive and laser 2 (red $\times$) where the drive leads by $s = 256$ ns. (b) Cross correlation of laser 1 and 2 with $s = 0$ ns. The κ_D values are averages of the values for the two transmission lines.

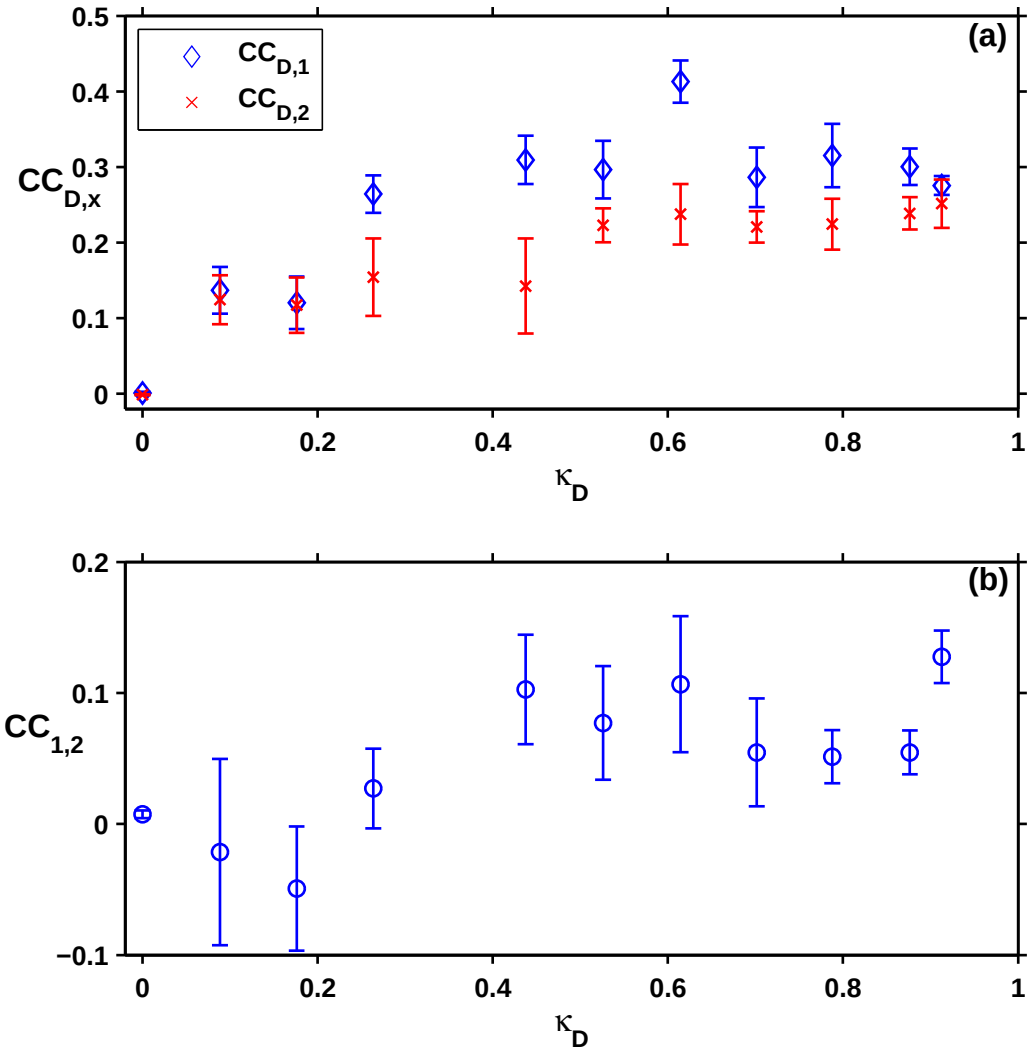

Figure 5.5: Cross correlations at specific shifts for unidirectional driving of uncoupled response lasers pumped at $1.4I_{th}$. (a) Cross correlations between the drive and laser 1 (blue $\diamond$) and the drive and laser 2 (red $\times$) where the drive leads by $s = 258$ ns. (b) Cross correlation of laser 1 and 2 with $s = 0$ ns. The κ_D values are averages of the values for the two transmission lines.

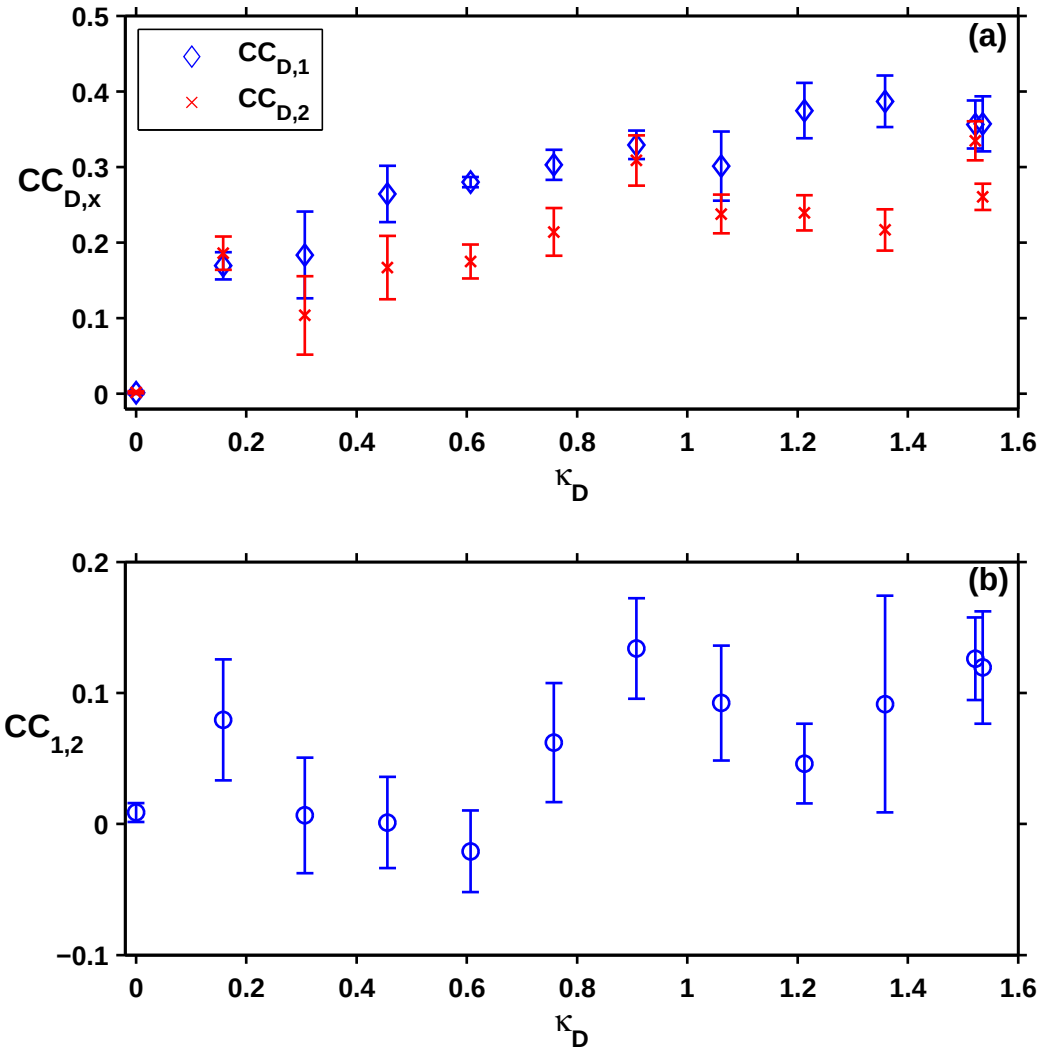

Figure 5.6: Cross correlations at specific shifts for unidirectional driving of uncoupled response lasers pumped at $1.2I_{th}$. (a) Cross correlations between the drive and laser 1 (blue $\diamond$) and the drive and laser 2 (red $\times$) where the drive leads by $s = 258$ ns. (b) Cross correlation of laser 1 and 2 with $s = 0$ ns. The κ_D values are averages of the values for the two transmission lines.

5.4 Driven mutually coupled lasers

We repeat the experiments described above with mutual coupling between the response lasers. The coupling strength for the mutual coupling, κ_{MC} is 2.5%. Figure 5.7 shows some cross correlations for the mutually coupled case. If the lasers are mutually coupled only, we saw in Ch. 4 that lag synchrony occurs at some delay time. The cross correlations between the response lasers had a peak at $s = \pm 28$ ns for all of the mutually coupled only runs. This is seen in Fig. 5.7(a) and the value of $CC_{1,2}(s = 28)$ will be used as a measure of the level of lag synchrony between the response lasers in what follows. The black bars in the three plots of Fig. 5.7 indicate where $CC_{1,2}(s)$ (the black curves) should peak if lag synchrony is present. The blue bars are the same as in the previous section and indicate where $CC_{1,D}(s)$ (the blue curves) and $CC_{2,D}(s)$ (the red curves) should peak if synchrony between the drive and response lasers occurs. In Fig. 5.7(b) we see that lag synchrony between the response lasers is still present for low drive coupling, but Fig. 5.7(c) shows that the lag synchrony is quenched for large drive coupling. There is also a small peak for $CC_{1,2}(s = 0)$, indicating a very low level of isochronal synchrony. Small peaks are also present for $CC_{1,D}(s = 258)$ and $CC_{2,D}(s = 258)$ indicating the response lasers are synchronizing to the drive at low levels. In the plots that follow we compare $CC_{x,D}(s)$ of both response lasers to the drive laser for $s = 256$ ns or $s = 258$ ns depending on which shift gives the largest cross correlation values. This data is used to determine if the response lasers are synchronizing to the drive. We also compare $CC_{1,2}(s = \pm 28)$ to $CC_{1,2}(s = 0)$ to determine if lag or isochronal

synchrony is stronger.

Figure 5.8 shows the results for the response lasers pumped at $2I_{th}$. There is a small increase in the cross correlations between the response lasers and the drive in plot (a). Figure 5.8(b) shows cross correlations between the response lasers with different shifts, s. When there is no drive ($\kappa_D = 0$) the lasers synchronize with a lag. The cross correlation is symmetric about $s = 0$ and we cannot tell which laser is leading. We examine the cross correlations of each laser leading the other with a shift of 28 ns when the drive is on to determine if the lasers are still lag synchronized. This data is plotted in the bottom plot with blue $\diamond$'s and red $\times$'s. Likewise, if isochronal synchrony occurs then we expect $CC_{1,2}(s = 0) = 1$. The cross correlation for the isochronal shift is plotted with black $\circ$'s. We see in Fig. 5.8 that isochronal synchrony grows but that the cross correlation is less than 0.25. We also see that the lag-synchrony is quenched as the drive coupling increases.

Figures 5.9 and 5.10 shown the cross correlations for the response lasers pumped at 1.4 and 1.2 times threshold respectively. In both cases the response lasers couple to the drive with modest cross correlations. Also, the lag-synchrony is quenched as κ_D increases. The isochronal cross correlations gets larger than the lag correlations, but never get very large.

5.5 Discussion and summary of Chapter 5

The isochronal cross correlations show that although the response lasers are reacting to the drive laser, the level of synchronization is low. One reason could be

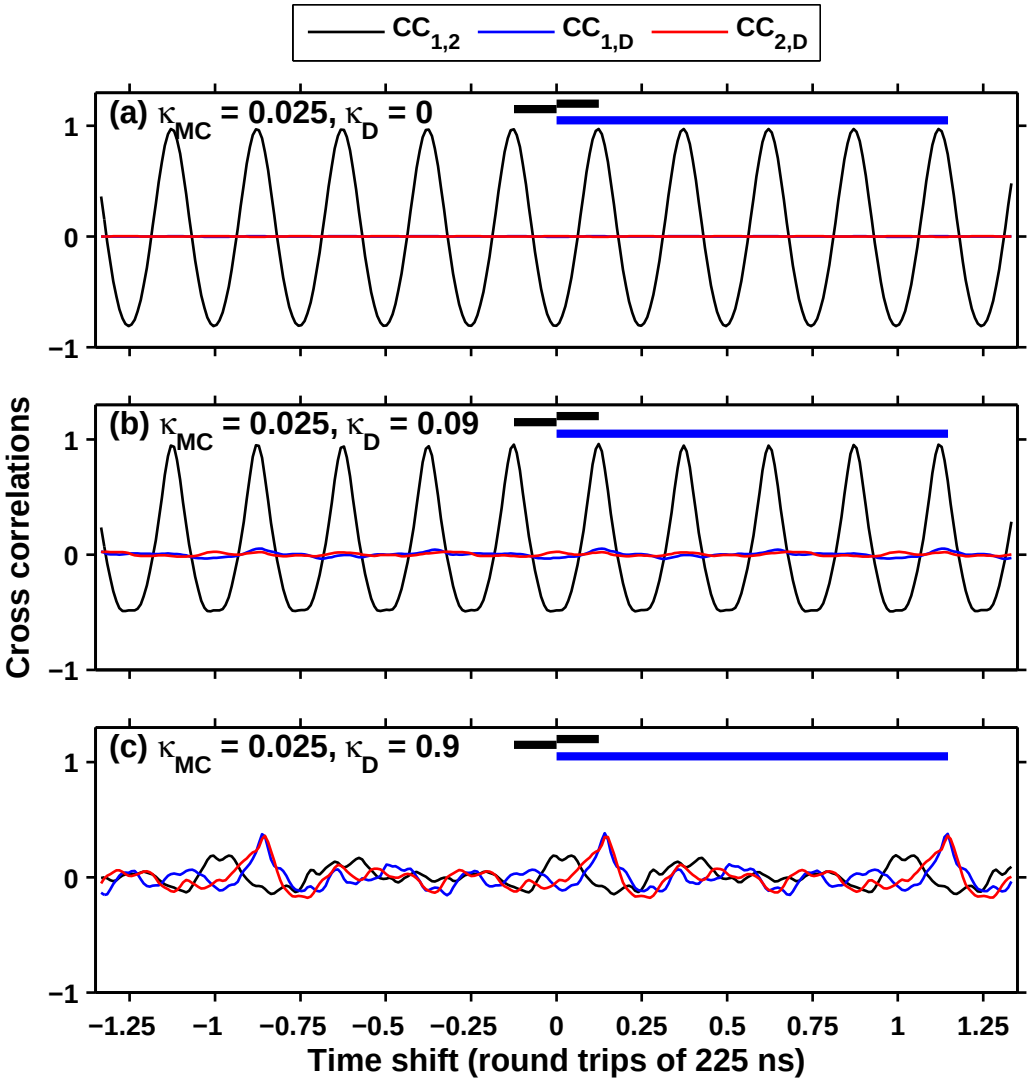

Figure 5.7: Cross correlations for unidirectional driving of mutually coupled response lasers pumped at $1.4I_{th}$. (a) Mutual coupling between the response lasers only. (b) Low level of drive coupling. (c) High level of drive coupling. For all plots of $CC_{x,y}$ the left(right) side of the plots correspond to a shift as if $x(y)$ were leading. The blue bars indicate the 258 ns time lag for a signal to travel from the drive through the transmission line and the response laser and be measured as compared to a signal measured directly from the drive. The black bars indicate a symmetric shift of ± 28 ns where $CC_{1,2}$ should peak if lag synchrony between the response lasers is present.

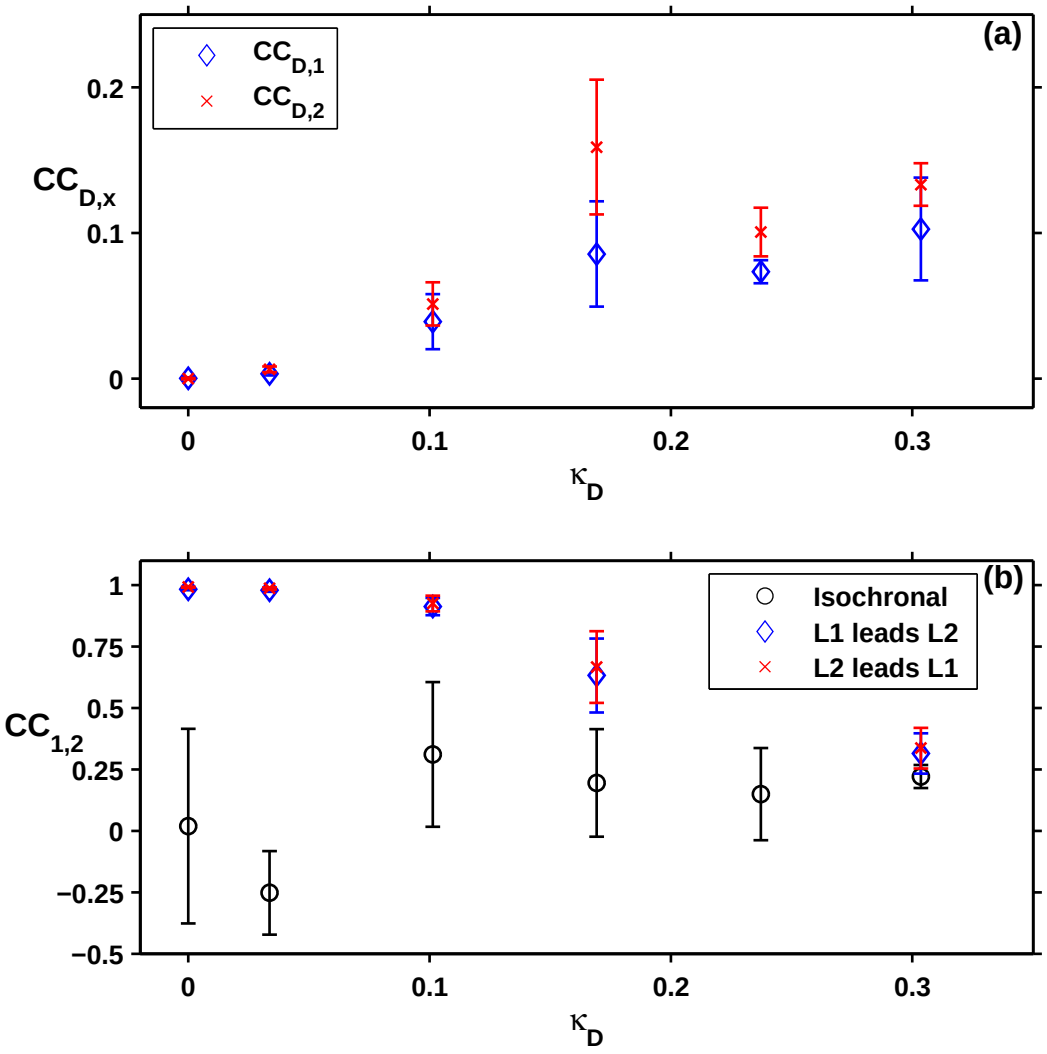

Figure 5.8: Cross correlations at specific shifts for unidirectional driving of mutually coupled response lasers pumped at $2I_{th}$. (a) Cross correlations at specific shifts between the drive and laser 1 (blue $\diamond$) and the drive and laser 2 (red $\times$) where the drive leads by $s = 256$ ns. (b) Cross correlations of laser 1 and 2 with no shift ($s = 0$ ns, $\circ$), shifted so laser 1 leads ($s = -28$ ns, blue $\diamond$), and shifted so laser 2 leads ($s = 28$ ns, red $\times$). The κ_D values are averages of the values for the two transmission lines.

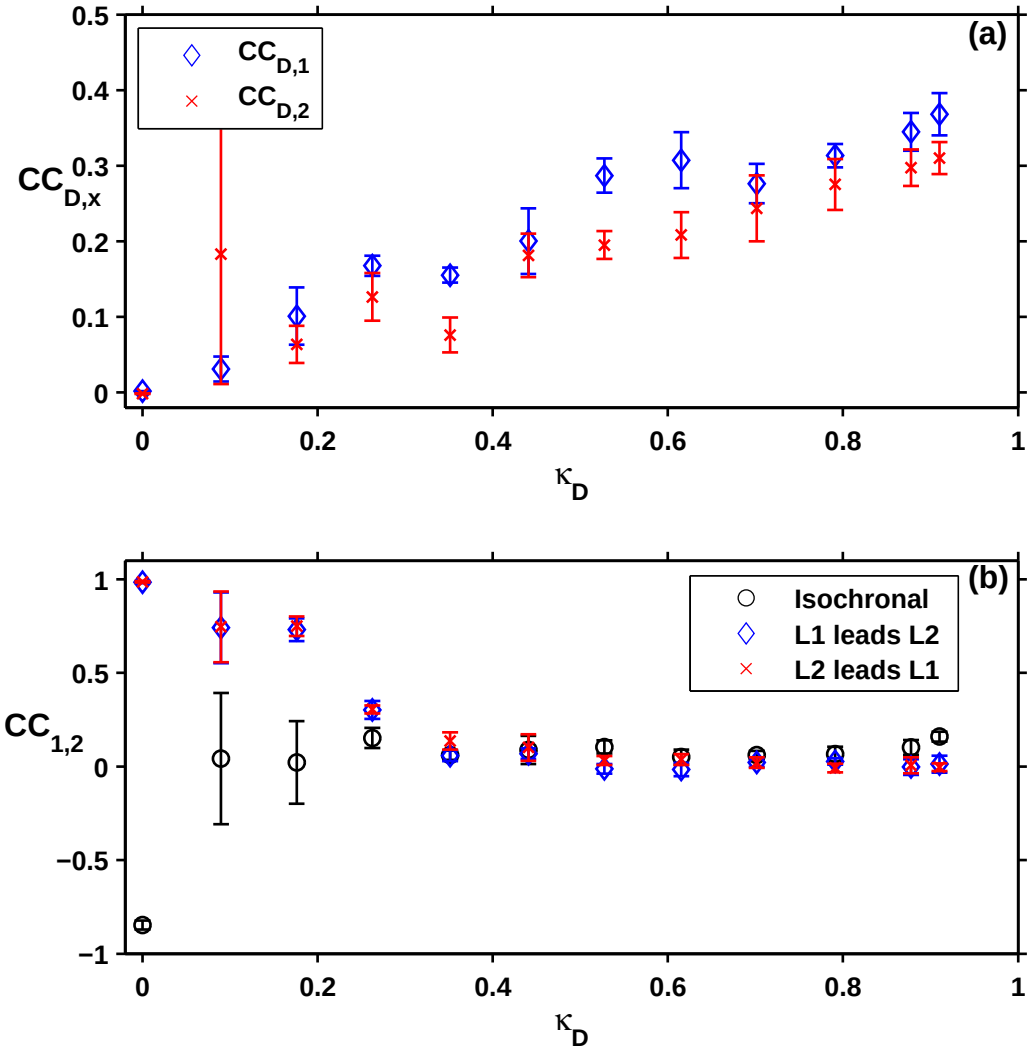

Figure 5.9: Cross correlations at specific shifts for unidirectional driving of mutually coupled response lasers pumped at $1.4I_{th}$. (a) Cross correlations at specific shifts between the drive and laser 1 (blue $\diamond$) and the drive and laser 2 (red $\times$) where the drive leads by $s = 258$ ns. (b) Cross correlations of laser 1 and 2 with no shift ($s = 0$ ns, $\circ$), shifted so laser 1 leads ($s = -28$ ns, blue $\diamond$), and shifted so laser 2 leads ($s = 28$ ns, red $\times$). The κ_D values are averages of the values for the two transmission lines.

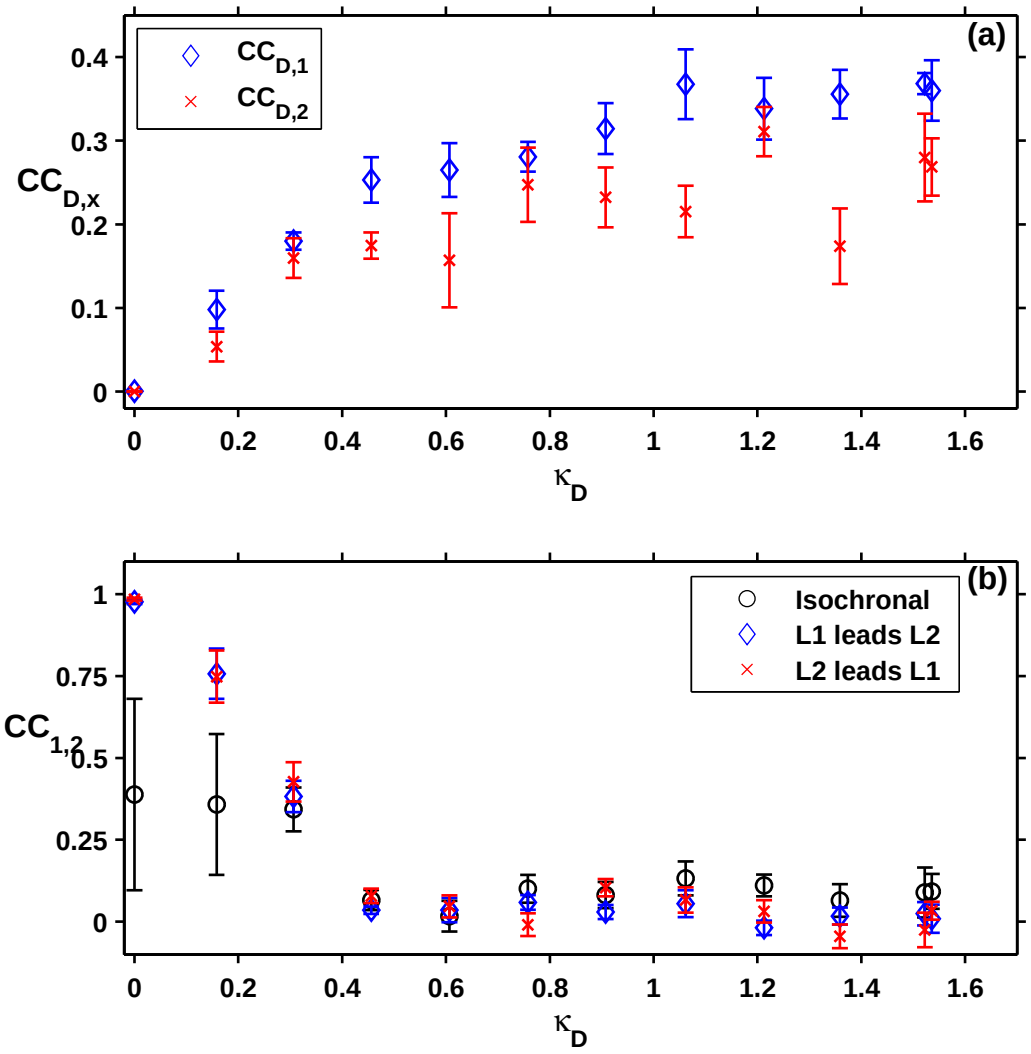

Figure 5.10: Cross correlations at specific shifts for unidirectional driving of mutually coupled response lasers pumped at $1.2I_{th}$. (a) Cross correlations at specific shifts between the drive and laser 1 (blue $\diamond$) and the drive and laser 2 (red $\times$) where the drive leads by $s = 256$ ns. (b) Cross correlations of laser 1 and 2 with no shift ($s = 0$ ns, $\circ$), shifted so laser 1 leads ($s = -28$ ns, blue $\diamond$), and shifted so laser 2 leads ($s = 28$ ns, red $\times$). The κ_D values are averages of the values for the two transmission lines.

the mismatch of the lasers' parameters. The drive laser's round trip time is 0.5 ns longer than the response lasers' round trip times. As we have seen in previous chapters, this is a very important parameter to the dynamics of the lasers. The drive laser cavity was shortened and the round trip time remeasured to find a new round trip time of 224.80 ± 4 ns. Also, losses in the response lasers' ring cavities were measured to more accurately match the drive coupling strengths. The coupling strengths are defined as the ratio of the power of the injected light to the power of the light in the cavity. The measurement of power in the ring is made at the input to the 95/5 output coupler and the power level needs to be reduced for each coupler in the cavity between this point and the injection point. Measurements showed that the couplers and connectors of the two laser cavities can have a significant difference in losses that should be accounted for. Preliminary data that corrected for this, used the new drive laser round trip time, and $\kappa_{MC} = 0.01$ did not show a change from the results already presented.

In summary, the cross correlations show some matching to the drive laser, but very little between the response lasers. For uncoupled response lasers the correlation to the drive laser grows slowly and saturates at about 0.3. When the response lasers are mutually coupled the response lasers synchronize to the drive, but the levels are below 0.4. The drive removes the lag-synchrony and the isochronal cross correlation gets larger than the lag cross correlation for large values of drive coupling. The level of isochronal synchronization between the response lasers is less than 0.25. The levels of isochronal synchrony might be improved by matching the lasers' parameters more closely. Losses in response lasers could be better matched. Power levels in

the response lasers and the transmission lines may need to be determined more accurately to match coupling strengths better.

Chapter 6

Conclusions and future work

6.1 Conclusions

The addition of extra time-delayed feedback or coupling to EDFRLs has an impact on the dynamics that depends on the additional time delay. We observe an increase in the size of the intensity fluctuations for longer delays. Additionally, we see large fluctuations when the mutual coupling delay between two mutually coupled lasers matches the round trip time. We also observe different dynamical behavior depending on the delays. A challenge with our data is to represent it in a way that will show us the behavior at different time scales. The spatiotemporal representations provide a way to view dynamical features with vastly different time scales very efficiently.

We can analyze the spatiotemporal representations with KL decomposition. This is an efficient way to calculate some measures of complexity for our data. We considered the KL dimension and the Shannon entropy of the KL modes. The KL dimension was sensitive to the relative positions of the knee in the eigenvalue spectrum and the cut-off used to truncate the KL expansion. In this sense the Shannon entropy was more robust than the KL dimension and provided more consistent results. We found that the dynamics increase in complexity for long delays. We also found the surprising result that the dynamics simplify for short delays for the mu-

tually coupled lasers. The complexity measures presented can be used to evaluate waveforms for time-delayed systems for chaotic communications.

We observed a narrowing of the optical spectrum for two mutually coupled lasers as compared to their uncoupled spectra. This motivates a physical reason for the simplification of the dynamics we observe. An electromagnetic mode in a laser cavity will experience gain if it meets certain constraints defined by the cavity and the gain medium. Adding another laser adds more constraints. If the light will experience gain in both cavities then it must meet the constraints of both cavities. This reduces the number of electromagnetic modes for the coupled systems and reduces the complexity of the dynamics. It would be very interesting to understand what happens with multiple lasers.

We also observe lag-synchrony for all delays when we mutually couple two lasers together with sufficient coupling strength. There is an ambiguity about which laser is leading and which laser is following. Attempts to create isochronal synchrony between two response lasers by driving them with a third laser produced an increase in the isochronal response as measured by cross correlations. The levels of isochronal synchrony were low and need to be improved before. If the response lasers were mutually coupled then the lag synchrony was quenched as the drive coupling strength increased. The isochronal cross correlation became larger than the lag cross correlation, but the level of isochronal synchrony was still low. We think the isochronal level in both cases could be improved by a better match of the lasers' parameters and more care matching coupling and transmission line parameters.

6.2 Future work

There is more work related to these experiments that would be interesting to perform. In our some of our spatiotemporal representations we see structures traveling around the ring. Techniques have been proposed that shift the data to remove the traveling component [81]. It would be interesting to analyze our data with this technique and compare results with those presented here.

Another important factor to consider is the interpolation we performed on the time series data to line up the round trips for the spatiotemporal representations. We assume that adding data points this way does not affect the information content of the data and hence does not affect the complexity measures we calculated. An explicit validation of this assumption would be useful.

More work could also be performed to evaluate the spatial KL modes we calculated. Time delay embeddings of the modes could be done to examine the complexity of each KL mode. This would provide some insight into the issue discussed in Section 4.8 about mode complexity. Dot products between KL modes could be used to examine the projections of one mode onto another. Comparisons between data from different spatiotemporal representations could be compared this way. Comparison of modes for different data runs would show how consistent the KL modes are for the system. A comparison between data with different time delays could show the evolution of the dynamics. For example, Fig. 3.5(b), (c), and (d) show an evolution from high frequency oscillations to a mix of higher frequency oscillations and low frequency traveling waves to low frequency traveling waves with a small amplitude

high frequency component. Evaluating this evolution might provide some insight into the way the dynamics change with different delays. Finally, comparisons between the single laser with feedback and the mutually coupled lasers could also be done this way.

Some spatiotemporal data sets, such as in Fig. 4.6(b), show distinct changes in the dynamics within a single run of data. Performing KL decomposition for each temporal region of the dynamics would let us see if there are any KL modes that are consistent across regions. This would identify which dynamical features, if any, are stable across these changes in dynamical character.

The optical spectra of the lasers shows interesting behavior. Better measurements of the temporal behavior of the spectra would greatly enhance our understanding of the dynamics of the optical mode structure the lasers use. This in turn should provide insight into how the lasers respond to the delayed signals and generate the variety of dynamics seen. Additionally, there is great interest in coherently adding laser light together to make high power beams and also in the scalability of any systems developed. A better understanding of the spectral dynamics could help us design arrays of lasers where the lasers all emit light coherently with respect to each other, producing power levels that increase as the square of the number of lasers used.

Our attempts create isochronal synchrony by driving two mutually coupled lasers showed that the response lasers were reacting to the drive laser, but we did not see high quality synchrony. Better synchrony might be achieved by matching the lasers' parameters with more accuracy.

These are just some of the many directions that could be investigated. The fiber lasers studied in this work are fascinating, high-dimensional systems. They will present many puzzles and insights for future researchers to explore.

Bibliography

[1] Michael C. Mackey and Leon Glass. Oscillation and chaos in physiological control systems. *Science*, 197(4300):287–289, July 15th 1977.

[2] R. Holz and F. W. Schneider. Control of dynamic states with time delay between two mutually flow rate coupled reactors. *J. Phys. Chem.*, 97(47):12239–12243, 1993.

[3] Sungchul Kim, Byoungho Lee, and Dong Hwan Kim. Experiments on chaos synchronization in two separate erbium-doped fiber lasers. *IEEE Photon. Technol. Lett.*, 13(4):290–292, April 2001.

[4] Roy Lang and Kohroh Kobayashi. External optical feedback effects on semiconductor injection lasing properties. *IEEE J. Quantum Electron.*, QE-16(3):347–355, March 1980.

[5] Kensuke Ikeda. Multiple-valued stationary state and its instability of the transmitted light by a ring cavity system. *Opt. Commun.*, 30(2):257–261, August 1979.

[6] D. V. Ramana Reddy, A. Sen, and G. L. Johnston. Experimental evidence of time-delay-induced death in coupled limit-cycle oscillators. *Phys. Rev. Lett.*, 85(16):3381–3384, October 16th 2000.

[7] J. Doyne Farmer. Chaotic attractors of an infinite-dimensional dynamical system. *Physica*, 4D(3):366–393, 1982.

[8] Heinz Georg Schuster. *Complex Adaptive Systems*. Scator Verlag, Saarbrücken, Germany, 2001.

[9] E. Desurvire. *Rare-Earth-Doped Fiber Lasers and Amplifiers*, chapter 10. Erbium-Doped Fiber Amplifiers: Basic Physics and Characteristics, pages 531–582. Marcel Dekker, New York, 2nd revised and expanded edition, 2001.

[10] Q. L. Williams, J. García-Ojalvo, and R. Roy. Fast intracavity polarization dynamics of an erbium-doped fiber ring laser: Inclusion of stochastic effects. *Phys. Rev. A*, 55(3):2376–2386, March 1997.

[11] Govind P. Agrawal. *Nonlinear Fiber Optics*. Academic Press, San Diego, 3rd edition, 2001.

[12] Gregory D. VanWiggeren and Rajarshi Roy. Chaotic communication using time-delayed optical systems. *Int. J. Bifurcation Chaos*, 9(11):2129–2156, 1999.

[13] Apostolos Argyris, Dimitris Syvridis, Laurent Larger, Valerio Annovazzi-Lodi, Pere Colet, Ingo Fischer, Jordi García-Ojalvo, Claudio R. Mirasso, Luis Pesquera, and K. Alan Shore. Chaos-based communications at high bit rates using commercial fibre-optic links. *Nature*, 438(7066):343–346, November 17$^{\text{th}}$ 2005.

[14] Gregory D. VanWiggeren and Rajarshi Roy. Optical communication with chaotic waveforms. *Phys. Rev. Lett.*, 81(16):3547–3550, October 1998.

[15] Gregory D. VanWiggeren and Rajarshi Roy. Communication with chaotic lasers. *Science*, 279(5354):1198–1200, February 20$^{\text{th}}$ 1998.

[16] J. García-Ojalvo and Rajarshi Roy. Spatiotemporal communication with synchronized optical chaos. *Phys. Rev. Lett.*, 86(22):5204–5207, May 2001.

[17] Anthony E. Siegman. *Lasers*, chapter 29. University Science Books, Sausalito, CA, 1986.

[18] C. O. Weiss and R. Vilaseca. *Dynamics of Lasers*, chapter 7.3. VCH, New York, 1991.

[19] J. García-Ojalvo and Rajarshi Roy. Intracavity chaotic dynamics in ring lasers with an injected signal. *Phys. Lett. A*, 229(22):362–366, June 2$^{\text{nd}}$ 1997.

[20] David J. DeShazer, J. García-Ojalvo, and Rajarshi Roy. Bursting dynamics of a fiber laser with an injected signal. *Phys. Rev. E*, 67(3):036602, March 2003.

[21] Liguo Luo, T. J. Lee, and P. L. Chu. Chaotic behavior in erbium-doped fiber-ring lasers. *J. Opt. Soc. Am. B*, 15(3):972–978, March 1998.

[22] Liguo Luo, P. L. Chu, T. Whitbread, and R. F. Peng. Experimental observation of synchronization of chaos in erbium-doped fiber lasers. *Opt. Commun.*, 176(1–3):213–217, March 15$^{\text{th}}$ 2000.

[23] Arkady Pikovsky, Michael Rosenblum, and Jürgen Kurths. *Synchronization: A universal concept in nonlinear sciences*. Cambridge University Press, Cambridge, UK, 2001.

[24] Louis M. Pecora and Thomas L. Carroll. Synchronization in chaotic systems. *Phys. Rev. Lett.*, 64(8):821–824, February 1990.

[25] S. Boccaletti, J. Kurths, G. Osipov, D. L. Valladares, and C. S. Zhou. The synchronization of chaotic systems. *Phys. Rept.*, 366(1–2):1–101, 2002.

[26] Elizabeth A. Rogers-Dakin, Jordi García-Ojalvo, David J. DeShazer, and Rajarshi Roy. Synchronization and symmetry breaking in mutually coupled fiber lasers. *Phys. Rev. E*, 73(4):045201, 2006.

[27] Leah B. Shaw, Ira B. Schwartz, Elizabeth A. Rogers, and Rajarshi Roy. Synchronization and time shifts of dynamical patterns for mutually delay-coupled fiber ring lasers. *Chaos*, 16(1):015111, March 2006.

[28] Fan Zhang and Pak L. Chu. Effect of transmission fiber on chaos communication system based on erbium-doped fiber ring laser. *J. Lightwave Technol.*, 21(12):3334–3343, December 2003.

[29] Tilmann Heil, Ingo Fischer, Wolfgang Elsässer, Josep Mulet, and Claudio R. Mirasso. Chaos synchronization and spontaneous symmetry-breaking in symmetrically delay-coupled semiconductor lasers. *Phys. Rev. Lett.*, 86(5):795–798, January 2001.

[30] J. K. White, M. Matus, and J. V. Moloney. Achronal generalized synchronization in mutually coupled semiconductor lasers. *Phys. Rev. E*, 65(3):036229, March 2002.

[31] Liang Wu and Shiqun Zhu. Coexistence and switching of anticipating synchronization and lag synchronization in an optical system. *Phys. Lett. A*, 315(3):101–108, March 2003.

[32] C. Masoller. Anticipation in the synchronization of chaotic semiconductor lasers with optical feedback. *Phys. Rev. Lett.*, 86(13):2782–2785, March 2001.

[33] Josep Mulet, Claudio Mirasso, Tilmann Heil, and Ingo Fischer. Synchronization scenario of two distant mutually coupled semiconductor lasers. *J. Opt. B: Quantum Semiclassical Opt.*, 6(1):97–105, January 2004.

[34] Brian B. Zhou and Rajarshi Roy. Isochronal synchrony and bidirectional communication with delay-coupled nonlinear oscillators. *Phys. Rev. E*, 75(2):026205, 2007.

[35] Henry D. I. Abarbanel and Matthew B. Kennel. Synchronizing high-dimensional chaotic optical ring dynamics. *Phys. Rev. Lett.*, 80(14):3153–3156, April 1998.

[36] Edward Ott. *Chaos in Dynamical Systems*. Cambridge University Press, Cambridge, UK, 2nd edition, 2002.

[37] Holger Kantz and Thomas Schreiber. *Nonlinear Time Series Analysis*. Cambridge University Press, Cambridge, UK, 2nd edition, 2004.

[38] Henry D.I. Abarbanel. *Analysis of Observed Chaotic Data*. Springer, New York, 1996.

[39] F. T. Arecchi, G. Giacomelli, A. Lapucci, and R. Meucci. Two-dimensional representation of a delayed dynamical system. *Phys. Rev. A*, 45(7):R4225–R4228, April 1992.

[40] Giovanni Giacomelli and Antonio Politi. Relationship between delayed and spatially extended dynamical systems. *Phys. Rev. Lett.*, 76(15):2686–2689, April 1996.

[41] Uriel Frisch. *Turbulence: The legacy of A. N. Kolmogorov*. Cambridge University Press, Cambridge, UK, 1995.

[42] R. Badii and A. Politi. *Complexity: Hierarchical structures and scaling in physics*. Cambridge University Press, Cambridge, UK, 1997.

[43] Michael Kirby. *Geometric Data Analysis: An Empirical Approach to Dimensionality Reduction and the Study of Patterns*. John Wiley and Sons, New York, 2001.

[44] J. L. Kaplan and J. A. Yorke. Chaotic behavior of multidimensional difference equations. In H. O. Peitgen and H. O. Walter, editors, *Functional Differential Equations and Approximations of Fixed Points*, pages 204–227. Springer, Berlin, 1979.

[45] Martin Casdagli, Stephen Eubank, J. Doyne Farmer, and John Gibson. State space reconstruction in the presence of noise. *Physica D*, 51(1–3):52–98, 1991.

[46] Thomas M. Cover and Joy A. Thomas. *Elements of Information Theory*. John Wiley and Sons, New York, 2nd edition, 2006.

[47] A. N. Kolmogorov. Three approaches to the quantitative definition of information. *Probl. of Inform. Transmission*, 1(1):1–7, 1965.

[48] G. J. Chaitin. *Algorithmic Information Theory*. Cambridge University Press, Cambridge, UK, 1987.

[49] G. J. Chaitin. On the length of programs for computing binary sequences. *J. Assoc. Comp. Machinery*, 13(4):547–569, October 1966.

[50] R. J. Solomonoff. A formal theory of inductive inference. *Inf. Control.*, 7(1):1–22 and 224–254, 1964.

[51] Abraham Lempel and Jacob Ziv. On the complexity of finite sequences. *IEEE Trans. Inf. Theory*, IT-22(1):75–81, January 1976.

[52] F. Kaspar and H. G. Schuster. Easily calculable measure for the complexity of spatiotemporal patterns. *Phys. Rev. A*, 36(2):842–848, July 1987.

[53] Peter Grassberger. Problems in quantifying self-generated complexity. *Helv. Phys. Acta*, 62(5):489–511, July 1989.

[54] F. T. Arecchi. Pattern formation and space-time organization. In R. G. Harrison and J. S. Uppal, editors, *Nonlinear Dynamics and Spatial Complexity in Optical Systems*, pages 65–113. Scottish Universities Summer School in Physics and Institute of Physics Publishing, Bristol and Philadelphia, 1993.

[55] Lawrence Sirovich. Turbulence and the dynamics of coherent structures, Part I: Coherent structures. *Quart. of Appl. Math.*, XLV(3):561–571, October 1987.

[56] Philip Holmes, John L. Lumley, and Gal Berkooz. *Turbulence, Coherent Structures, Dynamical Systems and Symmetry*. Cambridge University Press, Cambridge, UK, 1996.

[57] Phillip J. Holmes, John L. Lumley, Gal Berkooz, Jonathan C. Mattingly, and Ralf W. Wittenberg. Low-dimensional models of coherent structures in turbulence. *Phys. Rep.*, 287(4):337–384, August 1997.

[58] Lawrence Sirovich and Michael Kirby. Low-dimensional procedure for the characterization of human faces. *J. Opt. Soc. Am. A*, 4(3):519–524, March 1987.

[59] T. Burkhard, M. O. Ziegler, I. Fischer, and W. Elsäßer. Spatio-temporal dynamics of broad area semiconductor lasers and its characterization. *Chaos, Solitons & Fractals*, 10(4-5):845–850, 1999.

[60] Ortwin Hess and Eckehard Schöll. Eigenmodes of the dynamically coupled twin-stripe semiconductor laser. *Phys. Rev. A*, 50(1):787–792, July 1994.

[61] Ortwin Hess. Spatio-temporal complexity in muilti-stripe and broad-area semiconductor lasers. *Chaos, Solitons & Fractals*, 4(8):1597–1618, 1994.

[62] Julien Clinton Sprott. *Chaos and Time Series Analysis*. Oxford University Press, Oxford, UK, 2003.

[63] Keinosuke Fukunaga and David R. Olsen. An algorithm for finding intrinsic dimensionality of data. *IEEE Trans. Computers*, C-20(2):176–183, February 1971.

[64] Scott M. Zoldi and Henry S. Greenside. Karhunen-Loève decomposition of extensive chaos. *Phys. Rev. Lett.*, 78(9):1687–1690, March 1997.

[65] Satosi Watanabe. Karhunen-Loève expansion and factor analysis theoretical remarks and applications. In *Transactions of the Fourth Prague Conference on Information Theory, Statistical Decision Functions, and Random Processes*, pages 635–660. Czechoslovak Academy of Sciences, Prague, 1965.

[66] Claude E. Shannon. A mathematical theory of comminucation. *Bell Syst. Tech. J.*, 27(3):379–423, and 27(4):623–656, 1948.

[67] Claude E. Shannon and Warren W. Weaver. *The Mathematical Theory of Communication*. University of Illinois Press, Urbana, IL, 1949.

[68] Fan Zhang, Pak L. Chu, R. Lai, and G. Ron Chen. Dual-wavelength chaos generation and synchronization in erbium-doped fiber lasers. *IEEE Photon. Technol. Lett.*, 17(3):549–551, March 2005.

[69] Emmanuel Desurvire. *Erbium-Doped Fiber Amplifiers: Principles and Applications*. John Wiley and Sons, New York, 1994.

[70] William J. Miniscalco. *Rare-Earth-Doped Fiber Lasers and Amplifiers*, chapter 2. Optical and Electronic Properties of Rare Earth Ions in Glasses, pages 17–112. Marcel Dekker, New York, 2nd revised and expanded edition, 2001.

[71] Oprel Technology Inc., Nepean, Ontario, Canada. *OFA-1203-17 Erbium-Doped Fiber Amplifier User's Manual*, 1997.

[72] Quinton L. Williams and Rajarshi Roy. Fast polarization dynamics of an erbium-doped fiber ring laser. *Opt. Lett.*, 21(18):1478–1480, September 15th 1996.

[73] Govind P. Agrawal and Niloy K. Dutta. *Semiconductor Lasers*. Van Nostrand Reinhold, New York, 2nd edition, 1993.

[74] Elizabeth A. Rogers. *Synchronization of High-Dimensional Dynamical Systems*. PhD thesis, University of Maryland-College Park, College Park, MD, 2005.

[75] Anthony E. Siegman. *Lasers*, chapter 11. University Science Books, Sausalito, CA, 1986.

[76] Andrew M. Fraser and Harry L. Swinney. Independent coordinates for strange attractors from mutual information. *Phys. Rev. A*, 33(2):1134–1140, February 1986.

[77] Peter Grassberger, Thomas Schreiber, and Carsten Schaffrath. Nonlinear time sequence analysis. *Int. J. Bifurcation and Chaos*, 1(3):521–547, 1991.

[78] Ioana Triandaf and Ira B. Schwartz. Karhunen-Loève mode control of chaos in a reaction-diffusion process. *Phys. Rev. E*, 56(1):204–212, July 1997.

[79] Gregory D. VanWiggeren and Rajarshi Roy. High-speed fiber-optic polarization analyzer: measurements of the polarization dynamnics of an erbium-doped fiber ring laser. *Opt. Commun.*, 164(1–3):107–120, June 1st 1999.

[80] Anthony L. Franz, Rajarshi Roy, Leah B. Shaw, and Ira B. Schwartz. Changing dynamical complexity with time-delay in coupled fiber laser oscillators. Submitted to *Phys. Rev. Lett.*

[81] Sonja Glavaški, Jerrold E. Marsden, and Richard M. Murray. Model reduction, centering, and the Karhunen-Loève expansion. In *Proc. 37th IEEE Conf. Decision and Control*, pages 2071–2076, Tampa, FL, December 1998.

[82] Ingo Fischer, Raul Vicente, Javier M. Buldu, Michael Peil, Claudio R. Mirasso, M. C. Torrent, and Jordi García-Ojalvo. Zero-lag long-range synchronization via dynamical relaying. *Phys. Rev. Lett.*, 97(12):123902, 2006.

[83] David J. DeShazer, Brian P. Tighe, Jürgen Kurths, and Rajarshi Roy. Experimental observation of noise-induced synchronization of bursting dynamical systems. *IEEE J. Selected Topics Quantum Electron.*, 10(5):906–910, September/October 2004.